Powerlaws, Bumps and Wiggles: Self-similar Models in the Era of Precision Cosmology

DISSERTATION

Presented in Partial Fulfillment of the Requirements for the Degree Doctor of Philosophy
in the Graduate School of The Ohio State University

By

Chris Orban, M.S.

Graduate Program in Physics

The Ohio State University

2011

Dissertation Committee:

Professor Terrence Walker, Advisor

Professor David Weinberg

Professor John Beacom

Professor Jim Beatty

Abstract

With the many questions raised by the discovery, about a decade ago, that the universe is in an accelerating phase of expansion, it is clear that cosmological N-body simulations will continue to play a key role in unravelling this mysterious phenomenon. Historically, the first generation of cosmological N-body codes were tested and verified using self-similar models for dark matter clustering that have special "scale-free" properties. These models, in addition to allowing novel tests of numerical accuracy, are also interesting as fundamental problems and have been insightful in illuminating the non-linear physics of cosmological structure formation. In this thesis I return to this theme, in the first part investigating in considerable detail a new class of self-similar dark matter clustering models with a large-scale clustering feature that closely resembles baryonic acoustic oscillations (BAO) – a key distance indicator for dark energy studies. The non-linear physics of this simplified model was investigated using cosmological N-body simulations and the results compared both to perturbation theory and a phenomenological model. In these comparisons the phenomenological model and one of the two perturbation theory models discussed generally matched the simulation data quite well – more specifically the "SimpleRG" perturbation theory scheme of McDonald (2007) was remarkably accurate. I also carried out (for the first time) a suite of numerical tests with this new self-similar model, concluding that with modest numerical requirements, current N-body simulations will accurately model the non-linear evolution of a BAO-like feature even for a wide range of broadband spectral power. Importantly, this statement is true of the shift of the BAO clustering feature – a crucial systematic for dark energy studies. In the second half of this thesis, again making use of self-similar numerical tests, I evaluate an alternative method for setting up and running ensembles of cosmological N-body simulations developed by Sirko (2005) based on the ideas of Pen (1997). This method maintains correspondence between the actual and simulated real-space (rather than fourier space) properties of the cosmological model and accordingly allows the average density in each box to vary slightly from one realization to another. Extensive tests show that this approach gives indistinguishable results, compared to the standard method, for the mean dark matter and halo clustering properties but that the box-to-box variance of these statistics in the new method is much higher than expected, making the scheme substantially sub-optimal for most uses. I discuss the assumptions in the method which cause this and comment on a regime where the Sirko (2005) approach may be very useful.

Dedicated to Scott Peck, Thomas Merton and Wendell Berry

ACKNOWLEDGMENTS

It is hard to put into words the feelings one gets, towards the end of a project, looking back on the life that was lived and the people who lived it with you during those months of hard work. I often say that science is a kind of promethean quest (in the most positive sense) which is like any other great journey – with joys, struggles, and a good amount of confusion. But it makes us what we are, and sharpens what is already there. I feel very priviliged that science has been my mountain to climb and that, institutionally, I have enjoyed the generous support of the Center for Cosmology and Astro-Particle Physics over the last few years. No less do I feel indebted to David Weinberg for taking me on as a student and for his guidance over the last three years. (I feel like I should write that sentence two more times for emphasis.) Much thanks also goes to my co-workers in CCAPP, especially to Michael Mortonson and Stelios Kazantzidis. I could not be more pleased to be graduating from such a widely-recognized group of folks and to have achieved something of the precedent that was set by the students who came before me.

As the saying goes, it takes a village... and, beyond academia, I carry as much appreciation for the amazing people I have befriended in Columbus and especially to my beautiful wife Julia who has seen me through good times and bad. Many thanks to our friends Robert and Michelle, Kristin and Andrew, Cathrine, Paul Rimmer, and their families; and also to 7th Avenue, and the Civic Association, to my neighbors and all my “hippie” friends. I have learned much from all of you.

Thanks goes also to my family (Sullivan’s included), for their support over the years. I couldn’t have done it without you all.

VITA

December 2004	B.S. Physics, University of Illinois at Urbana-Champaign
2006	University Fellow, The Ohio State University
2008	M.S. Physics, The Ohio State University
2007-2010	Graduate Teaching and Research Assistant

Publications

Orban, C., Weinberg, D.H., "Self-similar Bumps and Wiggles: Isolating the Evolution of the BAO peak with Power-Law Initial Conditions" (submitted)

Orban, C., Weinberg, D.H., "Revisiting a Novel Approach to Running Ensembles of Cosmological N-body Simulations" (in prep.)

Orban, C., Gnedin, O. Y., Weisz, D. R., Skillman, E. D., Dolphin, A. E., & Holtzman, J. A. "Delving Deeper into the Tumultuous Lives of Galactic Dwarfs" ApJ, 2008, 686, 1030

Li, H., Shengtai, L., Koller, J., Wendroff, B.B., Liska, R., **Orban, C.**, Liang, E.P.T., and Lin, D.N.C., "Potential Vorticity Evolution Produced by an Embedded Protoplanet," 2005, ApJ, 624, 1003.

Orban, C. and P.M. Ricker, "Modelling Protogalactic Collapse and Magnetic Field Evolution with FLASH." 2004, BAAS, 36, 1499.

Langston, G.I., **Orban, C.**, and T.S. Bastian, "A Search for Cyclotron Maser Emission from Extra-Solar Planets." 2002, BAAS, 34, 1176.

Fields of Study

Major Field: Physics

Table of Contents

Chapters

Appendices

List of Figures

Figure **Page**

List of Tables

Table **Page**

Chapter 1

INTRODUCTION

Self-similarity is symmetry across scale. It implies recursion, pattern inside of pattern.
– James Gleick

The work presented in this thesis springs ultimately from a very simple but powerful idea: physical systems that exhibit a great deal of symmetry will in certain cases evolve such that the dynamics at a given time is a scaled version of the state of the system at earlier (or later) times. This kind of behavior is referred to as "self-similar" evolution or self-similar scaling, and, famously, fractals are a well-known example of objects which have a self-similar appearance. In nature, there is no lack of systems that have this fractal-like property to some extent and as I write the tree in my front yard sheds its intricately-patterned leaves and we anxiously await the arrival of the first crystalline snowflakes of the season. The concept, in theoretical physics, is widely appreciated as the foundation of the theory of phase transitions and the renormalization group. But to a physicist the novelty of self-similarity lies in the property that the equations governing the system become fully independent of the physical size of the system. Often these equations are difficult to solve and this simplification can lead to penetrating insights into phenomena like phase transitions. In the case of cosmological structure formation, self-similar models are interesting both as fundamental challenges to theory and as powerful tests of the simulation methods designed to numerically treat this problem.

This is not the first study in cosmology to investigate self-similar models. A rich literature exists on the topic, and in arguably the most significant contribution to the field from these studies, the demonstration by Efstathiou et al. (1988) of self-similar evolution in the first generation of cosmological N-body simulations decisively confirmed the accuracy of those algorithms in certain regimes. This bolstered confidence in the simulation methods and enabled studies of more realistic cosmological models. (And eventually, by the 1990s, the predictions from cosmological N-body codes would become important pieces of evidence in the case for dark energy.)

In this work I show the results for self-similar tests – both from powerlaw cosmologies as in Efstathiou et al. (1988), as well as a new test to be discussed shortly – in order to likewise test the accuracy of the latest generation of codes at higher precision, and over a wider range of scales.

I also use self-similarity to test a novel method developed by Sirko (2005) for generating initial conditions and running ensembles of simulations. But I also take interest in these models as a fundamental challenge to theory and I make detailed comparisons between the simulation results and the *ab initio* predictions from perturbation theory (PT).

It is often said, in commenting on the advances in theory and observation in the last decade, that the field has entered the "era of precision cosmology," and, overarchingly, this investigation is motivated by the need to produce high-precision predictions for the growth of structure as observations, at a variety of wavelengths, become increasingly sensitive. As emphasized by Annis et al. (2005) and Wu et al. (2010), to fully realize the potential of the coming generation of astronomical surveys to constrain dark energy and other parameters of interest, an order of magnitude improvement in precision from theory is required. Although self-similar models bear only a qualitative resemblance, as discussed in the next section, to the to the currently-favored ΛCDM model of cold dark matter and a cosmological constant, the non-linear dynamics of these models are important as tests of perturbation theory and as fundamental problems. To use an analogy from quantum mechanics, self-similar models are, in a certain sense, the hydrogen atom of structure formation and should be understood before moving on to more complex problems. Additionally, numerical tests with self-similar models contribute to the larger effort by corroborating the accuracy of cosmological N-body codes for a wide variety of dark matter clustering models.

1.1 Powerlaw Cosmologies

Whereas fractals are exact copies of themselves, the cosmological models investigated here are only statistically self-similar. I illustrate this in Fig. 1.1 by showing snapshots from an N-body simulation in the three left-hand panels and comparing a zoomed-in view of the previous output alongside and to the right of those results. In each plot the particles come from a slice of the lower 1/8th of the simulation volume and, for visual comparison, the simulations are downsampled in the left hand panels so that each plot shows the same total number of particles. In each plot the non-linear scale, $R_{\rm nl}$, is shown, here defined as the scale where the rms overdensity in randomly placed spheres reaches the value of one. Importantly the zoomed-in plots on the right have the same value of $R_{\rm nl}$, relative to the axes shown, as the simulation outputs immediately to the left. Qualitatively, in terms of the distribution of voids and overdense regions, the zoomed-in slices bear a remarkable resemblance to the simulation outputs shown adjacent to it. If unconvinced of this, look at the zoomed-in density fields on the right and try to tell if this density distribution is a flipped or mirrored version of the plot immediately to the left. If it is hard to tell on first glance this is evidence that the two images are statistically similar. More rigorously, one can quantify the differences between the two images in a statistical way and in the limit of many realizations of this cosmological model the scaled-forward density field should be statistically equivalent to the density field at the later output. To the extent that these results do not match this is a sign of unwanted

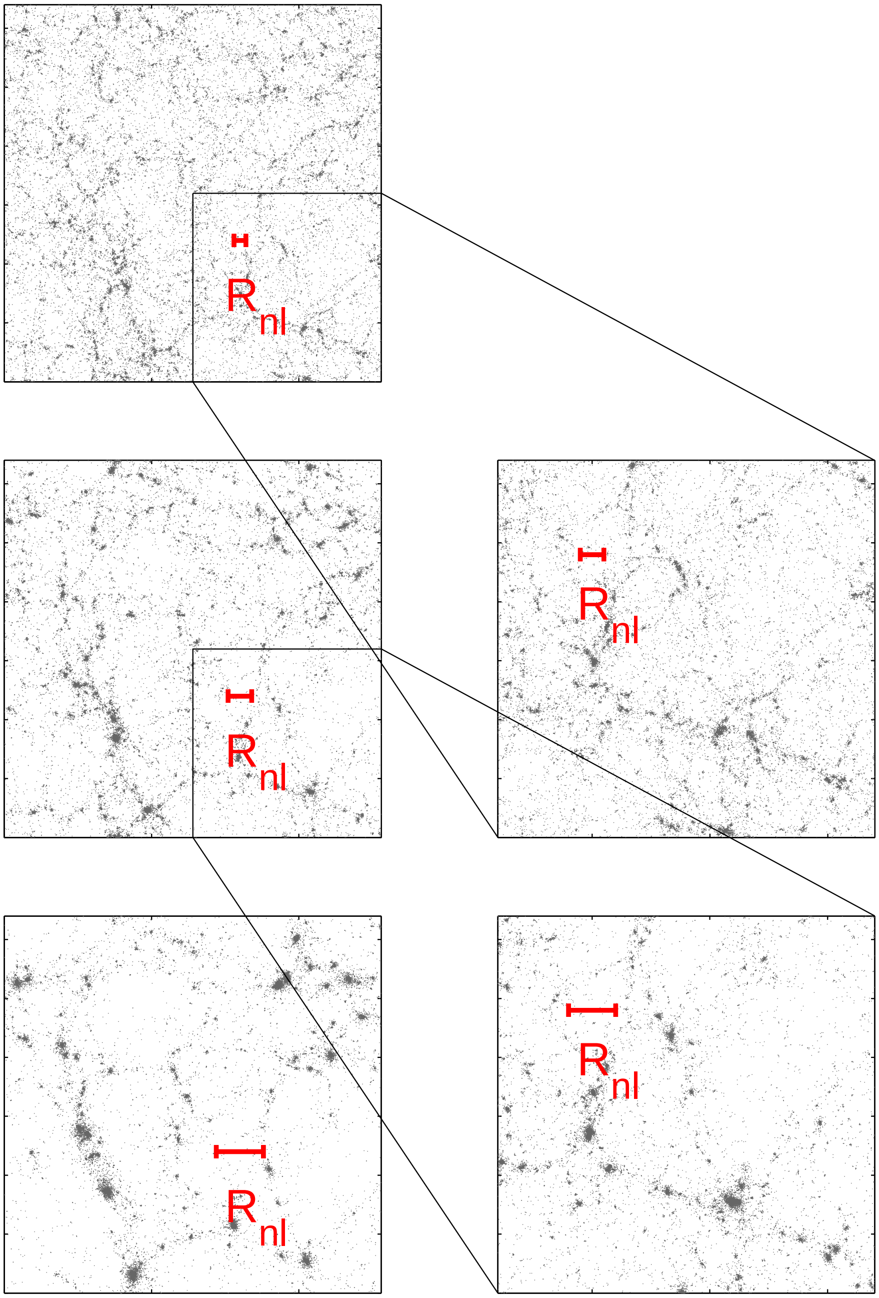

Figure 1.1: *Left panels* Slices from an N-body simulation showing particles in the lower 1/8th of the simulation volume. The axes extend out to the box scale and the plots appear in chronological order – the earliest output at the top and the last output at the bottom. The nonlinear scale, $R_{\rm nl}$, is shown in each plot. *Right panels* Slices from the lower-right quadrant of the preceding output. The non-linear scale is shown on each plot, indicating that the slices have the same level of clustering as the outputs shown to the left.

numerical effects.[1]

In Fourier space, Fig. 1.1 shows the evolution of the density field of an initially $P(k) = A\,k^{-1}$ spectrum where $\delta^3(\vec{k}-\vec{k'})P(k) = \langle \delta(\vec{k})\delta^*(\vec{k'})\rangle$ and $\delta(\vec{x}) = (\rho(\vec{x}) - \bar{\rho})/\bar{\rho}$, using $\rho(\vec{x})$ to represent the real-space density field and $\bar{\rho}$ is the average density in the box. In this study I will frequently show dark matter clustering results in terms of $\xi(r)$, which is the Fourier transform pair of $P(k)$. In general, since powerlaw power spectra have no special scales or features and since gravity, if we simulate without dark energy (i.e. $\Omega_m = 1$), has no preferred lengths the evolution of structure should be self-similar.[2] In this thesis I focus on $P(k) = Ak^n$ where $n = -0.5, -1, -1.5, \& -2$. This range of slopes roughly brackets the effective slopes of the ΛCDM power spectrum on scales accessible to current galaxy-redshift surveys.

1.2 Self-similar Bumps and Wiggles

This study introduces a new class of self-similar cosmological models. These models are close relatives of the "pure" powerlaw models discussed in the previous section. In real space, these pure powerlaw models are also powerlaws in real space and the Fourier transform of a $P(k) = Ak^n$ spectrum works out to be $\xi(r) = (r_0/r)^{n+3}$, as long as $-3 < n < 0$ (Peebles 1980). In the new class of models this real-space powerlaw is multiplied by a gaussian with a width and height inspired by the baryon acoustic oscillations (BAO) feature in ΛCDM. More explicitly, the linear theory correlation function is

$$\xi_{\rm IC}(r) = \left(\frac{r_0}{r}\right)^{n+3} (1 + A_{\rm bump}\, e^{-(r-r_{\rm bao})^2/2\sigma^2_{\rm bao}}). \tag{1.1}$$

Fig. 1.2 shows a comparison of the ΛCDM model and three different "powerlaw times a bump" models (corresponding to $n = -0.5, -1,$ and-1.5 slopes in Fourier space). All of the models are normalized such that $\xi(r) = 1$ at the same scale, $r = r_0$.

Since Eq. 3.22 contains another scale besides r_0, which fixes the amplitude of the powerlaw, this implies that the self-similar test illustrated in Fig. 1.1 does not apply to this new class of models. (For example "zooming-in" on one of the snapshots would enlarge both the BAO scale as well as the non-linear scale so that the two density fields would not be statistical copies of each other.) Instead, the evolution should be self-similar when two *different* sets of simulations, each with different values for $r_{\rm bao}$ and r_0, are compared at the same $r_0/r_{\rm bao}$. This ratio becomes the time variable for this class of models and any significant discrepancies in the statistics of the density field, at fixed $r_0/r_{\rm bao}$, can be interpreted as evidence of numerical inaccuracies (e.g., from interference from the artificially-introduced scale of the box or the scale of the initial mean inter-particle spacing). I show results from running a suite of these tests in the next chapter.

---

[1] These statements also apply to scaling outputs from later to earlier times and in practice statistics from all the outputs are compared together.

[2] Atomic physics does introduce new scales into the problem, however, we neglect this and run dark-matter-only simulations with large box sizes where these effects are small.

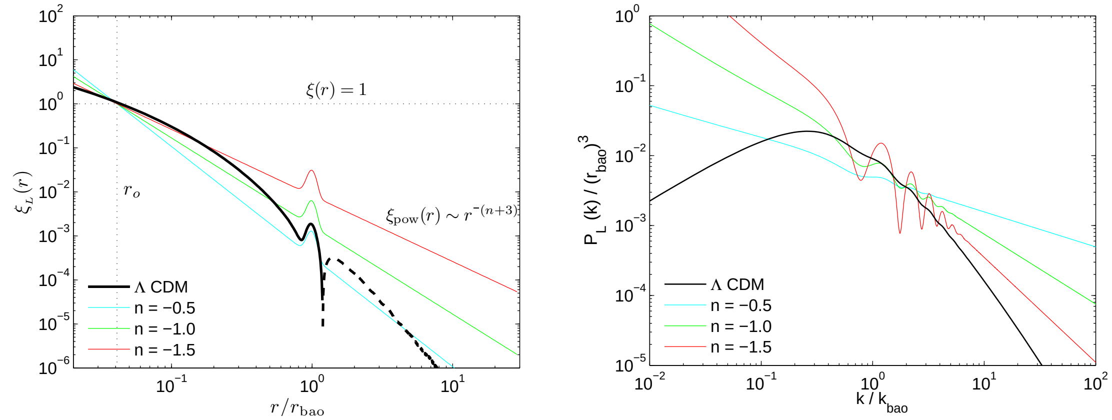

Figure 1.2: *Left panel* A comparison of the linear theory matter auto correlation function for ΛCDM (black and when $\xi_L < 0$ black-dashed) and the linear theory matter auto correlation functions for three examples from a new class of self-similar cosmological models (red, green, blue). *Right panel* The linear theory power spectra of the models shown in the left panel with the same normalization.

These simulations are also quite interesting as insightful probes of the non-linear physics at work on the large scales where the BAO feature appears. Measuring the BAO clustering feature in future surveys will be extremely valuable for constraining dark energy, as discussed in the next section, however this regime is difficult to model at high precision and ambitious surveys like BigBoss (Schlegel et al. 2009b), WFIRST (Blanford et al. 2010), and Euclid (Laureijs et al. 2009) will eventually reach the level where these inaccuracies would be an important source of systematic error. With this in mind, in Chapter 2, I model the non-linear dynamics phenomenologically, and, in Chapter 3, I show and discuss the predictions of two different *ab initio* PT models and compare those results to measurements from N-body simulations. Previously, PT schemes have only been rigorously tested with the ΛCDM and the "extreme" cCDM ($\sigma_8 = 1, \Omega_m = 1, \Omega_b = 0.4$) cosmological models (Carlson et al. 2009).

1.3 The Importance of BAO as a Cosmological Probe

From the beginning, the primary science driver for this thesis has been to sharpen (or at least test) the theoretical tools involved in predicting the evolution of the Baryon Acoustic Oscillations (BAO) clustering feature. Future measurements of this feature in astronomical surveys are anticipated to place strong constraints on the dark energy equation of state and in this section I sketch out a brief argument for why such optimism is well-founded. In this discussion, I consider only the BAO feature in the galaxy distribution – a slight preference for galaxies to be located at a fixed comoving scale (∼ 150 Mpc) away from each other – and in particular I only examine this feature in the angular clustering of galaxies where it has already been detected (Eisenstein et al. 2005;

Percival et al. 2010). Since, fundamentally, the clustering feature comes from a feature in the dark matter distribution which is imprinted on the things we observe, there are a variety of other ways in which future surveys may detect BAO (e.g. the Lyα forest, line of sight clustering of galaxies, 21cm emission). These observations hold great promise as well and I focus on the angular clustering of galaxies simply for brevity and to keep the discussion close to current observations.

BAO measurements are "geometrical" probes of dark energy, constraining, in some way, the relationship between cosmic distance and redshift. This places it in the same category as Type Ia supernovae but with the important difference that supernovae constrain distances as standard candles whereas the BAO feature is a "standard ruler". As a feature at fixed comoving distance, detecting the angular scale of the BAO at a given redshift is, conceptually, like knowing the length and angle subtended by one side of a triangle. In Euclidean, non-expanding, geometry the inference of the distance to this "ruler" is a trivial application of trigonometry. In an expanding universe, however, light rays are bent slightly en route, which changes the apparent angular size of the object at the observer. This effect can be parameterized in such a way as to retain much of our euclidean intuition. Defining an "angular diameter" distance, d_A, the observed angular size, $\Delta\theta$, of an object at fixed length Δr at redshift z is simply,

$$\Delta\theta = \frac{\Delta r}{d_A(z)} \tag{1.2}$$

where d_A captures the effects of the expansion (here assuming flatness),

$$d_A(z) = a(z) \int_{a(z)}^{1} \frac{c\, da}{a^2 H(a)} \tag{1.3}$$

and $H(a)$ is given by

$$H(a) = H_0 \sqrt{\Omega_{m,0} a^{-3} + \Omega_{de,0} a^{-3(1+w)}}. \tag{1.4}$$

As usual, $a = 1/(1+z)$, $\Omega_{m,0}$ and $\Omega_{de,0}$ are the current densities of matter and dark energy relative to the critical density and w is the equation of state of the dark energy. In practice, detecting the BAO peak at a certain angular separation, $\theta_{\rm bao}$, in galaxy clustering data yields a measurement of d_A since the comoving scale of the BAO (i.e. the sound horizon at decoupling) is well constrained by the cosmic microwave background,

$$s_{\rm bao} = \frac{1}{\sqrt{\Omega_{m,0} H_0^2}} \frac{2c}{\sqrt{3 z_{\rm eq} R_{\rm eq}}} \log \frac{\sqrt{1+R_{\rm rec}} + \sqrt{R_{\rm rec} + R_{\rm eq}}}{1+\sqrt{R_{\rm eq}}} \tag{1.5}$$

where $R = 3\rho_b/4\rho_\gamma$, ρ_b and ρ_γ being baryon and radiation densities respectively, and the "eq" subscripts refer to the epoch of matter-radiation equality while the "rec" subscripts refer to the epoch of recombination, $z_{\rm rec} \approx 1100$ (Eisenstein & White 2004). Measurements of the CMB place tight constraints on all of the parameters (or parameter combinations) in Eq. 1.5, and in the near future the Planck mission will be able to determine $s_{\rm bao}$ to an extremely high level of accuracy.

Therefore $d_A(z)$ is straightforwardly measured with

$$d_A(z) = \frac{s_{\text{bao}}}{\theta_{\text{bao}}(z)}. \tag{1.6}$$

Note that since the scale, s_{bao}, is set in the early universe when dark energy is subdominant, s_{bao} will be independent of all but the most extreme dark energy models. This attractive feature implies that this distance indicator is "anchored" to the CMB, regardless of the dark energy model, whereas other distance measures are anchored to the distances to nearby galaxies and the inference of the *absolute* distance to a given bin in redshift is not nearly as model-independent.

We can assess the sensitivity of BAO measurements to the dark energy equation of state with a few well-motivated approximations. Let us assume throughout that w is a constant, independent of redshift, and that $w = -1 + \Delta w$, so that $\Delta w = 0$ corresponds to a cosmological constant. Placing this in Eq. 3.3 and taylor expanding yields

$$\Delta \log H(a) \approx -\Delta w \frac{3}{2} \log(a)(1 - \Omega_m(a)) \tag{1.7}$$

where

$$\Omega_m(a) = \frac{\Omega_{m,0} a^{-3}}{\Omega_{m,0} a^{-3} + \Omega_{de,0} a^{-3(1+w)}}. \tag{1.8}$$

We can use this expression with Eq. 1.3 to calculate the deviation of the angular diameter distance, Δd_A, from the $w = -1$ model as a function of Δw and z, assuming all parameters in $H(a)$ except w are perfectly known (after the Planck mission this will be a remarkably good approximation, especially at high redshift!). For ease in what follows I will integrate over da instead of dz,

$$\frac{d(d_A)}{dw} = a \int \frac{c\,da}{a^2} \frac{-1}{H^2(a)} \frac{dH(a)}{dw} = a \int \frac{c\,da}{a^2 H(a)} \frac{d \log H(a)}{dw} = -a \int \frac{c\,da}{a^2 H(a)} \frac{3}{2} \log(a)(1 - \Omega_m(a)). \tag{1.9}$$

For redshifts smaller than $z \sim 0.33$ (i.e. during the dark energy-dominated era) we can treat the integral analytically with the rough approximation that $H(a) = H_0$ and $1 - \Omega_m(a) \approx 1 - \Omega_{m,0}$. It is possible to show that in this redshift range

$$\Delta w \approx \frac{\Delta d_A}{d_A} \frac{2}{3} \left(\frac{1-a}{-\log(a) + a - 1} \right) \left[\frac{1}{1 - \Omega_{m,0}} \right]. \tag{1.10}$$

This expression implies that at a certain redshift if one can constrain the deviation of angular diameter distance, Δd_A from the $w = -1$ model to a certain level then this can be used as an independent measurement of Δw. According to Eq. 1.6 $\Delta d_A/d_A$ is just $-\Delta\theta_{\text{bao}}/\theta_{bao}$ and the constraint on Δw is therefore straightforwardly related to the ability of a given survey to precisely identify the angular scale of the BAO. The most precise BAO measurement to date comes from Percival et al. (2010) who locate this angular scale to 2.7% from well over one hundred thousand galaxies with a mean redshift $z = 0.275$. They report that their best fit w is close to a cosmological constant with a 1σ (marginalized) error on w of 0.17. Using $\Delta d_A/d_A = 0.027$ with their best-fit values for $\Omega_{m,0}$

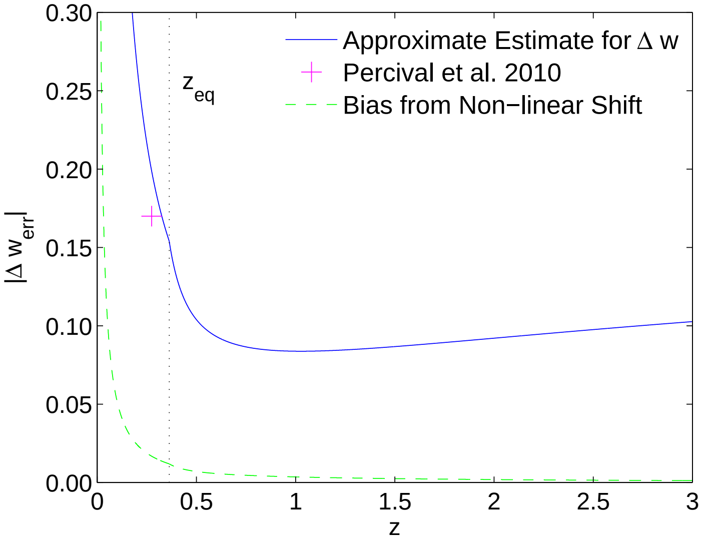

Figure 1.3: Measurement precision on Δw for constraining the angular scale of the BAO feature to $\Delta\theta_{\rm bao}(z)/\theta_{\rm bao}(z) = 0.027$ using Eqs. 1.10 & 1.11. For comparison the 1σ (marginalized) precision on w from Percival et al. (2010) is shown at $z = 0.275$, the mean redshift of the galaxy sample used to measure the BAO. An estimate of the bias on w from the neglecting the non-linear shift of the BAO peak, using expectations for the shift reported in Seo et al. (2010), is shown with a green-dashed line.

and $\Omega_{de,0}$ in Eq. 1.10 gives $\Delta w = 0.20$. Although some relatively daring approximations were made to obtain the expression in Eq. 1.10, and the comparison to rigorous multi-dimensional parameter constraints is admittedly crude, this result is quite reasonable.[3] Applying the same approach at higher redshift, during the epoch where the density is dark-matter dominated, we can approximate $H(a) \approx H_0\Omega_{m,0}^{1/2}a^{-3/2}$, and $\Omega_m(a) \approx \Omega_{m,0}a^{-3}/\Omega_{de,0}$ and again treat the integrals analytically. In this case,

$$\Delta w \approx \frac{\Delta d_A}{d_A}\frac{2}{3}\left(\frac{2}{\Omega_{m,0}}(\sqrt{a_{eq}} - \sqrt{a}) + a_{eq}^{-1} + 1\right) \Bigg/ \left(\tfrac{-\log(a_{eq})+a_{eq}-1}{a_{eq}}(1-\Omega_{m,0}) + \tfrac{2\,\Omega_{de,0}}{49\,\Omega_{m,0}^{3/2}}\left(2(a_{eq}^{7/2} - a^{7/2}) + 7(a^{7/2}\log a - a_{eq}^{7/2}\log a_{eq})\right)\right) \quad (1.11)$$

where $a_{eq} = (\Omega_{m,0}/\Omega_{de,0})^{1/3}$ is the scale factor at the transition from matter domination to dark energy dominated expansion. Eq. 1.11 should be a reasonable approximation for BAO measurements at redshifts beyond $z_{eq} \sim 0.33$. Fig. 1.3 shows the expected constraining power of BAO measurements for a wide range of redshifts using Eqs. 1.10 & 1.11 and assuming the same level of $\Delta d_A/d_A$ precision as Percival et al. (2010). For $z < z_{eq}$, Δw is poorly constrained merely because

---

[3] The Percival et al. (2010) result for Δw also includes weak constraints on dark energy from the CMB. This explains why their Δw is *smaller* than my estimate, which assumes that the only constraint on w comes from BAO.

the Hubble expansion rate is only weakly dependent on w in that range. At larger redshifts this is not the case and a measurement of the angular scale of the BAO always translates into interesting constraints on the dark energy equation of state. Note that Fig. 1.10 still assumes a constant w. Therefore in this picture the BAO measurement at each redshift provides an independent estimate of w, assuming no evolution in the equation of state over time.

The caveat to this approach, which motivates this work, is that although the CMB constrains $s_{\rm bao}$ to high accuracy at $z_{\rm rec} \approx 1100$, at lower redshift this scale can potentially shift due to the non-linear dynamics of structure formation. This effect has been characterized in N-body simulations, which predict a shrinking the BAO scale by $\sim 0.3\%$ by $z = 0$. In Fig. 1.3, using the Δw expressions in Eqs. 1.10 & 1.11 with the reported non-linear shift from ΛCDM simulations in Seo et al. (2010), I overplot an estimate of the bias on the inferred value of w from neglecting this effect. Since the shift grows steadily time this bias is most severe at low redshift, and, compared to the current state of the art (i.e. Percival et al. 2010) this is a relatively minor detail. However, as future surveys constrain the BAO feature more finely than the 2.7% assumed in the figure (which corresponds to lowering the vertical scale for the Δw estimate shown) the BAO shift will become an important systematic. This shift still needs to be characterized for a wide range of dark energy models and at higher precision likely using some combination of rigorously-tested perturbation theory models and fits to N-body results.

1.4 Revisiting a Novel Approach to Running Cosmological N-body Simulations

In the latter half of this work I revisit a very clever but seldom used method developed by Sirko (2005) for generating initial conditions and running ensembles of cosmological N-body simulations. This investigation is also motivated by the need for high precision predictions of the evolution of the BAO clustering feature. For this problem one typically runs ensembles of simulations (rather than simulating a single giant volume) in order to achieve the necessary precision by statistically combining the results for the large scale clustering while maintaining high spatial resolution. In the standard approach, each simulation box is given the same size and dark matter density – each realization varies only to the extent that it is a different sampling of the initial linear power spectrum. By contrast, in Sirko (2005), the assumptions of fixed box size and dark matter density are lifted[4],so that the cosmological parameters and box size are slightly different in each realization. The amplitude of these box-to-box fluctuations is related to the clustering power on the scale of the box, $P(k_{\rm box})$, where $k_{\rm box} = 2\pi/L_{\rm box}$.

In testing this method, Sirko (2005) compared results from ensembles of simulations performed

---

[4] To be more precise, the box size is fixed in Mpc units but the hubble parameter varies from box to box so that in h^{-1}Mpc units the box size does vary. Likewise the dark matter density is fixed in $M_\odot/{\rm Mpc}^3$ units whereas the critical density is defined in $h^2 M_\odot/{\rm Mpc}^3$ units, so that the ratio of the dark matter density to the critical density, Ω_m, also varies from box to box.

with the standard method to results from ensembles of simulations in the new framework. These comparisons were made exclusively using ΛCDM initial conditions, which do not allow any kind of self-similar cross-checks. In Chapter 3, I show self-similar test with this method both from pure powerlaw initial conditions as well as with the powerlaw times-a-bump models, comparing these results to ensembles of simulations performed in the standard way. Since the Sirko (2005) method was engineered to be a more faithful rendering of real space statistics, this chapter pays close attention to the results from the matter autocorrelation function, halo mass function and halo bias.

1.5 Conclusions and Appendices

Finally, in the concluding section of this work I summarize my results and sketch out a few possibilities for future work. This thesis also features two appendices, the first showing results for non-linear fitting functions for $n = -0.5, -1$ and -1.5 pure powerlaw initial conditions, which is useful for phenomenology and for tests of PT. Secondly, in Appendix B, I describe a remedy for the bias introduced by the integral constraint, that, if uncorrected, is artificially imposed in the *measurement* of $\xi(r)$. This issue becomes important for separations, r, approaching the scale of the box and in models with steeper power spectra. For $n = -0.5$ the correction is negligible, while for $n \lesssim -1.5$ this effect can be quite large. Appendix C discusses the ramifications of this correction for measuring the halo clustering bias.

Chapter 2

SELF-SIMILAR BUMPS AND WIGGLES

2.1 Introduction

The detection of the baryon acoustic oscillation (BAO) signature from observations of galaxy clustering (Eisenstein et al. 2005; Cole et al. 2005) represents a triumph of large-scale-structure theory and of state-of-the-art cosmological surveys. The BAO feature, imprinted by sound waves that propagate in the pre-recombination universe (Peebles & Yu 1970), provides a "standard ruler" that can be used to measure the distance-redshift relation and the evolution of the Hubble parameter $H(z)$ (Eisenstein et al. 1998; Blake & Glazebrook 2003; Seo & Eisenstein 2003). BAO measurements in the Sloan Digital Sky Survey (SDSS) yield a 2.7% measurement of the comoving distance to $z = 0.275$ (Percival et al. (2010); Kazin et al. (2010); improved from the 4% precision of Eisenstein et al. (2005)). Several ongoing experiments – WiggleZ (Drinkwater et al. 2010), HETDEX (Hill et al. 2008), and the BOSS survey of SDSS-III (Schlegel et al. 2009a) – seek to extend these measurements to higher redshift and improve their precision, using spectroscopic surveys of galaxies and (in the case of BOSS) the Lyα forest. Pan-STARRS (Kaiser et al. 2002) and the Dark Energy Survey (The Dark Energy Survey Collaboration 2005) seek to measure the distance-redshift relation using the BAO feature in angular galaxy clustering, and the Large Synoptic Survey Telescope (LSST Science Collaboration 2009) will eventually reach much higher precision measurements. Other ambitious experiments – the ground-based BigBOSS survey (Schlegel et al. 2009b) and the space-based WFIRST (Blanford et al. 2010) and Euclid (Laureijs et al. 2009) missions – plan spectroscopic surveys of $\gtrsim 10^8$ galaxies that in principle allow BAO measurements at the 0.1% level.

The high anticipated precision of these experiments places stringent demands on theory. To fully exploit these measurements as probes of cosmic acceleration, one must understand the effects of non-linear gravitational evolution and non-linear bias of mass tracers (e.g. galaxies or the Lyα forest) on the location of the BAO feature, calculating any shifts to an accuracy below the statistical measurement errors. This challenge has inspired many analytic and numerical investigations of BAO evolution (Carlson et al. 2009; Padmanabhan & White 2009; Eisenstein et al.

2007; Seo et al. 2008, 2010; Blake & Glazebrook 2003; Smith et al. 2008; Takahashi et al. 2009; Crocce & Scoccimarro 2008; Montesano et al. 2010; Sánchez et al. 2008), most of them focused on a ΛCDM cosmological model (inflation and cold dark matter with a cosmological constant) with parameters close to those favored by recent observations. In this paper, I pursue a complementary approach, inspired by N-body studies of self-similar cosmological models with a scale-free initial power spectrum $P(k) = Ak^n$ (e.g. Efstathiou et al. 1988; Bertschinger & Gelb 1991; Makino et al. 1992; Lacey & Cole 1994; Colombi et al. 1996; Jain et al. 1995; Smith et al. 2003; Widrow et al. 2009). Specifically, I investigate models in which the correlation function of the initial density field (the Fourier transform of its power spectrum) is

$$\xi_{\rm IC}(r) = \left(\frac{r_0}{r}\right)^{n+3} \left[1 + A_{\rm bump}\, e^{-(r-r_{\rm bao})^2/2\sigma_{\rm bao}^2}\right], \qquad (2.1)$$

a power-law modulated by a Gaussian bump centered at a "BAO" scale $r_{\rm bao}$.[5] For specified values of n and the bump height and width ($A_{\rm bao}$ and $\sigma_{\rm bao}$), the non-linear evolution of these initial conditions should depend only on the ratio $r_0/r_{\rm bao}$ of the correlation length to the BAO scale, and not (except for the overall change of scale) on the individual values of r_0 and $r_{\rm bao}$. Strictly speaking, this statement holds only for a particular cosmological model (e.g. $\Omega_m = 1$, $\Omega_\Lambda = 0$) in which the expansion factor $a(t)$ is a powerlaw of time, but I will show that the bump evolution is nearly identical for an $\Omega_m = 0.3, \Omega_\Lambda = 0.7$ cosmology when evaluated as a function of the linear growth factor.

There are several valuable aspects of this approach. First, by varying n, $\sigma_{\rm bao}$ and $r_0/r_{\rm bao}$, I can investigate the interplay among power spectrum slope, bump width and non-linearity in determining the shape and location of the BAO feature. Second, I can test analytic (e.g. perturbation theory) descriptions of BAO evolution over a much wider range of conditions than they have been tested to date, to see how well they capture the underlying physics of BAO evolution as opposed to working in a specific case. Among other things, I evolve simulations to values of $r_0/r_{\rm bao}$ much larger than those of conventional ΛCDM, so that I can clearly see where perturbative approaches break down and how far they can be pushed. In this regard, my approach is similar to that of Carlson et al. (2009) and Padmanabhan & White (2009) who use a "crazy" CDM (cCDM) model with parameters ($\Omega_m = 1, \Omega_b = 0.4, \sigma_8 = 1$) designed to produce larger BAO wiggles and stronger non-linear effects. Third, the self-similarity of these models allow for numerical tests where, as a consistency check, the evolution of the bump from simulations with the BAO bump with different numerical choices (e.g., box size relative to BAO scale, mean interparticle spacing, time steps) should all agree when compared at the same $r_0/r_{\rm bao}$.

Qualitatively, one expects the non-linear evolution of the BAO feature to involve a broadening and attenuation of the bump in configuration space, as discussed by Eisenstein et al. (2007), who describe matter scattering out of the BAO "shell". In Fourier space this phenomenon is seen as a

---

[5] Note that a pure power-law spectrum $P(k) = Ak^n$ corresponds to a correlation function $\xi(r) \propto r^{-(n+3)}$ Peebles (1980)

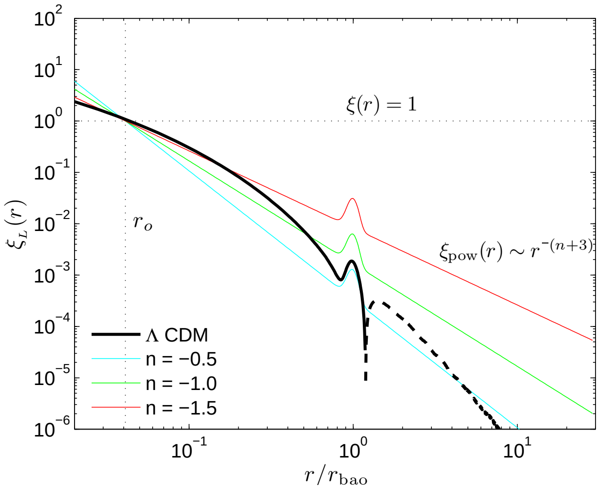

Figure 2.1: A comparison of the linear theory matter autocorrelation function for ΛCDM (black, becoming dashed when $\xi_L < 0$) and the linear theory matter autocorrelation functions investigated in this study. The ΛCDM correlation function shown was generated using the fiducial WMAP7 cosmology (assuming flatness), and the amplitude shown corresponds to $z = 0$. For comparison these different clustering distributions are normalized to have the same non-linear scale, r_0, as the ΛCDM case, where $\xi_L(r_0) \equiv 1$.

damping of oscillations at high-k. In many perturbative approaches, this damping is exponential and given by

$$\Sigma^2 = \frac{1}{3\pi^2} \int_0^\infty P_L(q)\ dq. \tag{2.2}$$

For pure powerlaw cosmologies one can easily see that this expression will be problematic. Physically, Eq. 2.2 is the rms displacement of particles – which includes the contribution from bulk motions that shift all particles in a large volume coherently – whereas the damping of the BAO feature is more fundamentally related to the rms relative displacement of pairs of particles. For the models investigated in this paper this subtlety becomes very important, and I argue that the broadening of the bump in these simulations scales according to the rms pairwise displacement equation (Eq. 2.11 below).

I describe the initial conditions and simulation setup in § 2.2, show and characterize the results for the bump evolution in § 2.3, and establish the numerical reliability of these results with self-similarity tests in § 2.4. In § 3.4 I show the power spectra in these simulations and compare both phenomenological and *ab initio* quasi-linear models to the simulation results. I compare my results with this setup to canonical ΛCDM in § 2.6 and comment on the broader relevance of these findings. Finally in § 2.7 I summarize the main conclusions and mention future directions for investigating this model.

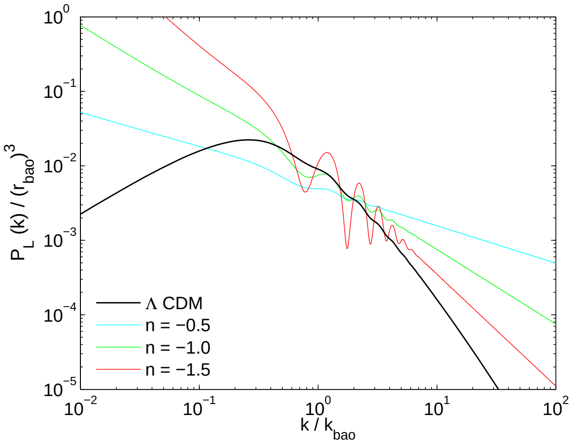

Figure 2.2: The linear theory power spectra of the models shown in Fig. 2.1 with the same normalization.

2.2 Simulations

2.2.1 Initial Conditions

I generate the initial conditions for the simulations by fourier transforming Eq. 3.22 to a power spectrum, $P_{\rm IC}(k)$, and using the publicly-available code 2LPT (Crocce et al. 2006), which computes particle displacements with second-order Lagrangian perturbation theory, to generate particle initial conditions files. 2LPT has been shown to minimize transients compared to the first order Zeldovich (1970) approximation.

In Fig. 2.1 I compare the three different $\xi_{\rm IC}(r)$ models explored in this paper (blue, green, and red) to a standard ΛCDM correlation function (black). I show the fourier transform of these correlation functions – the resultant $P_{\rm IC}(k)$ – in Fig. 2.2 compared to a flat ΛCDM power spectrum generated from CAMB (Lewis et al. 2000) assuming fiducial WMAP7 parameters (Komatsu et al. 2010). In keeping with convention, I refer to the powerlaw in fourier space ($n = -0.5, -1.0, -1.5$) rather than in configuration space. These choices for the powerlaw slope are inspired by the resemblance to the ΛCDM correlation function on different scales. Similarly, unless otherwise noted, I choose $\sigma_{\rm bao} = 0.075\, r_{\rm bao}$ as the ΛCDM-inspired gaussian width and $A_{\rm bump} = 2.75$ as the gaussian amplitude of the BAO feature.

In this study my time variable is $r_0/r_{\rm bao}$, where $\xi_L(r_0) \equiv 1$. This quantity grows as the amplitude of $\xi_L(r)$ becomes larger and the correlation length r_0 increases. For convenience I show conversions between this convention for the non-linear scale and other choices in Table 2.1. Other popular conventions define the non-linear scale as $\sigma(R_*) \equiv 1$ or $\sigma(R_*) \equiv \delta_c$, i.e. the scale where the rms density in spheres reaches one or reaches the threshold for spherical collapse, $\delta_c = 1.69$. I show $R_*/r_{\rm bao}$ for $\sigma(R_*) \equiv 1$ in the second column in Table 2.1; to convert from $\sigma(R_*) \equiv 1$

to $\sigma(R_*) \equiv \delta_c$, multiply this column by $\delta_c^{2/(n+3)}$. A fourier-space convention for the non-linear wavenumber, $\Delta^2(k_{\rm NL}) \equiv 1$ where $\Delta^2(k) = k^3 P(k)/(2\pi)^3$, is also shown in the third column. $k_{\rm NL}$ is shown divided by $k_{\rm bao} = 2\pi/r_{\rm bao}$ so as to be independent of a specific choice of $r_{\rm bao}$ and to reflect the self-similar nature of the setup. Finally, the fourth column shows the effective value of σ_8, computed assuming $r_{\rm bao} = 100\,h^{-1}$Mpc. More generally this column can be interpreted to be the rms density contrast in spheres of radius 8% of the BAO scale.

I begin the simulations at the earliest epoch listed for each of the three models shown in Table 2.1, and I obtain outputs at each of the epochs listed.

2.2.2 Approximate Solution for $P_{IC}(k)$

Starting from the fourier transform relation,

$$P_{\rm IC}(k) = 4\pi \int_0^\infty \xi_{\rm IC}(r)\, \frac{\sin(kr)}{kr}\, r^2\, dr, \tag{2.3}$$

and breaking up $\xi_{\rm IC}(r)$ in Eq. 3.22 into two terms, I expect

$$P_{\rm IC}(k) = P_{\rm pow}(k) + P_{\rm wig}(k). \tag{2.4}$$

An exact analytic solution exists for the powerlaw term (Peebles 1980): the fourier transform of $P_{\rm pow} = Aa^2k^n$ is $\xi(r) = (r_0/r)^{n+3}$ with amplitudes related by

$$A\,a^2 = \frac{2\pi^2\ \ (2+n)}{\Gamma(3+n)\sin((2+n)\pi/2)} r_0^{n+3} \equiv A_n r_0^{n+3}. \tag{2.5}$$

The remaining $P_{\rm wig}(k)$ term in Eq. 2.4 is given by

$$\begin{aligned} P_{\rm wig}(k) \ &= \frac{4\pi A_{\rm bump} r_0^\gamma}{k} \times \\ &\int_0^\infty r^{-(n+2)} e^{-(r-r_{\rm bao})^2/2\sigma_{\rm bao}^2} \sin(kr)\, dr\ . \end{aligned} \tag{2.6}$$

Up to a normalization, the integral is simply the expectation value of $r^{-(n+2)} \sin kr$ over a gaussian probability distribution $p(r)$ centered on $r_{\rm bao}$ with width $\sigma_{\rm bao}$ (but truncated at $r > 0$):

$$\int_0^\infty r^{-(n+2)} \sin(kr)\, p(r)\, dr \approx (2\pi\sigma_{\rm bao}^2)^{1/2} \langle\, r^{-(n+2)}\ \sin(kr)\, \rangle. \tag{2.7}$$

Table 2.1: Normalization/Conversion Table

	r_0/r_{bao}	R_*/r_{bao}	$k_{\mathrm{NL}}/k_{\mathrm{bao}}$	σ_8
n = -0.5	0.00039	0.0073	34.1	0.05
	0.024	0.046	5.40	0.5
	0.043	0.080	3.10	1.0
	0.059	0.111	2.24	1.5
	0.074	0.139	1.78	2.0
	0.102	0.193	1.02	3.0
	0.129	0.243	0.856	4.0
	0.178	0.335	0.740	6.0
	0.311	0.584	0.588	12.0
n = -1	0.0027	0.0040	41.2	0.05
	0.027	0.040	4.12	0.5
	0.043	0.064	2.58	0.8
	0.053	0.080	2.06	1.0
	0.073	0.110	1.51	1.37
	0.080	0.120	1.37	1.5
	0.107	0.160	1.03	2.0
	0.160	0.240	0.687	3.0
	0.213	0.320	0.515	4.0
	0.267	0.400	0.412	5.0
	0.320	0.480	0.258	6.0
n = -1.5	0.0011	0.0015	56.6	0.05
	0.024	0.032	2.63	0.5
	0.061	0.080	1.04	1.0
	0.104	0.137	0.608	1.5
	0.153	0.202	0.414	2.0
	0.263	0.346	0.241	3.0
	0.386	0.508	0.164	4.0

Since $p(r)$ is strongly peaked at $r = r_{\rm bao}$, and since $\sin(kr)$ is generally much more sensitive than $r^{-(n+2)}$ to the value of r,[6] I have, to good approximation,

$$\langle r^{-(n+2)} \sin(kr) \rangle \approx \langle r^{-(n+2)} \rangle \langle \sin(kr) \rangle \approx r_{\rm bao}^{-(n+2)} \langle \sin(kr) \rangle, \tag{2.8}$$

leaving only the expectation value of $\sin(kr)$ to be determined. This expression is given by

$$\begin{aligned} \langle \sin(kr) \rangle &= (2\pi\sigma_{\rm bao}^2)^{-1/2} \int_0^\infty e^{-(r-r_{\rm bao})^2/2\sigma_{\rm bao}^2} \sin(kr)\, dr \\ &\approx \sin(kr_{\rm bao}) \exp(-(k\,\sigma_{\rm bao})^2/2). \end{aligned} \tag{2.9}$$

This line of approximation ultimately leads to

$$\begin{aligned} P_{\rm IC}(k) \;\approx\; & A_n r_0^3 (kr_0)^n \;+ \\ & 2^{5/2}\pi^{3/2} A_{\rm bump} \sigma_{\rm bao} r_{\rm bao}^2 \left(\frac{r_0}{r_{\rm bao}}\right)^{n+3} \frac{\sin(kr_{\rm bao})}{kr_{\rm bao}} e^{-k^2\sigma_{\rm bao}^2/2}. \end{aligned} \tag{2.10}$$

With the ΛCDM-inspired choices for the constants in this expression (discussed in § 3.2), the approximation for $P_{\rm IC}(k)$ agrees with the numerical integration to better than a percent (relative to the underlying powerlaw) over the entire range of k-values.

2.2.3 Integration of Particle Trajectories

I used the publicly-available Gadget2 code (Springel 2005) to integrate particle trajectories from the initial conditions. Gadget2 is a hybrid, Tree-PM code in which the long-range gravitational forces are computed by solving the Poisson equation in fourier space while the short range forces are computed using a Tree algorithm (Barnes & Hut 1986). Gadget2 is parallelized using standard MPI and allocates processors/cores with the space-filling Peano-Hilbert curve. This allows the code to perform well on massively-parallel machines.

Throughout, unless otherwise noted, I simulate the powerlaw times a gaussian model using a flat $\Omega_m = 1.0$ cosmology with no dark energy, much like in self-similar pure powerlaw investigations (e.g. Efstathiou et al. 1988; Widrow et al. 2009) or in cCDM (Carlson et al. 2009; Padmanabhan & White 2009). This choice allows structure to grow indefinitely, avoiding the freeze-out limit when the dark energy component comes to dominate. However, in § 2.4.2, I present some simulations that include a cosmological constant and conclude that the evolution of the bump still only depends on the ratio of the non-linear scale to the BAO scale, even when dark energy is present.

Most of the simulations presented here, unless otherwise noted, were run with 512^3 particles

---

[6] $\sin(kr)$ goes as r^1 when k is small, and clearly varies rapidly with r when k is large. By contrast $r^{-(n+2)}$ varies as $r^{-0.5}$ for $n = -1.5$ and $r^{-1.5}$ for $n = -0.5$. Most of the inaccuracy in the final result for $P_{\rm IC}(k)$ comes from Eq. 2.8. The approximations in Eqs. 2.7 & 2.9 are more accurate because they only depend on the assumption that $\int_{r_{\rm bao}}^\infty \exp(-r^2/2\,\sigma_{\rm bao}^2)\, dr \approx 0$.

using a 768^3 PM grid for the large scale forces and a comoving force softening (relevant to the tree part of the code) of 1/4th the initial mean interparticle spacing. The box size was chosen to be $\sim 20\times$ larger than the BAO scale, making the force softening $\sim$1/2000th the scale of the box. I ran seven realizations of each model in order to obtain better statistics on large scales. I also performed pure powerlaw simulations (i.e. no wiggles) with the three cases ($n = -0.5$, $n = -1$, $n = -1.5$) to compare with the cases that include a BAO feature (Appendix A). Also note that I apply a correction to $\xi_{\rm meas}(r)$ to account for the artificial enforcement of the integral constraint on $\xi_{\rm meas}(r)$ (Appendix B). This correction is important on large scales for $n \leq -1$.

The simulations were evolved to the point where the non-linear scale reached approximately 30% of the initial BAO scale. As in pure powerlaw simulations, there is a concern that for steep power spectra the missing power on scales larger than the box will invalidate the results. However, even in the last output of the $n = -1.5$ case, which has the most large scale power, the simulations fall well within the guidelines recommended by Smith et al. (2003), and the self-similarity of the pure powerlaw results in Appendix A seem also to confirm the validity of the simulation results.

All of the simulations presented here were performed using the Glenn cluster at the Ohio Supercomputer Center[7]. In total, the results in this paper are based on 28 512^3-particle simulations of powerlaw+bump initial conditions, 21 256^3-particle simulations and 28 512^3-particle simulations used in the tests of 2.4, and 20 512^3-particle simulations of pure powerlaw models presented in Appendix A.

2.3 Evolution of the BAO Bump

2.3.1 $\xi(r)$ results for fiducial case

Fig. 2.3 presents the main results for the configuration-space evolution of the BAO feature. Remarkably, when divided by the pure powerlaw correlation function as in the plots on the right hand column, the BAO feature maintains a gaussian shape throughout the non-linear broadening and damping that occurs in structure formation.[8] In linear theory the bump would maintain the initial shape as indicated with the black dashed lines on the right hand column.

I overplot the best fit gaussians on the right hand column with dot-dashed lines of various colors corresponding to different epochs to emphasize and better illustrate this gaussian behavior. Quantitative measures of the evolution in bump amplitude and width are considereed in § 2.3.3.

When comparing the three models, one should bear in mind that at fixed $r_0/r_{\rm bao}$ the bump in the $n = -0.5$ case is at a much lower clustering amplitude than in the $n = -1.5$ case simply because an $n = -1.5$ powerlaw has much more large scale power, and I defined the initial bump feature to be a gaussian *times* (rather than added to) a powerlaw. The simulation data for the $n = -0.5$ case are noisier, especially at early epochs, because is a measurement of a weaker signal.

---

[7] `http://www.osc.edu/supercomputing/hardware/`

[8] The exception, discussed below, is at late times (high clustering amplitudes) in the $n = -1.5$ model.

Figure 2.3: Matter 2-point correlation function results for a powerlaw times a gaussian model for dark matter clustering. The upper two panels show results for the $n = -0.5$ background powerlaw, while the middle two panels show $n = -1$ and the lower two $n = -1.5$. The left panels show the measured matter autocorrelation function from the simulations at various epochs as colored points and, in dashed lines with the same color scheme, the corresponding linear theory correlation function at each epoch. The right panels show the matter autocorrelation function divided by the pure powerlaw correlation function, $\xi_{\rm pow}(r)$. Black dashed lines show the linear theory prediction, which is independent of epoch. Typical errors on the mean for $\xi_{\rm meas}(r)/\xi_{\rm pow}(r)$ are shown off to the right for various epochs, but note that errors are strongly correlated across the full range of the bump. On the right hand panels we also overplot with dot-dashed lines the best fit gaussians with the same color scheme as the measurements from simulations. $\xi(r)$ has been corrected for the integral constraint as described in Appendix B.

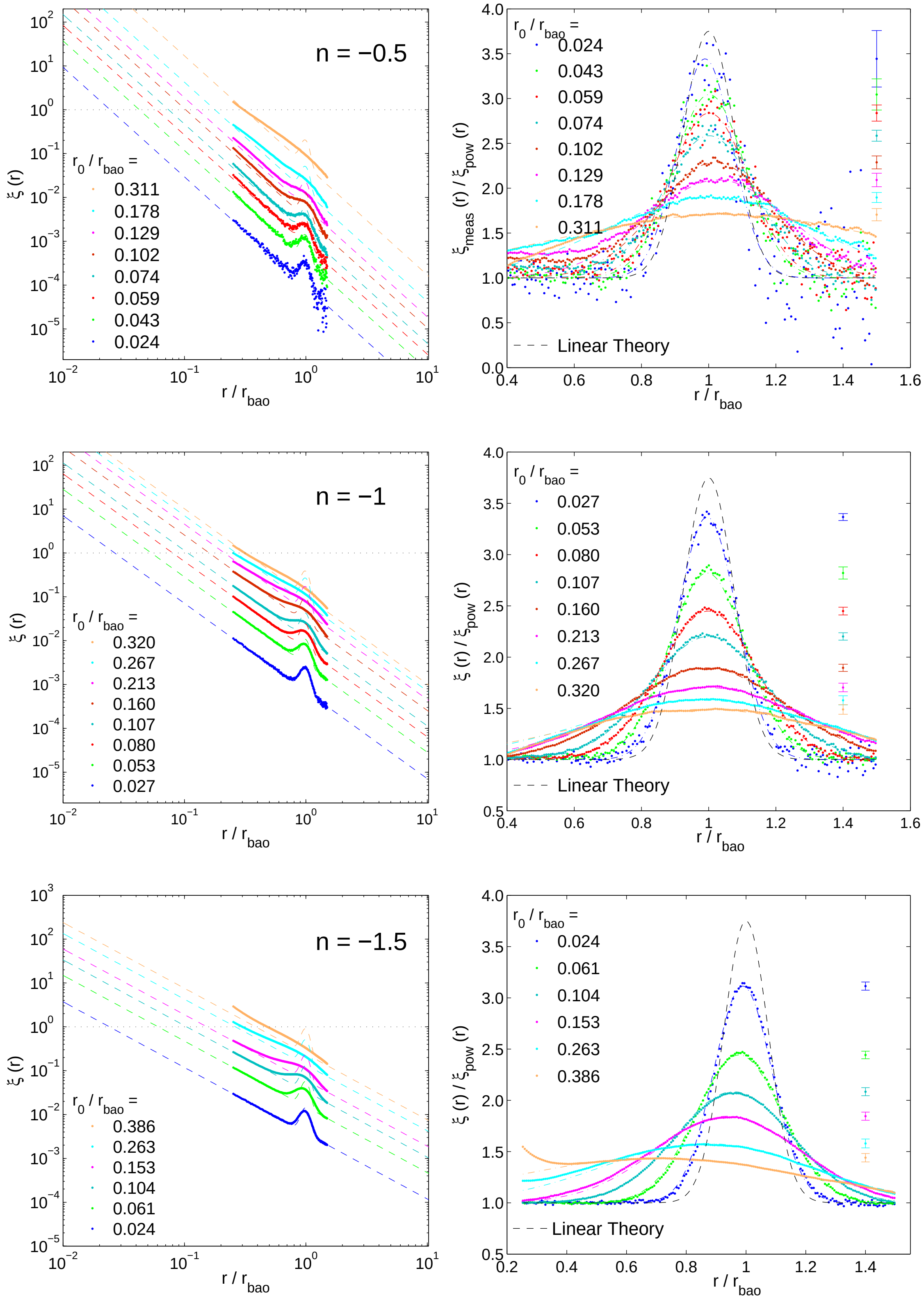
n = −0.5
n = −1
n = −1.5
ξ (r)
r / r$_{bao}$
r$_0$ / r$_{bao}$ =
0.311
0.178
0.129
0.102
0.074
0.059
0.043
0.024
ξ$_{meas}$ (r) / ξ$_{pow}$ (r)
Linear Theory
0.320
0.267
0.213
0.160
0.107
0.080
0.053
0.027
ξ (r) / ξ$_{pow}$ (r)
0.386
0.263
0.153
0.104
0.061
0.024

Figure 2.3:

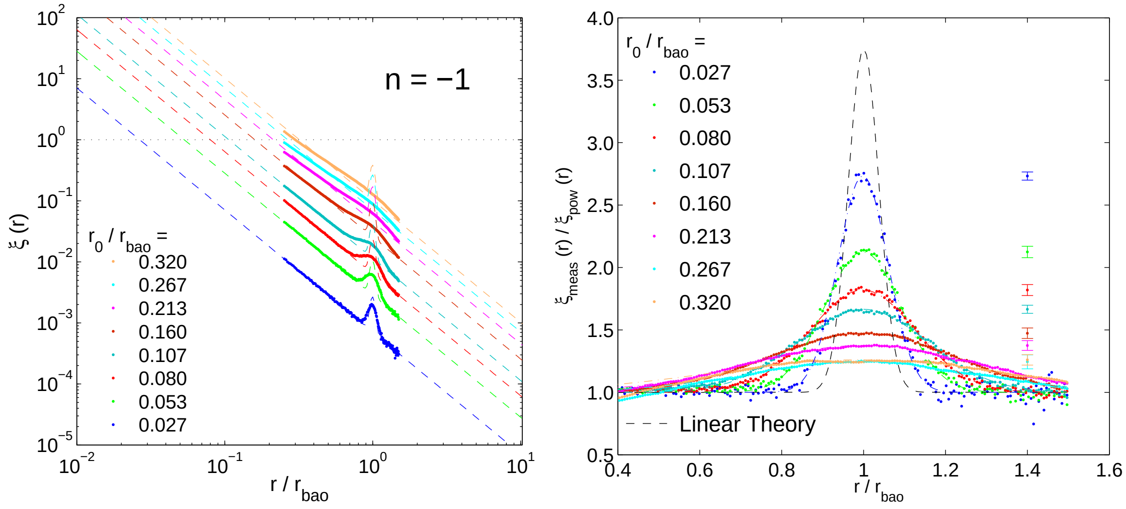

Figure 2.4: Results for a setup where the initial gaussian width of the bump is half of its fiducial value and the background powerlaw is set to $n = -1$. As in Fig. 2.3 different outputs are shown in different colors, with the typical errors on the mean offset to the right. $\xi(r)$ has been corrected for the integral constraint as described in Appendix B.

The other striking feature of Fig. 2.3 is that the location of the bump maximum stays nearly fixed in the $n = -0.5$ and $n = -1$ cases, even when they are evolved to high values of $r_0/r_{\rm bao}$ (corresponding to $\sigma_8 = 6 - 12$), while the location of the maximum for the $n = -1.5$ case shifts substantially at late times. The shifts for $n = -1.5$ are 6, 14, and 29 % at $r_0/r_{\rm bao} = 0.153$, 0.263, 0.386 (corresponding to $\sigma_8 = 2$, 3, 4). By contrast, in ΛCDM one typically sees shifts of $\sim 0.5\%$ by $z = 0$ ($\sigma_8 \approx 0.8$) and extrapolating the fitting formula of Seo et al. (2010) to an extreme value of $\sigma_8 = D(z)/D(0) \approx 4$ predicts a shift of only $\sim 5\%$. Qualitatively, I can understand the different behavior of $n = -1.5$ as a consequence of the much higher clustering amplitude at $r \approx r_{\rm bao}$ (see Fig. 2.1). I will discuss the non-linear shift of the BAO peak in further detail in following sections.

As one last qualitative note on the $n = -1.5$ results in Fig. 2.3, at the two latest epochs one can see that the correlation function at $r \sim 0.5 r_{\rm bao}$ is showing significant non-linear evolution away from the initial power-law, in contrast to the other two cases. I avoid this region in determining the best fit gaussians to the simulation data.

2.3.2 Evolution of a "Skinny" Bump

I also investigated a case where the initial gaussian width of the bump was half of the value in the fiducial case, i.e. $\sigma_{\rm bao} = 0.0375\, r_{\rm bao}$ instead of ΛCDM-inspired value of $\sigma_{\rm bao} = 0.075\, r_{\rm bao}$. Keeping $A_{\rm bump}$ fixed at 2.75, I performed simulations only for the $n = -1$ background powerlaw. These results are shown in Fig. 2.4. The bump clearly maintains a gaussian shape as it is damped out, and, as in the fiducial $n = -1$ case, there does not seem to be any shift in the BAO peak by the end of the simulation.

2.3.3 Quantitative Characterization of the Bump Evolution

In Figs. 2.5-2.6 I show plots comparing the amplitude, width, and measured shift from gaussian fits to the simulation results. These gaussian functions were determined by first making a rough determination of the BAO peak and bump amplitude from $\xi(r)/\xi_{\text{pow}}(r)$, then varying r_{bao}, A_{bump} and σ_{bao} in a 3-dimensional χ^2 to find the best fit. I avoided correlation function data more than $\Delta r \sim 0.3 r_{\text{bao}}$ below the peak in finding the best fit gaussian, to avoid effects of non-linear evolution of the underlying powerlaw correlation function. Error bars in Figs. 2.5 & 2.6 were determined via jackknife error estimation by sequentially omitting the correlation function results for one of the seven realizations and determining the best fit gaussians in each case. The errors on $A_{\text{bump}} \times \sigma_{\text{bao}}/r_{\text{bao}}$, a dimensionless proxy for the area of the bump, are from propagated errors in the values of A_{bump} and σ_{bao}. The $n = -1.5$ case suffers from a slight degeneracy between the amplitude of the bump and the magnitude of the non-linear shift, so the jackknife error bars are slightly larger in this case.

Fig. 2.5 shows the main results for the quantitative evolution of the dimensionless bump width, $\sigma_{\text{bao}}/r_{\text{bao}}$, bump amplitude, A_{bump}, and area $A_{\text{bump}} \times \sigma_{\text{bao}}/r_{\text{bao}}$. In the top panel, in all cases there is significant broadening of the bump, while in the middle panel, even apart from the dot-dashed models which will be discussed in a moment, the amplitude of the $n = -0.5$ case appears to decrease more slowly than that of the other setups.

The lower panel of Fig. 2.5 shows that the area under the bump stays remarkably constant, closely following the black horizontal dashed and dot-dashed lines as the bump broadens and attenuates. I speculate that the non-linear dynamics of the growth of structure is just diffusively moving apart the pairs at separation $r \sim r_{\text{bao}}$ so that $\sigma^2_{\text{bao}} \approx \sigma^2_{\text{IC}} + \sigma^2_{\text{diff}}$, while the area under the bump stays constant and the gaussian shape is maintained. These assumptions underlie the models plotted in the top two panels of Fig. 2.5. The broadening is modeled using the linear theory equation for the mean-squared relative displacement between pairs (Eq. 9 from Eisenstein et al. 2007),

$$\Sigma^2_{\text{pair}} = r^2_{12} \int_0^\infty \frac{k^2 dk}{2\pi^2} P(k) f_{||}(k r_{12}), \tag{2.11}$$

where r_{12} is the separation and

$$f_{||}(x) = \frac{2}{x^2}\left(\frac{1}{3} - \frac{\sin(x)}{x} - \frac{2\cos(x)}{x^2} + \frac{2\sin(x)}{x^3}\right). \tag{2.12}$$

In the limit $r_{12} \to \infty$, Eq. 2.11 reduces to Eq. 2.2, i.e., the rms pairwise displacement Σ_{pair} asymptotes to the Zel'dovich displacement. However, modes with $k r_{12} \ll 1$ move pairs of particles

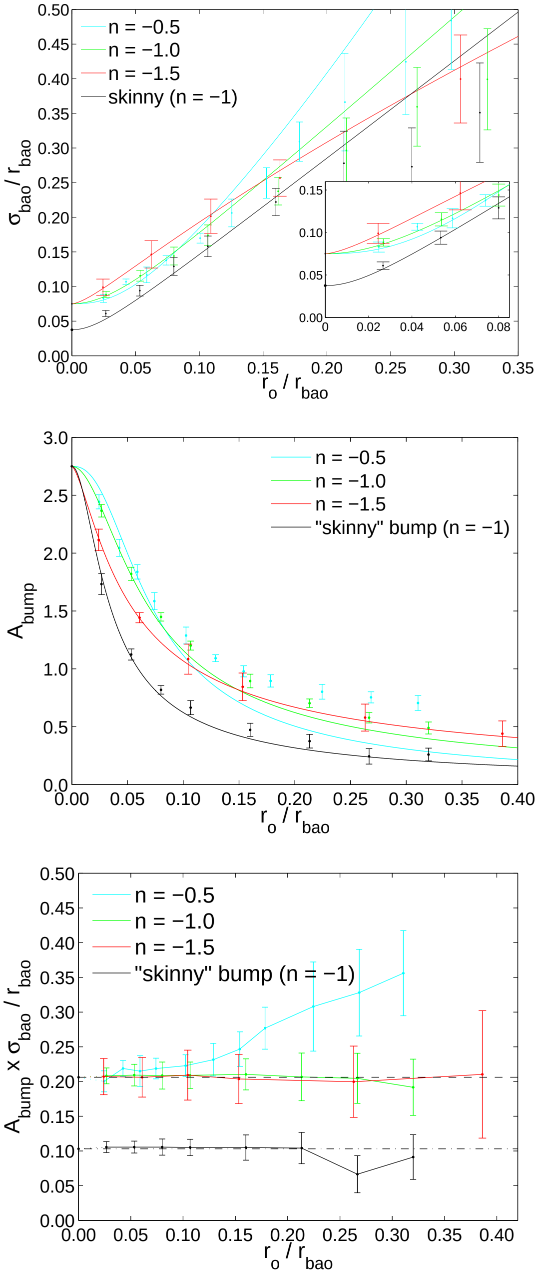

Figure 2.5: Results for the dimensionless width (top), amplitude (middle), and a proxy of the dimensionless area under the bump (lower panel). Overplotted in the top two panels is a diffusion model in which the broadening of the width scales as suggested by the rms pairwise displacement equation (Eq. 2.11) while the area of the gaussian bump is held constant. Error bars are from jackknife error estimation.

separated by r_{12} coherently, and while these modes may dominate the "bulk flow" they cannot affect clustering on scales $< r_{12}$. Notably, Eq. 2.2 is infrared divergent for $n \leq -1$, while Eq. 2.11 is convergent for $n > -3$, failing only when the *density contrast* (not peculiar velocity) has a divergent large scale contribution.

If, as an approximation, I consider a pure powerlaw power spectrum, $P(k) \approx Aa^2k^n$, Eq. 2.11 can be re-written as

$$\Sigma^2_{\rm pair} = \frac{A\,a^2}{r_{12}^{n+1}} \frac{1}{2\pi^2} \int_0^\infty x^{2+n} f_{||}(x) dx, \tag{2.13}$$

where $x = kr_{12}$. Selecting $r_{12} = r_{\rm bao}$, and since $Aa^2 \sim r_0^{n+3}$ (Eq. 3.14), this implies a scaling of the form

$$\Sigma^2_{\rm pair} \sim r^2_{\rm bao} \left(\frac{r_0}{r_{\rm bao}}\right)^{n+3}. \tag{2.14}$$

In Fig. 2.5 I therefore model the evolution of $\sigma_{\rm bao}$ by assuming this scaling and empirically fitting the constant of proportionality for each background powerlaw, i.e.,

$$\sigma^2_{\rm bao} = \sigma^2_{\rm IC} + 2\,\kappa_n\, r^2_{\rm bao} \left(\frac{r_0}{r_{\rm bao}}\right)^{n+3}. \tag{2.15}$$

I use the symbol κ_n and include a factor of 2 to emphasize the characterization of the bump evolution as a diffusion process.

The curves in the upper panel of Fig. 2.5 show predictions of Eq. 2.15 with values of $\kappa_n = \{4.5, 1.3, 0.5\}$ for $n = -0.5, -1$ and -1.5, respectively, chosen by visual fit to the simulation points. The model provides a good match to the data for $r_0/r_{\rm bao} < 0.1$. Most significantly, the same κ_n fits both the fiducial and skinny $n = -1$ cases, supporting the conjecture that the bump width is effectively set by a quadrature sum of the linear theory "intrinsic" width and the rms pairwise displacement. The scaling with rms displacement holds fairly accurately out to large $r_0/r_{\rm bao}$. The constant-area approximation holds well for $n = -1$ and $n = -1.5$, but it breaks down for $n = -0.5$ when $r_0/r_{\rm bao} \gtrsim 0.1$, explaining the divergence of points and model curve in the middle panel of Fig. 2.5.

2.3.4 Movement of the BAO peak

Fig. 2.6 shows the change in position of the bump maximum, determined as described in § 2.3.3 by fitting a gaussian to the ratio of the non-linear correlation function to the linear-theory powerlaw. As already noted in the discussion of Figs. 2.3 and 2.4, there is no significant shift of the peak location in simulations for either the $n = -0.5$ or $n = -1$ cases (fiducial or "skinny" bump). Error bars on the $n = -0.5$ peak location become large at late times because the bump itself flattens and the large scale correlation is weak. For $n = -1$, the skinny bump errors are initially lower than those of the fiducial model because the sharper peak can be centroided more precisely, but they are higher at late times because the skinny bump gets depressed to a lower amplitude. In contrast

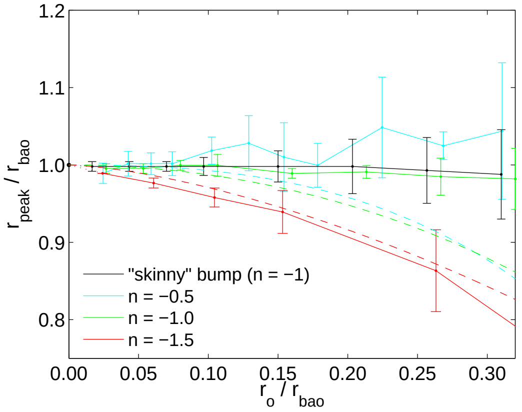

Figure 2.6: Results for the non-linear shift of the BAO peak measured from the right panels of either Fig. 2.3 or Fig. 2.4. The "skinny" bump results are offset to the left by $\Delta r_0/r_{\rm bao} = 0.01$ so as to avoid overlap with the fiducial $n = -1$ results. Dashed lines show a prediction for the shift of the peak based on Eq. 32 from Smith et al. (2008). Error bars are from jackknife error estimation.

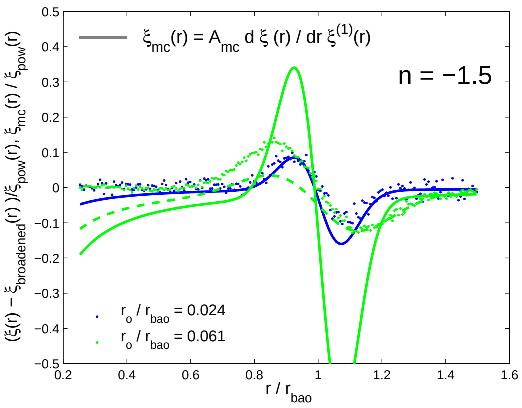

Figure 2.7: Residuals showing the non-linear shift from subtracting the gaussian fits centered on the un-shifted BAO scale from the matter correlation function results from the first two outputs in the $n = -1.5$ case (blue and green points). The dashed lines show the predictions of the Crocce & Scoccimarro (2008) ansatz in this case using $A_{\rm mc} = 34/21$ for both outputs. The thin green-dashed line assumes a broadened and attenuated bump in $\xi_{\rm mc}(r)$ as discussed in the text.

to the other cases, the $n = -1.5$ model shows significant and strong peak shifts, evident already for $r_0/r_{\rm bao} = 0.024$ ($\sigma_8 = 0.5$). Indeed, I have truncated the plot before the final $n = -1.5$ output, with $r_0/r_{\rm bao} = 0.386$ and $r_{\rm peak}/r_{\rm bao} = 0.71$.

I compare these results to an elegant model for the shift from Smith et al. (2008) that uses linear theory velocities and the pair-conservation constraint on $\xi(r)$ to track the average motion of pairs separated by $r_{\rm bao}$. Their equation (32) can be written

$$\frac{D^2(z)}{D^2_{\rm ic}} - 1 = \int_{r_{\rm peak}}^{r_{\rm bao}} \frac{3}{\bar{\xi}_{\rm ic}(r)} \frac{dr}{r} \ , \tag{2.16}$$

where $D(z)$ is the linear growth factor, the subscript ic refers to initial conditions when fluctuations are fully in the linear regime, $r_{\rm bao}$ is the linear theory BAO position, $r_{\rm peak}$ is the non-linear position of the peak, and $\bar{\xi}(r)$ is the volume-averaged correlation function interior to radius r. For $D(z)/D_{\rm ic} \gg 1$ and the initial conditions investigated here, this equation leads to the approximate result

$$\frac{r_{\rm peak}}{r_{\rm bao}} \approx \left[1 + \frac{n+3}{n} C_n \left(\frac{r_0}{r_{\rm bao}}\right)^{n+3}\right]^{1/(n+3)} \ , \tag{2.17}$$

where C_n would be 1.0 for a pure powerlaw spectrum and incorporating the bump gives $C_n \approx \{1.13, 1.26, 1.38\}$ for $n = \{-0.5, -1, -1.5\}$. For $n < 0$ this formula predicts that the peak shifts to smaller scales. In the limit of small $r_0/r_{\rm bao}$, a binomial expansion yields

$$\frac{r_{\rm peak}}{r_{\rm bao}} \approx 1 + \frac{C_n}{n} \left(\frac{r_0}{r_{\rm bao}}\right)^{n+3} \ . \tag{2.18}$$

Since $r_0^{n+3} \propto D^2(z)$, the non-linear shift grows as the square of the linear growth function as expected from PT (e.g. Padmanabhan & White 2009; Seo et al. 2010), and the displacement is larger for more negative n.

The seemingly quite different argument of Crocce & Scoccimarro (2008) leads to a similar expression for the peak shift. They propose modeling the non-linear correlation function in the neighborhood of the bump by

$$\xi_{\rm NL}(r) \approx \xi(r) + A_{\rm mc} \frac{d\xi(r)}{dr} \frac{r\,\bar{\xi}(r)}{3} \ , \tag{2.19}$$

where the mode-coupling factor $A_{\rm mc}$ can be treated as a fitting parameter but the value 34/21 obtained from PT is in fact close to the best-fit numerical value (see Crocce et al. (2010), Appendix A). With judicious use of Taylor expansions in the limit of small shift and minimal non-linear broadening, one can derive

$$\frac{r_{\rm peak}}{r_{\rm bao}} \approx 1 + \frac{34}{21} \frac{C_n}{n} \left(\frac{r_0}{r_{\rm bao}}\right)^{n+3} \ , \tag{2.20}$$

hence a shift about 50% larger than Eq. (2.18) but with the same dependence on r_0 and n.

Dashed lines in Figure 2.6 show the prediction of Eq. (2.18). The model correctly predicts that the shift is much larger for $n = -1.5$ than for $n = -1$ or $n = -0.5$. For $n = -1.5$, it tracks the numerically measured shift remarkably well. For the other n values, it predicts too large a shift for $r_0 > 0.1 r_{\rm bao}$; at smaller r_0, the model is consistent with the numerical results within the error bars, but the numerical results are also consistent with zero shift. Note that this treatment does not include the 1-loop PT extension of Smith et al. (2008)'s model, which could improve agreement at later epochs.

Figure 2.7 compares Eq. (2.20) to the first two outputs of the $n = -1.5$ simulations. For $r_0/r_{\rm bao} = 0.024$, this model predicts the distortion in the neighborhood of the peak remarkably well, with no free parameters. Note that there is a clear non-linear shift of the peak at this output, despite the low value of $\sigma_8 = 0.5$. For $r_0/r_{\rm bao} = 0.061$, the model predicts too large a distortion. However, if I insert the broadened and lower amplitude bump (taking $\sigma_{\rm bao}$ and $A_{\rm bump}$ from the model discussed in the previous section) into the calculation of Eq. (2.20), an approach that seems reasonable but is not rigorously justified, then I get the dashed green lines in Figure 2.7, which agrees much better (though not perfectly) with the numerical results.

I conclude that these analytic approaches can explain why the shift in the bump location is much larger for $n = -1.5$ and can capture at least some of the quantitative behavior of the peak shift. However, they do not work accurately over a wide range of $r_0/r_{\rm bao}$ and n. I will return to the comparison of PT predictions and the numerical results in §3.4, in the context of the power spectrum.

2.4 Self-Similar Tests

In an $\Omega_m = 1$ pure powerlaw model, i.e. $P(k) = Ak^n$, since the only scale germane to the problem is the amplitude, A, the evolution of clustering statistics should depend only on the value of A or some derived variable such as $k_{\rm NL} = (2\pi^2/A)^{1/(n+3)}$. The evolution may be different for each powerlaw but with n fixed there should be a unique function (e.g. of $k/k_{\rm NL}$, or $r/R_{\rm NL}$, or $M/M_{\rm NL}$, ...) that fully describes any given clustering statistic, even well into the non-linear regime. In the early days of cosmological N-body investigations, demonstrations of self-similar evolution with pure powerlaw cosmologies, in addition to providing physical insight, also gave decisive confirmations of the accuracy of simulations (e.g. Efstathiou et al. 1988; Bertschinger & Gelb 1991; Lacey & Cole 1994; Jain et al. 1995; Colombi et al. 1996). I take advantage of the simplicity of the powerlaw times a gaussian setup to perform self-similar tests that can be used in an analogous way to test the accuracy of the simulations on the scale of the bump.

The powerlaw times a bump setup clearly has two scales at play instead of one, so in this case, for a given powerlaw and a given initial bump width, the non-linear dynamics should evolve only as a function of the ratio of the non-linear scale to the BAO scale. The dynamics are self-similar in the sense that any property of the system, such as the broadening of the bump or the shift in the peak for a particular powerlaw, is determined by how close the non-linear scale, r_0, has come to the

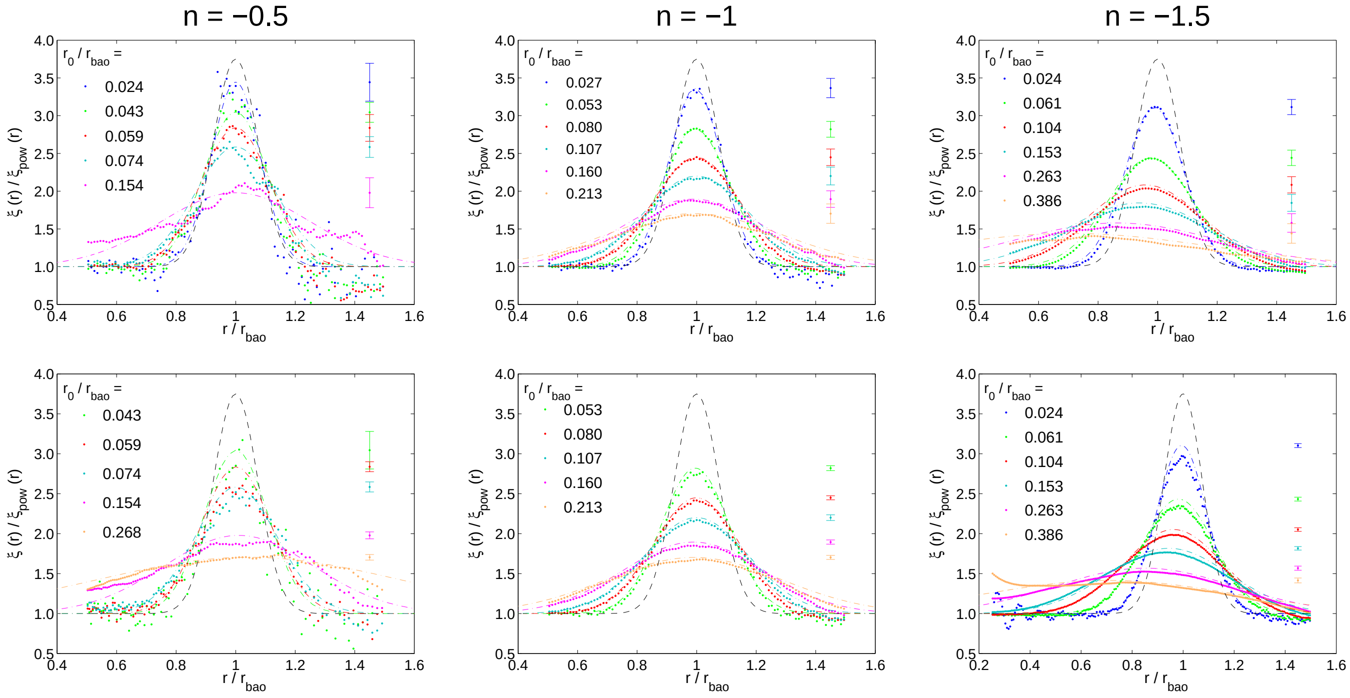

Figure 2.8: Tests of robustness to numerical parameters. (*Top*) Comparison of the bump region of $\xi(r)$ in simulations with $r_{\rm bao}/L_{\rm box} = 1/10$ (points) to the gaussian fits (lines) from the fiducial simulations in Fig. 2.3, which have $r_{\rm bao}/L_{\rm box} = 1/20$. (*Bottom*) Comparison of simulations with $r_{\rm bao}/L_{\rm box} = 1/20$ but 256^3 particles, hence $r_{\rm bao}/n_p^{-1/3} = 12.5$, to the fiducial simulations with 512^3 particles and $r_{\rm bao}/n_p^{-1/3} = 25$.

BAO scale. Unlike a ΛCDM simulation the result should not, in principle, depend on whether the bump is initially set at, e.g., 100 h^{-1} Mpc or 130 h^{-1} Mpc; only the ratio of the non-linear scale to the BAO scale matters in determining the evolution. If the N-body results do depend, separately, on the BAO scale or the non-linear scale, this can be interpreted as a sign of numerical artifacts.

2.4.1 Robustness to Varying Box Size and Mean Interparticle Spacing

Cosmological N-body simulations unavoidably introduce two artificial scales into the problem – the box size, $L_{\rm box}$, and the initial mean interparticle spacing, $l_p = {n_p}^{-1/3} = L_{\rm box}/N^{1/3}$. Both of these scales can potentially interfere with the evolution of the BAO feature and bias one's results. In the upper panels of Fig. 2.8 I show results from tests where the BAO scale has been doubled (or equivalently the box-size halved), such that $r_{\rm bao}/L_{\rm box} \approx 1/10$ instead of the fiducial value of $r_{\rm bao}/L_{\rm box} \approx 1/20$ in the simulations shown elsewhere in the paper. The number of particles in this test is kept fixed at 512^3, so that the ratio of the BAO scale to the mean interparticle spacing increases from $r_{\rm bao}/{n_p}^{-1/3} = 25$ (as in the fiducial simulations) to 50. I also show tests (lower three panels) where the box size is kept fixed while the number of particles is decreased to 256^3, arguably more akin to a conventional convergence test. In each panel I plot the best-fit gaussians from the fiducial set of simulations. Note that for the "double-the-bump" tests in the upper panels of Fig. 2.8, these simulations had to be run for much longer than in the fiducial case in order for the non-linear scale to approach the BAO scale, which had been placed at twice the fiducial separation.

To the extent that the simulations in Fig. 2.8 match the fit from the fiducial set of simulations, the evolution can be said to be self-similar and unaffected by the artificially-introduced numerical scales. For the double-the-bump tests, the results seem to match the fiducial simulations well. In this case, especially for $n = -1.5$, the integral-constraint correction to $\xi(r)$ discussed in Appendix B is critical. I interpret this agreement as an indication that $r_{\rm bao}/L_{\rm box} \lesssim 1/10$ is acceptable if one includes integral-constraint corrections. Note that the measured errors on the mean are larger for these tests, which measure the correlation function on scales closer the box scale than in the fiducial simulations. These larger errors are consistent with expectations from Gaussian statistics in a finite volume Cohn (2006).

The 256^3 test was not quite as successful. The accelerated attenuation of the bump in the $n = -1.5$ case is severe enough to be of particular concern, especially since this setup is the one which actually sees an appreciable change in the BAO peak. The $n = -1$ simulations agree much better but still slightly underpredict the bump height. This also seems to be the case with the $n = -0.5$ results, which are more noisy. Though not quite a failure, I interpret this test to recommend keeping $r_{\rm bao}/{n_p}^{-1/3} \gtrsim 25$, as in the fiducial set of simulations.

The tests in Fig. 2.8 show that the evolution of the bump – its flattening, its movement in the $n = -1.5$ case, the lack of movement in the $n = -0.5$ and -1 cases, and the unexplained behavior of the bump area in the $n = -0.5$ case – is robustly predicted even when numerical parameters are changed substantially. For the wider importance of using BAO to constrain cosmology, this

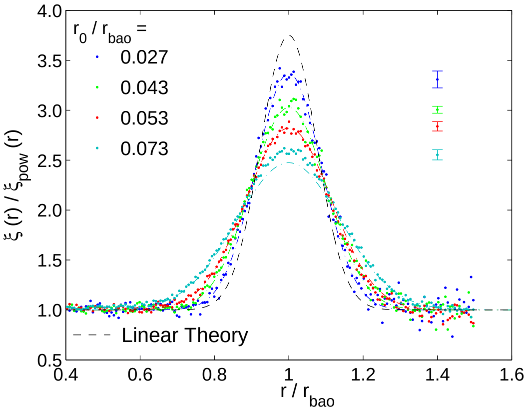

Figure 2.9: Results for a model including a cosmological constant ($\Omega_m = 0.3$, $\Omega_\Lambda = 0.7$) and with an $n = -1$ background powerlaw. The first and third outputs (blue and red) are directly comparable to the first and second outputs of the fiducial $n = -1$ simulations; thus the gaussian fits to those outputs in the fiducial case are overplotted. The second and last outputs (green and cyan) are compared to extrapolations from the fiducial $n = -1$ case assuming no non-linear shift and a model for the bump evolution as described in § 2.3.3.

is an encouraging sign that modest N-body simulations can accurately render the non-linear shift of the BAO peak with very different models for the broad-band clustering. For power spectra that span a much wider range than ΛCDM models, numerical parameters $r_{\rm bao}/L_{\rm box} \lesssim 1/10$ and $r_{\rm bao}/n_p^{-1/3} \gtrsim 25$ appear to be adequate.

2.4.2 A Test with Dark Energy

In this section, simulations including a cosmological constant ($\Omega_m = 0.3, \Omega_\Lambda = 0.7$) are presented and connected to the conclusions in previous sections. The evolution of the bump, if evolving self-similarly, should only depend on the ratio of $r_0/r_{\rm bao}$, so that the effect of dark energy would only be to change how quickly the non-linear scale grows and reaches a certain value. The introduction of dark energy in principle breaks self-similarity by defining a characteristic time (when Ω_m and Ω_Λ are equal), but in linear perturbation theory and the quasi-linear Zel'dovich and adhesion (Gurbatov et al. 1989; Weinberg & Gunn 1990) approximations, evolution is determined only by the linear growth factor, with no direct dependence on $\rho_m(a)$ or $\rho_{\rm DE}(a)$. Zheng et al. (2002) and Nusser & Colberg (1998) demonstrate that this dependence on the linear growth factor alone remains a very good approximation in fully non-linear N-body simulations, the latter also showing explicitly that the full equations of motion for cosmological perturbations are weakly dependent on the individual values of Ω_m and Ω_Λ when those equations are expressed using the linear growth factor as the time variable.

Fig. 2.9 compares these expectations to the N-body simulation results by presenting the evolved bump in a set of simulations ($n = -1$) that include a cosmological constant in comparison to the gaussian fits to the fiducial simulations. For some outputs, I have interpolated between outputs of the fiducial simulations assuming the model for the bump evolution discussed in § 2.3.3. A substantive difference between $\Omega_m = 1$ and dark energy models is that the growth of structure "freezes out" as dark energy becomes the dominant component of the universe. The last output in Fig. 2.9 is very close to this "freeze-out" limit in the linear theory growth function, which prevents r_0/r_{bao} from growing beyond 0.073 in this case.

The gaussian fits to the fiducial simulations agree well with the simulation results in Fig. 2.9, even for the last output which, with considerable computational expense, was evolved very close to the freeze-out limit. This confirms the expectations of self-similar evolution for this setup even in cosmologies with dark energy.

2.5 Evolution of the BAO feature in Fourier Space

2.5.1 Power Spectrum Estimation

Power spectra were determined for the $n = -0.5, -1$ and -1.5 models by mapping the particles onto a 1024^3 grid using the cloud in cell (CIC) assignment scheme. Performing a discrete fast fourier transform on this grid yields $\hat{\delta}(\vec{k})$ and fourier amplitudes $P(\vec{k}) = |\hat{\delta}(\vec{k})|^2$. The artificial smoothing introduced by the gridding scheme is corrected for by dividing $P(\vec{k})$ by the appropriate assignment function for CIC (Hockney & Eastwood 1981), and the corrected $P(\vec{k})$ is binned in k to yield $P(k)$. Following Heitmann et al. (2010) I do not include any kind of shot noise correction (e.g Jing 2005; Colombi et al. 2009), and I follow their advice in trusting the computed power spectra only up to half the *particle* nyquist wavenumber, as indicated with black dotted vertical lines in Fig. 2.10, which presents the primary power spectrum results. The power spectrum up to this k-value should be negligibly affected by the aliasing of the 1024^3 grid. Notwithstanding the conservative decisions in measuring $P(k)$, I will argue in the next section that a simple phenomenological model that draws on results from pure powerlaw simulations (Appendix A) allows these predictions to be extended to much higher k for the early outputs.

I report power spectra throughout, normalizing the wavenumbers by $k_{\mathrm{bao}} = 2\pi/r_{\mathrm{bao}}$, and giving the power spectrum amplitudes in terms of $P(k)/r^3_{\mathrm{bao}}$. This reflects the self-similar nature of the problem and allows more straightforward identification of the k-values of various nodes and anti-nodes. For technical reasons I throw out the measurements of the spectral power for $k \approx 2\pi/L_{\mathrm{box}}$, which should be computed separately from measurements at higher k because of the different statistics of mode-counting near the scale of the box. The power on these scales is also inevitably noisy because of the small number of modes.

Figure 2.10: *Left column*: Measured power spectra for the fiducial $n = -0.5$ (top), $n = -1$ (middle) and $n = -1.5$ (bottom) simulations. The x-axis is shown normalized to the scale of the BAO feature, $k_{\rm bao} = 2\pi/r_{\rm bao}$ and the y-axis is likewise shown as a dimensionless quantity, $P(k)/r_{\rm bao}^3$. There is no correction for shot noise; the shot noise level is indicated with dot-dashed lines. *Right column*: Results from dividing by the linear theory pure powerlaw. In both columns a phenomenological model (Eq. 2.21, solid colored lines) is compared to the simulation results. The scale corresponding to half the particle nyquist wavenumber is indicated with a vertical black dotted line.

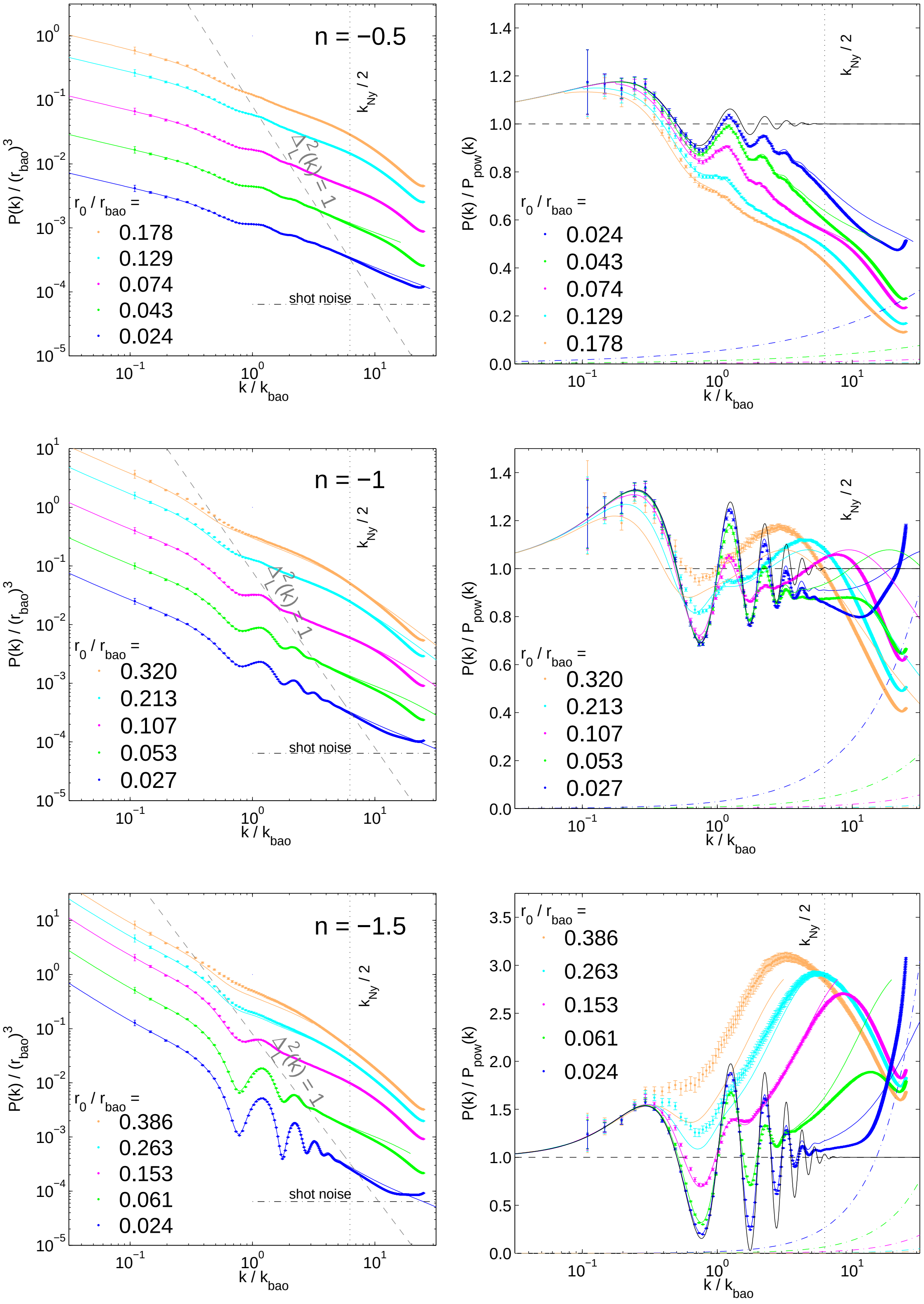
n = −0.5
n = −1
n = −1.5
P(k) / (r_bao)^3
P(k) / P_pow(k)
k / k_bao
k_Ny / 2
Δ^2(k) = 1
shot noise
r_0 / r_bao =
0.178
0.129
0.074
0.043
0.024
0.320
0.213
0.107
0.053
0.027
0.386
0.263
0.153
0.061
0.024
10^−1
10^0
10^1
10^−5
10^−4
10^−3
10^−2
0.0
0.2
0.4
0.6
0.8
1.0
1.2
1.4
0.5
1.5
2.0
2.5
3.0
3.5

Figure 2.10:

2.5.2 Interpretation

Ignoring the wiggles in Fig. 2.10 for a moment and focusing on the evolution of the overall shape of the power spectrum, the results are bracketed by the $n = -0.5$ spectrum, which trails behind the linear theory powerlaw at high k, and the $n = -1.5$ spectrum, which clearly outpaces the linear theory clustering prediction. This behavior is expected from perturbation theory (Scoccimarro & Frieman 1996; Scoccimarro 1997), and the trend is more clearly shown in the pure powerlaw plots in Appendix A. Physically, the behavior of the $n = -0.5$ powerlaw is sometimes described as "previrialization" (Davis & Peebles 1977), where on small scales the clustering power is so high that as halos form they pull away from the expansion of the universe and the non-linear power spectrum falls behind the linear theory prediction. For much steeper powerlaws, like $n = -1.5$ or the high k spectrum of ΛCDM, the trend is the opposite; clustering power is "transferred" from large scales to smaller scales. The $n = -1$ spectrum lies between these two extremes, and its spectrum is above and below the linear theory prediction in different ranges (Appendix A).

With this in mind I modeled the power spectrum results with a phenomenological approach, treating separately the non-linear evolution of the pure powerlaw spectrum and modeling the wiggles by coupling the analytic solution in Eq. 2.10 with the diffusion model introduced in § 2.3.3. Thus, the model is

$$\begin{aligned} P_{\rm phen}(k) &= A_n r_0^3 (k r_0)^n f_n(k/k_{\rm NL}) \quad + \\ & 2^{5/2}\pi^{3/2} A'_{\rm bump}\sigma'_{\rm bao} r_{\rm bao}^2 \left(\frac{r_0}{r_{\rm bao}}\right)^{n+3} \frac{\sin(k\, r'_{\rm bao})}{k r'_{\rm bao}} e^{-k^2\sigma'^2_{\rm bao}/2}, \end{aligned} \tag{2.21}$$

where $\sigma'_{\rm bao}$ is from Eq. 2.15, and, as in § 2.3.3, the area under the bump is assumed to be constant, $A'_{\rm bump}\,\sigma'_{\rm bao} = A_{\rm bump}\,\sigma_{\rm IC}$. For the $n = -0.5$ and $n = -1$ cases I assume no shift of the BAO scale, $r'_{\rm bao} = r_{\rm bao}$, while for $n = -1.5$ I set the BAO scale using $r'_{\rm bao}/r_{\rm bao} = 1 - 1.08(r_0/r_{\rm bao})^{1.5}$, which is a good description of the motion of the peak in Fig. 2.6. For the pure powerlaw evolution I use non-linear fitting functions to pure powerlaw simulations, $f_n(k/k_{\rm NL})$, which are described in Appendix A. In Fig. 2.10 I show the predictions of the phenomenological model with solid lines up to the k-values where the fitting function is well determined by the pure powerlaw simulations.

This model works surprisingly well in the $n = -0.5$ case, given that the constant area approximation seems to break down in the later outputs (Fig. 2.5). The first few outputs of the $n = -1$ and $n = -1.5$ cases are also well matched by Eq. 2.21. For these first few outputs the phenomenological models may actually be more trustworthy than the simulation measurements: at high k the pure powerlaw spectrum dominates, and the non-linear fitting functions in this regime are defined preferentially from later outputs in the pure powerlaw simulations, which should be unaffected by transients from initial conditions or shot noise.

If the phenomenological model can be trusted at high k, the results for the first output shown in Fig. 2.10 can be extended to $k/k_{\rm bao} \sim 30$ for $n = -0.5$, $k/k_{\rm bao} \sim 600$ for $n = -1$, and $k/k_{\rm bao} \sim 50$

for $n = -1.5$. Assuming again that simulations can be trusted up to half the particle nyquist wavenumber, this is analogous to running simulations for this setup with $\sim 2400^3$, $\sim 48000^3$ and $\sim 4000^3$ particles respectively[9], assuming the same box size as the 512^3 simulations presented here.

At small k and late times there are significant deviations, however, between the phenomenological model and the $n = -1$ and $n = -1.5$ results. Those outputs have features, especially around $k \sim k_{\rm bao}$, that seem to be unaccounted for in Eq. 2.21. In the next section I compare the simulation results to expectations from perturbation theory.

2.5.3 Comparison with PT predictions

Because of the IR divergence of $\int P(q)\,dq$ for steep power spectra, perturbation theory schemes that use this term anywhere to renormalize the higher order expansions will necessarily be problematic for these setups. However, standard 1-loop PT (a.k.a. SPT) is still well defined for $n > -3$ (Vishniac 1983; Makino et al. 1992) and so, like Widrow et al. (2009) who explored pure powerlaw spectra, I show predictions for this approach and for the closely related SimpleRG scheme from McDonald (2007).

Although, the $n = -0.5$ and $n = -1$ cases are IR convergent for $\int P(q)\,dq$, they are still UV divergent. Through separating the powerlaw and wiggle terms I can avoid some of the cutoff dependence of the SPT predictions; the predictions shown for the $n = -1.5$ case should be completely cutoff independent, while $n = -0.5$ and $n = -1$ results are sensitive to the UV cutoff. In what follows I choose $k_{\rm max}/k_{\rm bao} \approx 160$, but my qualitative conclusions would be unchanged even if this high-k cutoff were increased by a factor of two. I calculate PT predictions by modifying the publicly-available copter code from Carlson et al. (2009) to better accommodate powerlaw cosmologies and this setup.

The primary PT results are presented in Fig. 2.11. At each output predictions are shown up to $k_{\rm NL}$, roughly the scales where these schemes are expected to break down. Generally, SimpleRG and SPT/SPT+ give fair-to-good predictions for the non-linear damping of the wiggles (as discussed below SPT+ uses the non-linear fitting functions in Appendix A for the powerlaw evolution). The good comparison with the simulations for the $n = -1.5$ case suggests that the non-linear shift can be adequately captured by PT. An exception to this is clearly the SPT+ predictions for the $n = -0.5$ case, which seem to significantly overpredict the damping of the BAO feature. I discuss the SPT/SPT+ predictions in more detail in the next section, breaking up the calculation into different “interaction” terms in an effort to gain insight into the non-linear physics. Predictions from the SimpleRG scheme in Fig. 2.11 were not calculated by breaking up $P_{\rm IC}(k)$ in this way since SimpleRG does a much better job than SPT in predicting the evolution of pure powerlaw spectra (Widrow et al. 2009).

---

[9] The extraordinary value for the $n = -1$ case comes from the high k fitting function from Widrow et al. (2009).

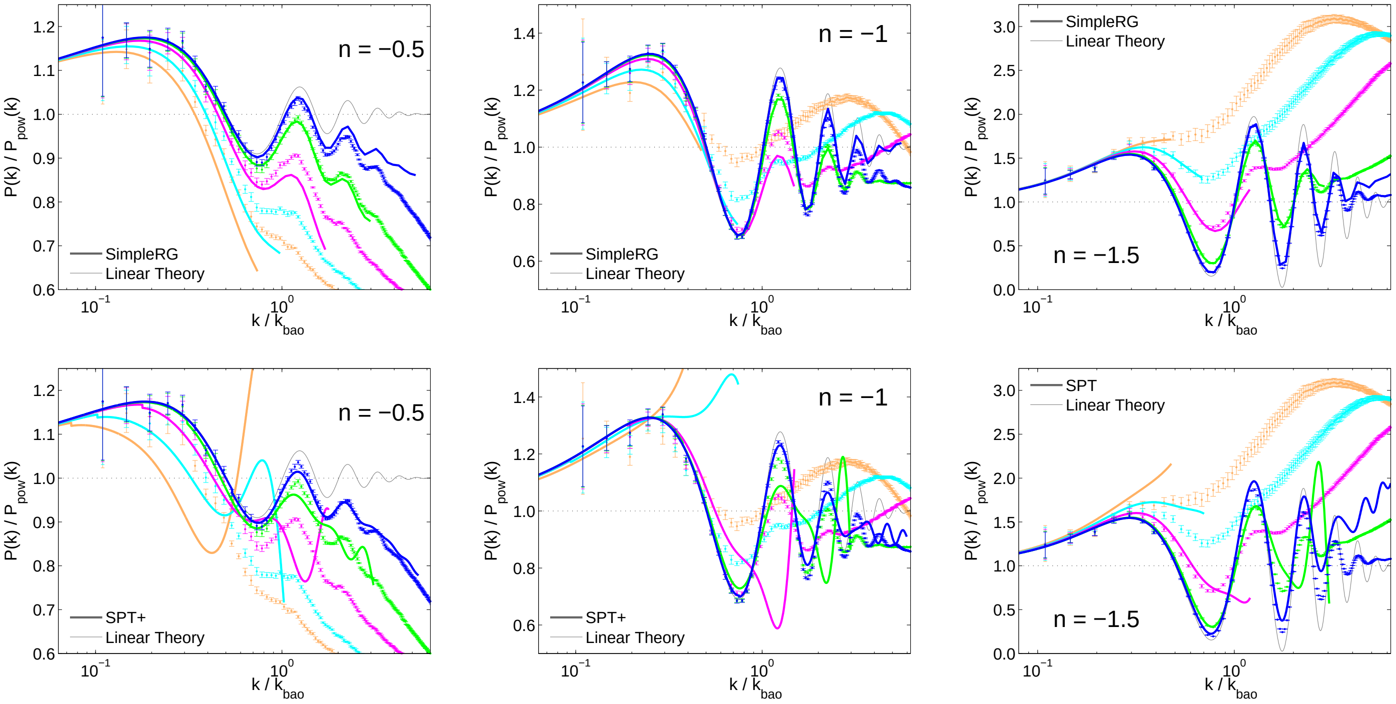

Figure 2.11: A comparison of power spectrum results from Fig. 2.10 with quasi-linear predictions from standard perturbation theory (SPT/SPT+, dashed lines) and the SimpleRG scheme (dot-dashed lines) from McDonald (2007). SPT+ treats the pure powerlaw evolution differently than SPT, using a fit to pure powerlaw simulation results (Appendix A) instead of the SPT prediction for the pure powerlaw evolution (Scoccimarro & Frieman 1996). In each plot the x-axis limits are set to include the low k measurements from simulations up to half the particle nyquist wavenumber, approximately the regime where the N-body results should be accurate.

2.5.4 SPT and SPT+

The 1-loop correction to the linear theory power spectrum is given by Makino et al. (1992)

$$P(k) = P_L(k) + P_{22}(k) + P_{13}(k) \tag{2.22}$$

where

$$\begin{aligned} P_{22}(k) = \; & \frac{k^3}{98\,(2\pi)^2} \int_0^\infty dr P_L\,(kr) \int_{-1}^{1} dx \; \times \\ & P_L\left[k\left(1+r^2-2rx\right)^{1/2}\right] \frac{\left(3r+7x-10rx^2\right)^2}{\left(1+r^2-2rx\right)^2} \end{aligned} \tag{2.23}$$

and

$$\begin{aligned} P_{13}(k) = \; & \frac{k^3 P_L(k)}{252\,(2\pi)^2} \int_0^\infty dr P_L(kr) \Big[\frac{12}{r^2} - 158 + 100r^2 \\ & -42r^4 + \frac{3}{r^3}\left(r^2-1\right)^3 \left(7r^2+2\right) \ln\left|\frac{1+r}{1-r}\right|\Big]. \end{aligned} \tag{2.24}$$

Notice that in $P_{22}(k)$ and $P_{13}(k)$ the linear power spectrum appears twice, and as a result these terms increase in amplitude as the linear growth function to the fourth power.

For pure powerlaw spectra, by including UV & IR cutoffs and using sufficient care to avoid the singularity in the denominator of the kernel in $P_{22}(k)$, these integrals can be computed analytically (Scoccimarro & Frieman 1996; Makino et al. 1992). In principle, it may also be possible to obtain an exact solution for 1-loop corrections to the analytic expression for $P_{\rm IC}(k)$ in Eq. 2.10, but the complexity of the $P_{22}(k)$ kernel is difficult to overcome or approximate.

To organize the calculation and for the most clarity in physical interpretation, I calculate the 1-loop corrections by treating separately the "interaction"[10] terms that arise from inserting $P_L(k) = P_{\rm pow}(k) + P_{\rm wig}(k)$ (Eq. 2.4) in $P_{22}(k)$ and $P_{13}(k)$,

$$\begin{aligned} P_{22}(k) = \frac{k^3}{98(2\pi)^2}\Big[& \int dr P_{\rm pow}(kr) \int dx P_{\rm pow}\left[k(1+r^2-2rx)^{1/2}\right] f_{22}(r,x) \\ & + 2\int dr P_{\rm pow}(kr) \int dx P_{\rm wig}\left[k(1+r^2-2rx)^{1/2}\right] f_{22}(r,x) \\ & + \int dr P_{\rm wig}(kr) \int dx P_{\rm wig}\left[k(1+r^2-2rx)^{1/2}\right] f_{22}(r,x) \Big], \end{aligned} \tag{2.25}$$

and likewise

$$\begin{aligned} P_{13}(k) = \frac{k^3}{252(2\pi)^2}\Big[& P_{\rm pow}(kr) \int dr P_{\rm pow}(kr) f_{13}(r) + P_{\rm pow}(kr) \int dr P_{\rm wig}(kr) f_{13}(r) \\ & + P_{\rm wig}(kr) \int dr P_{\rm pow}(kr) f_{13}(r) + P_{\rm wig}(kr) \int dr P_{\rm wig}(kr) f_{13}(r)\Big], \end{aligned} \tag{2.26}$$

where $f_{22}(r,x)$ and $f_{13}(r)$ are short hand for the fully expressed kernels in Eqs. 2.23 & 2.24. For the

---

[10] Alluding to the resemblance between SPT and Feynman integrals in particle physics

terms where $P_{\rm pow}(k)$ appears twice – a.k.a. the powerlaw-powerlaw interactions – this result can be looked up in Scoccimarro & Frieman (1996) or computed using their approach. But since those results are often cutoff dependent and/or in poor agreement with simulations, I can potentially replace the powerlaw-powerlaw interactions and the linear theory powerlaw with a fitting function from pure powerlaw simulations, while still treating the remaining terms in $P_{22}(k)$ and $P_{13}(k)$ without any approximation. In Fig. 2.11 this approach is dubbed "SPT+" while "SPT" refers to treating the powerlaw-powerlaw interactions as in Scoccimarro & Frieman (1996). I discuss the remaining interaction terms in the next two sections.

2.5.5 Powerlaw-Wiggle Interactions

Eqs. 2.25 & 2.26 contain three terms that include both $P_{\rm pow}(k)$ and $P_{\rm wig}(k)$. Since these terms include dimensionless factors of $(r_0/r_{\rm bao})^{n+3}$, whereas in the remaining "wiggle-wiggle" interaction terms there appear factors of $(r_0/r_{\rm bao})^{2(n+3)}$, at fixed $r_0/r_{\rm bao}$ these powerlaw-wiggle interaction terms will generally give larger corrections to $P_L(k)$ than the "wiggle-wiggle" interactions, which are discussed in the next section. The powerlaw-wiggle terms were evaluated numerically to obtain the SPT & SPT+ results in Fig. 2.11. The $P_{13}(k)$ powerlaw-wiggle interactions are given by

$$\begin{aligned} P_{13,\text{pow-wig}}(k) \ = & \\ & \frac{k^3}{252(2\pi)^2}\Bigg[P_{\rm wig}(kr)\int dr P_{\rm pow}(kr) f_{13}(r) \\ & \qquad + P_{\rm pow}(kr)\int dr P_{\rm wig}(kr) f_{13}(r)\Bigg]. \end{aligned} \tag{2.27}$$

For the second term in Eq. 2.27, since $P_{\rm wig}(k)$ is exponentially damped at high k and $P_{\rm wig}(k) \rightarrow$ constant for $k \rightarrow 0$, the result is cutoff independent. By using an approximation to the $P_{13}(k)$ kernel one can obtain a remarkably accurate approximate solution for this expression, which will be explained in the section on "wiggle-wiggle" interactions where this integral also appears.

The integral in the first term in Eq. 2.27 also appears in the calculations of Scoccimarro & Frieman (1996) for a variety of powerlaws. In this case IR divergences might be expected to be problematic, but, as explained by Makino et al. (1992), for steep powerlaws the IR divergence cancels with a corresponding term in $P_{22}(k)$ (in the present context the powerlaw-wiggle term in Eq. 2.25) yielding finite results for $n > -3$. Unfortunately, there are still UV divergences for the $n = -0.5$ and -1.0 cases. I integrate up to $k_{\rm max}/k_{\rm bao} \approx 160$ in the results presented here.

The last powerlaw-wiggle interaction term, as just mentioned, is the second term in Eq. 2.25. This term has a factor of two in front of it because a symmetry in the $P_{22}(k)$ kernel implies that if $P_{\rm pow}(k)$ and $P_{\rm wig}(k)$ are interchanged the result of the integral remains the same. I use this property to cross check the numerical integration of this term. Although I was unable to find an approximate analytic solution for this term, note that the dx integral can be computed analytically using the approximation $P_{\rm wig}(k) \sim \sin(kr_{\rm bao})/k$ and with a substitution of variables. This approximation is

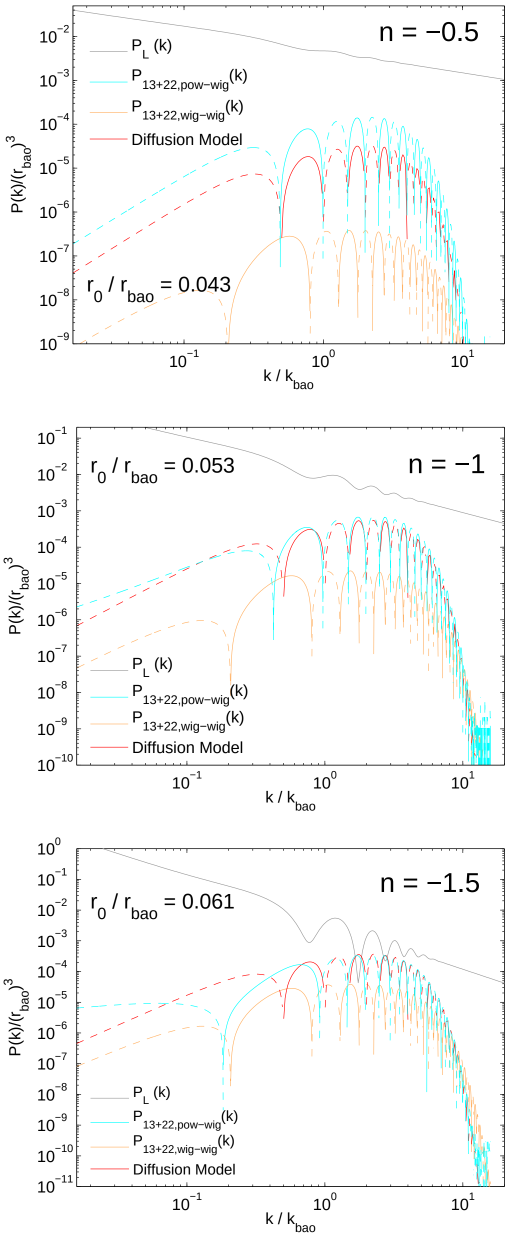

Figure 2.12: Results for the powerlaw-wiggle interactions (cyan) and the wiggle-wiggle interactions (orange) for the three different powerlaw setups. Expectations from the diffusion model coupled with an analytic approximation for $P_{\rm IC}(k)$ in the $r_0/r_{\rm bao} \ll 1$ limit are shown for comparison in red. Positive corrections are shown in solid lines, negative corrections are shown in dashed lines. Note that for clarity the $n = -1.5$ plot is shown at the first output; the $n = -0.5$ and -1 plots are shown at the second output, which allows easier visual comparison with the linear theory power spectrum.

valid for $k \ll \sigma_{\rm bao}^{-1}$, still a relatively wide and interesting range of k.

The results for the powerlaw-wiggle interactions are shown in cyan lines alongside the linear theory spectrum (gray solid lines) in Fig. 2.12. Also shown (in orange) are the wiggle-wiggle interactions discussed in the next section. A negative correction in this plot is shown with dashed lines, while positive corrections are shown with solid lines. Qualitatively, the results indicate that the powerlaw-wiggle interactions are approximately out of phase with linear theory and push and pull the wiggles in the right places to dampen out the BAO feature. A possible exception to this is the low k correction for $n = -1.5$, but, in fact, the wide positive correction around $k/k_{\rm bao} \sim 0.5$ seems to explain the extra power seen on those scales in the simulation results (Fig. 2.10), which was not captured by the phenomenological model in Eq. 2.21.

For a more quantitative comparison to the powerlaw-wiggle results, Fig. 2.12 shows a model inspired by the diffusion behavior seen in the correlation function. If I suppose that the bump broadens out as in Eq. 2.15 and place this ansatz for $\sigma^2_{\rm bao}(r_0)$ in the phenomenological model in Eq. 2.21, then in the limit where $r_0/r_{\rm bao}$ is small I expect the wiggles to evolve as

$$\begin{aligned} P_{\rm wig}(k, r_0)/r_0^{n+3} &\sim e^{-k^2\sigma^2_{\rm bao}(r_0)/2}\frac{\sin(kr_{\rm bao})}{k} \\ &\approx e^{-k^2\sigma^2_{\rm IC}/2}\frac{\sin(kr_{\rm bao})}{k} \\ &\quad -k^2 r_{\rm bao}^2\kappa_n\left(\frac{r_0}{r_{\rm bao}}\right)^{n+3} e^{-k^2\sigma^2_{\rm IC}/2}\frac{\sin(kr_{\rm bao})}{k}. \end{aligned} \tag{2.28}$$

Notice that since the linear theory wiggles grow in amplitude as the linear growth function squared (i.e. $r_0^{n+3} \sim Aa^2$ in Eq. 3.14), the extra factor of r_0^{n+3} in Eq. 2.28 makes this correction grow as the linear growth function to the fourth power. This is the same dependence on the growth function as in SPT. I plot this expectation from the diffusion model – essentially $-k^2$ times the linear theory wiggles – alongside the powerlaw-wiggle results in Fig. 2.12. There are no free parameters to this comparison; κ_n takes the same value as in § 2.3.3, which gave a good fit to the correlation function results.

For the $n = -1$ and -1.5 cases the agreement with the diffusion model is quite good except for the caveat already mentioned with $n = -1.5$ for $k/k_{\rm bao} \sim 0.5$. For the $n = -0.5$ case, the shape of $P_{13+33,\text{pow-wig}}(k)$ agrees well with the diffusion model but the amplitude is about a factor of four larger. Fig. 2.12 suggests that the problem lies in the SPT+ prediction, which predicts too much damping of the BAO feature. (Increasing the high-k cutoff would predict more damping.)

Comparing the diffusion model, which oscillates as $-\sin(kr_{\rm bao})$ in Fig. 2.12, to the powerlaw-wiggle interactions also reveals a slight phase difference between $P_{13+22,\text{pow-wig}}(k)$ and the diffusion model expectations. This is most easily visible for $n = -1.5$ in Fig. 2.12, which seems to oscillate as $-\sin(kr_{\rm bao} + \varphi)$ where $\varphi \approx 0.2$, while this phase is closer to $\varphi \approx 0.1$ for $n = -1$ and is consistent with zero for $n = -0.5$. This result implies that, in addition to damping the BAO feature, the

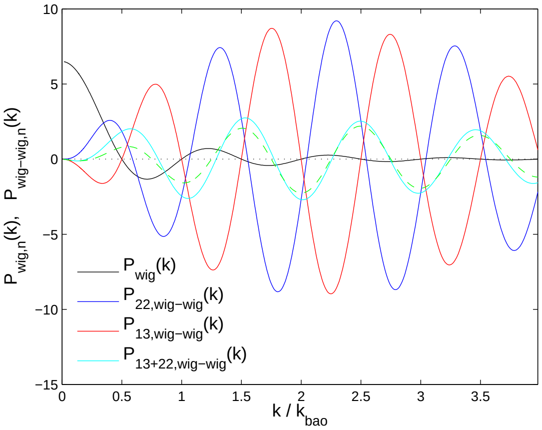

Figure 2.13: Highlighting the wiggle-wiggle interactions and showing, individually, $P_{13,\text{wig-wig}}(k)$ (red) and $P_{22,\text{wig-wig}}(k)$ (blue) which destructively interfere to produce the final result, $P_{13+22,\text{wig-wig}}(k)$ (cyan). Also shown for comparison are the linear-theory wiggles (Eq. 2.10) in black and a cosine function with a similar envelope and amplitude as $P_{13+22,\text{wig-wig}}(k)$. Note that the y-axis is normalized to be dimensionless and independent of powerlaw and epoch; see text for more details.

powerlaw-wiggle interactions provide a shift, since a Taylor expansion of $\sin(kr_{\text{bao}}/\alpha_{\text{shift}})$ yields

$$\sin(kr_{\text{bao}}/\alpha_{\text{shift}}) \approx \sin(kr_{\text{bao}}) - (\alpha_{\text{shift}} - 1)\cos(kr_{\text{bao}}) \tag{2.29}$$

and, without any approximation,

$$-\sin(kr_{\text{bao}} - \varphi) = -\cos\varphi\,\sin(kr_{\text{bao}}) - \sin\varphi\,\cos(kr_{\text{bao}}). \tag{2.30}$$

The last term on the right in Eq. 2.30 should provide the “push” to move the BAO feature to smaller scales, since $\sin\varphi \geq 0$ for the φ-values that match the numerical results.

2.5.6 Wiggle-Wiggle Interactions

Though suppressed by a factor of $(r_0/r_{\text{bao}})^{n+3}$ relative to the powerlaw-wiggle interactions, in Fig. 2.12 the wiggle-wiggle interactions are not completely negligible (at least for the $n = -1.5$ case), and by eye they appear about a half-period out of phase with the linear theory wiggles, just the kind of feature that gives rise to a shift of the BAO scale. I discuss these calculations in this section, with the convenience that because the functional form of $P_{\text{wig}}(k)$ is independent of n, the wiggle-wiggle interactions are also independent of n apart from the $(r_0/r_{\text{bao}})^{2(n+3)}$ term out front. Since $P_{\text{wig}}(k) \to$ constant at low k and $P_{\text{wig}}(k)$ decays rapidly to zero at high k, the integrals should be cutoff independent.

The task, then, is to evaluate the two remaining terms in Eqs. 2.25 & 2.26. I treat both terms numerically, but, fortuitously, a remarkably accurate solution can be obtained for $P_{13,\text{wig-wig}}(k)$.

Using $P_{\rm wig}(k) \sim \exp(-k^2\sigma_{\rm bao}^2/2)\sin(kr_{\rm bao})/k$, and by approximating the $P_{13}(k)$ kernel with $f_{13}(r) \approx -(352/5)\exp(-29r^2/11) - 488/5$ one can show that

$$\begin{aligned} &\int_0^\infty dr P_{\rm wig}(kr) f_{13}(r) \approx \\ &-\frac{176\,\pi}{5\,k}\mathrm{Erf}\left(\frac{\sqrt{11}k\; r_{\rm bao}}{\sqrt{116+22k^2\sigma_{\rm bao}^2}}\right) - \frac{244\,\pi}{5\,\mathrm{k}}\mathrm{Erf}\left(\frac{r_{\rm bao}}{\sqrt{2}\sigma_{\rm bao}}\right), \end{aligned} \tag{2.31}$$

which is accurate to better than 8% for all k and better than 1% for $k/k_{\rm bao} \gtrsim 0.6$. The minus signs in this result imply that, when multiplied by $P_{\rm wig}(k)$ to obtain $P_{13,\text{wig-wig}}(k)$ as in Eq. 2.26, the result will oscillate like $-\sin(kr_{\rm bao})$.

In Fig. 2.13, which shows the results for numerical integration of the wiggle-wiggle interactions, the y-axis has been normalized to be a dimensionless quantity that is independent of the powerlaw and epoch of interest, i.e.,

$$P_{\rm wig,n}(k) \equiv \frac{P_{\rm wig}(k)}{r_{\rm bao}^3}\left(\frac{r_{\rm bao}}{r_0}\right)^{n+3}$$

$$P_{\text{wig-wig,n}}(k) \equiv \frac{P_{\text{wig-wig}}(k)}{r_{\rm bao}^3}\left(\frac{r_{\rm bao}}{r_0}\right)^{2(n+3)}.$$

Clearly there is a great deal of destructive interference between $P_{13,\text{wig-wig}}(k)$ and $P_{22,\text{wig-wig}}(k)$ in Fig. 2.13. The sum of these terms, $P_{13+22,\text{wig-wig}}(k)$, which is of course much lower in amplitude than either $P_{13,\text{wig-wig}}(k)$ or $P_{22,\text{wig-wig}}(k)$, seems to oscillate at about a half-period out of phase with $P_{\rm wig}(k)$ as mentioned earlier. To highlight this I overplot with a green-dashed line a function proportional to $-\cos(kr_{\rm bao})$, which qualitatively follows the oscillations in $P_{13+22,\text{wig-wig}}(k)$ rather well. Since the $P_{22,\text{wig-wig}}(k)$ term seems to oscillate as $\sin(kr_{\rm bao} - \varphi)$ where φ is small and positive, when added to $P_{13,\text{wig-wig}}(k)$, which oscillates as $-\sin(kr_{\rm bao})$ and with a similar envelope, these waves interfere as

$$\begin{aligned} -\sin(kr_{\rm bao}) \;&+\; \sin(kr_{\rm bao} - \varphi) \\ &= \sin(kr_{\rm bao})(-1+\cos\varphi) - \sin\varphi\cos(kr_{\rm bao}) \\ &\approx -\sin\varphi\,\cos(kr_{\rm bao}). \end{aligned} \tag{2.32}$$

The green-dashed line, more specifically, shows this $-\cos(kr_{\rm bao})$ term multiplied by the analytically-derived envelope for $P_{13,\text{wig-wig}}(k)$ (i.e. Eq. 2.31 with appropriate constants and factors of k and including a factor of $\exp(-k^2\sigma_{\rm bao}^2/2)$ from $P_{\rm pow}(k)$) and divided by a factor of four (i.e. $\sin\varphi \approx 1/4$) to approximately match the amplitude of $P_{13+22,\text{wig-wig}}(k)$. This model is only approximate – for example, there seems to be some weak k-dependence of the phase φ in $P_{22,\text{wig-wig}}(k)$ – but, qualitatively, something like this phenomenological description must be going on.

This raises the question of whether, in SPT, the shift in the BAO scale comes primarily from the phase lag in the powerlaw-wiggle interactions or from $P_{13+22,\text{wig-wig}}(k)$. The answer, at least for $n = -1.5$ where the BAO scale moves significantly, is that the shift is similar in magnitude from both terms, and that both "push" the BAO scale in the same direction. Qualitatively, the same can be said for the $n = -1$ case, but the phase lag in the powerlaw-wiggle interactions is smaller and the $(r_0/r_{\rm bao})^{(n+3)}$-suppressed amplitude of wiggle-wiggle interactions is smaller still, so much less of a shift is expected. And in the $n = -0.5$ case there does not seem to be a phase lag in the powerlaw-wiggle interactions, while the wiggle-wiggle interactions are even more attenuated.

2.5.7 PT Results in Real Space

Returning to the SimpleRG scheme, which is closely related to SPT, I show the results from integrating the $P_{\rm SimpleRG}(k)$ predictions shown in Fig. 2.11 into two-point correlation functions in Fig. 2.14. Note that some of the outputs for the $n = -0.5$ case are omitted for clarity. At each output I apply a minimal damping to $P_{\rm SimpleRG}(k)$ to suppress noise and the influence of $P_{\rm SimpleRG}(k)$ for $k \gg k_{\rm NL}$ in the final result. Some PT schemes naturally include exponential damping in the predicted $P_{\rm QL}(k)$ (e.g. Matsubara 2008), which is advantageous for computing $\xi(r)$ from PT. SimpleRG (and SPT) do not naturally include these factors, so the results for $\xi(r)$ may not be as clean-looking as other schemes, even though the $P(k)$ predictions may be quite reasonable. In SPT, for example, the $P(k)$ predictions for $k \gtrsim k_{\rm NL}$ with the powerlaw-times-a-bump setup are often large and inaccurate or predict $P(k) < 0$ at some k. Therefore I do not show $\xi(r)$ predictions from SPT, which offer little insight in judging the accuracy of the scheme or in confirming the picture of how the BAO feature evolves as sketched out in the previous two sections.

With that disclaimer, the SimpleRG predictions do a good job of rendering the evolution of the BAO feature in configuration space (Fig. 2.14). In all cases the broadening and attenuation of the bump are qualitatively accounted for, including the $n = -0.5$ case that was problematic in SPT; the success of SimpleRG in this case may even help explain why the area of the bump is not as precisely conserved as in the other setups (Fig. 2.5). And in the $n = -1.5$ case, although noisy, SimpleRG does seem to accurately predict the shift in the BAO peak. With the close correspondence between SimpleRG and SPT, broadly speaking I interpret the success of SimpleRG in Figs. 2.11 & 2.14 and the typically sensible results for SPT discussed in the previous two sections to imply that perturbation theory can accurately capture the non-linear evolution of the BAO feature with this class of initial conditions.

2.6 Discussion and comparison with ΛCDM

2.6.1 ΛCDM-like Simulations

Having described and explained the non-linear evolution of the BAO-feature with the powerlaw setup in some detail, it is worth discussing the relevance of these results to the canonical ΛCDM cosmology. I approach this task first by simply assessing the resemblance of these results to ΛCDM.

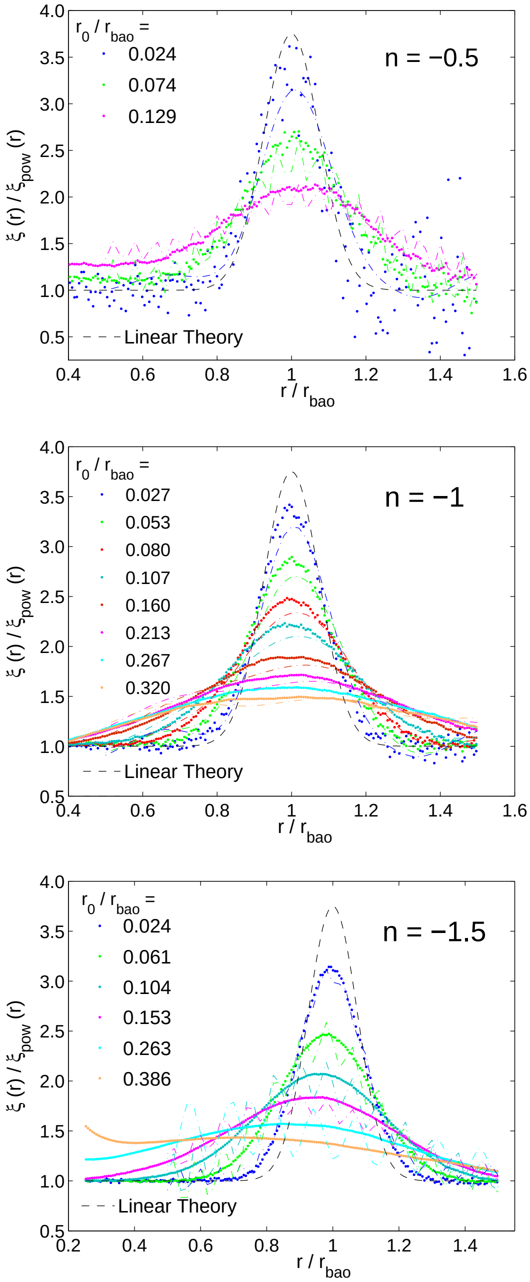

Figure 2.14: The results from fourier transforming the power spectrum predictions of SimpleRG (Fig. 2.11) into correlation functions (dot dashed lines), compared with the results from simulations (points). The fourier transform was performed with a small amount of damping in order to suppress noise and the influence of the power spectrum for $k \gg k_{\rm NL}$, well beyond the regime where SimpleRG is expected to be reliable.

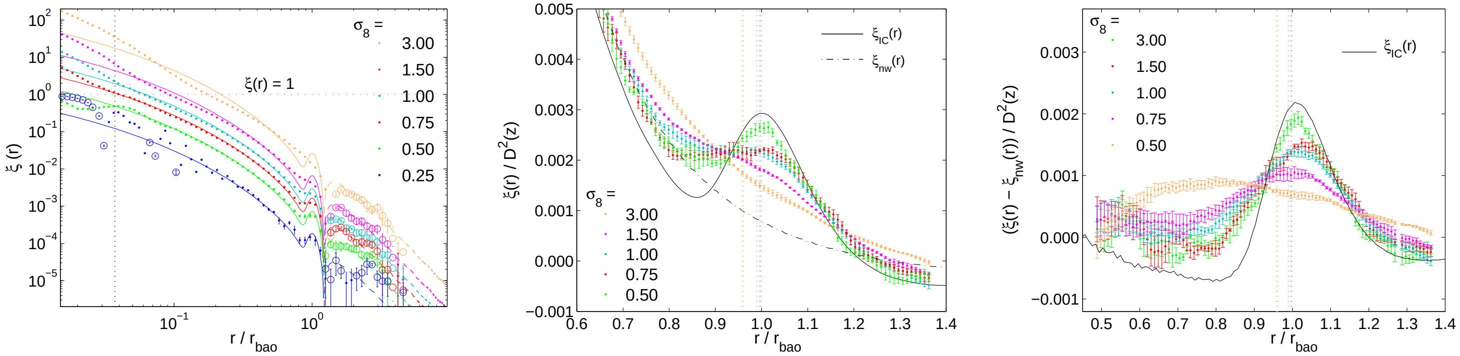

Figure 2.15: *Left panel*: The matter two-point correlation function results from four simulations using a canonical ΛCDM linear-theory power spectrum but evolving the initial conditions using $\Omega_m = 1$, $\Omega_\Lambda = 0$. The correlation function is shown at different epochs (points with error bars; solid when $\xi(r) > 0$, circles when $\xi(r) < 0$) with the linear theory correlation function overplotted (solid colored lines). The vertical dotted line shows the initial mean interparticle spacing. *Center panel*: The correlation function near the BAO scale. Vertical dotted lines show the expected shift from Seo et al. (2010) colored according to epoch. Also shown is the smooth $\xi_{\rm nw}(r)$ (black dot-dashed line) derived by fourier transforming $P_{\rm nw}(k)$ from Eisenstein & Hu (1998). *Right panel*: The result of subtracting $\xi_{\rm nw}(r)$ from the $\xi(r)$ measurements.

To aid in this comparison I performed a set of four simulations with an initial ΛCDM spectrum ($\Omega_m = 0.226$, $\Omega_\Lambda = 0.774$) as in Fig. 2.2 but evolved with $\Omega_m = 1$, $\Omega_\Lambda = 0$ so that σ_8 and $r_0/r_{\rm bao}$ in this case can avoid the freeze out limit and reach values comparable to the powerlaw setup. The ΛCDM-like simulations presented here were performed with essentially identical parameters as the earlier fiducial simulations in terms of box size, force resolution and number of particles. I show the primary $\xi(r)$ results in Fig. 2.15; the $r_0/r_{\rm bao}$ values for each output is shown in Table 2.2.

Table 2.2: ΛCDM outputs

$r_0/r_{\rm bao}$	σ_8
0.003	0.25
0.019	0.5
0.040	0.75
0.062	1.0
0.106	1.5
0.218	3.0

Fig. 2.15 is fairly unremarkable except that it shows the non-linear evolution of the correlation function in ΛCDM well past $z = 0$ and beyond the freeze out limit ($\sigma_8 \sim 1.3$). As in Fig. 2.1, the overall amplitude of the BAO feature at fixed $r_0/r_{\rm bao}$ is more similar to the $n = -0.5$ case than to the cases with more large scale power. The models for the non-linear shift from Seo et al. (2010), shown with vertical dotted lines in the center and right panels of Fig. 2.1, predict shifts of $3 - 4$ % when extrapolated to the final output[11]. The center panel also shows the smooth $\xi_{\rm nw}(r)$ correlation function, computed from a fourier transform of $P_{\rm nw}(k)$ from Eisenstein & Hu (1998), and in the right panel $\xi_{\rm nw}(r)$ is subtracted from the simulation data. In the center panel the combination of strong damping of the BAO feature and noise in the $\xi(r)$ measurement make any shift non-discernible. In the right panel the result of subtracting out $\xi_{\rm nw}(r)$ does visually resemble an attenuating gaussian (much more than $\xi(r)/\xi_{\rm nw}(r)$, which is not shown), but it is unclear whether the apparent drift of the BAO peak towards smaller scales, especially by the last output, is truly from the non-linear shift or whether the effect is simply from the changing broadband shape of $\xi(r)$. A plot of $(\xi(r) - \xi_{\rm pow}(r))/D^2(z)$ versus r from any of the fiducial simulations presented here would show a similar trend.

---

[11] The prediction depends on whether one assumes their $\alpha_{\rm shift} - 1 \propto D(z)^2$ formula, as expected from SPT, or instead uses their empirical fit where $\alpha_{\rm shift} - 1 \propto D(z)^{1.74}$. Fig. 2.15 shows the predictions of the $D(z)^2$ model. The empirical model is similar.

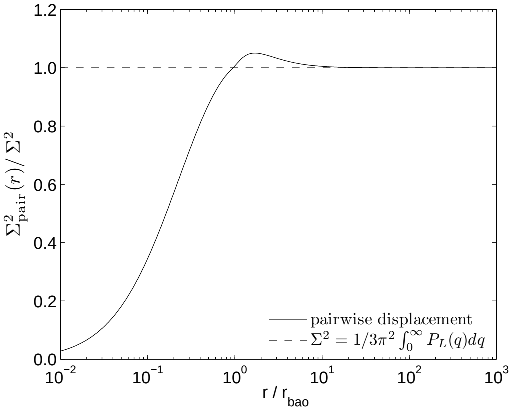

Figure 2.16: The rms pairwise displacement (Eq. 2.11; solid) at different scales using ΛCDM initial conditions divided by the commonly used rms displacement formula (Eq. 2.2; dashed), which includes the contribution from bulk motions. Both quantities scale as the linear growth function squared, so the result shown is independent of epoch.

2.6.2 Perturbation Theory and Modeling

In§ 2.5.2 I showed that a phenomenological approach matched the results from the fiducial simulations rather well. Eq. 2.21 bears a close resemblance to the damped-exponential models often used in the literature (e.g. Eisenstein et al. 2007; Seo et al. 2010), and I emphasize the conclusion that the broadening (damping) of the bump (wiggles) depends on the *pairwise* dispersion, $\Sigma^2_{\rm pair}$, rather than the rms displacement, Σ^2, which is sensitive to bulk motions. In Fig. 2.16, I compare $\Sigma^2_{\rm pair}/\Sigma^2$ on a wide range of scales for a ΛCDM spectrum (Fig. 2.2). Although I expect the two formulae to converge to the same result as $r \to \infty$, it is nevertheless surprising that $\Sigma^2_{\rm pair}(r_{\rm bao})$ differs by less than 2% from the Σ^2 displacement. In the literature there is no widespread agreement on how best to use Eq. 2.2 to predict the damping, and in practice Σ^2 is often a free parameter while other groups argue that an upper limit of $k = 4k_{\rm NL}$ in Eq. 2.2 is a better match to simulations (Crocce & Scoccimarro 2008). In this view, like that of Eisenstein et al. (2007), it is $\Sigma^2_{\rm pair}(r_{\rm bao})$ that matters physically, and the success of models based on Σ^2 is a lucky coincidence that holds in ΛCDM-like models but can fail, by an infinite factor, for powerlaw models.

Another widely-used phenomenological approach assumes a model for $P_{\rm NL}(k)$ motivated by Renormalized Perturbation Theory (RPT; Crocce & Scoccimarro 2006). In these models the non-linear shift comes directly from including $P_{22}(k)$ in the phenomenological form, or, in real space, from modeling the shift with the closely-related $\xi_{\rm mc}(r)$ ansatz and calibrating the amplitude of this term to N-body results (e.g. Sánchez et al. (2008); Montesano et al. (2010); Crocce et al. (2010)). Using this approach and a natural value for the amplitude of this term, in § 2.3.4 I showed that this approach adequately captures the shift in real space for the first output of the $n = -1.5$ case (when $\sigma_8 = 0.5$). By the second output (corresponding to $\sigma_8 = 1$), however, it fails, and although not rigorously justified by the derivation of the term, I argue that the formula would more accurately predict the shift if the broadening of the bump could be incorporated into $\xi_{\rm mc}(r)$. This may have been previously unnoticed because the shift in ΛCDM when $\sigma_8 \sim 1$ is smaller than the shift in the $n = -1.5$ case, and the amplitude of the bump, i.e., $\xi(r_{\rm bao})$, is significantly smaller in ΛCDM than in the $n = -1.5$ setup.

Finally, the success of the SimpleRG method (McDonald 2007) in matching the simulation results, both in fourier space and in real space, may certainly be informative to ongoing efforts to model the BAO evolution with *ab initio* predictions from PT. Carlson et al. (2009) show that this scheme also does a reasonable job in predicting the non-linear power spectra of ΛCDM and cCDM cosmologies. I ignored most other PT schemes (except SPT Makino et al. (1992)), which give divergent predictions for powerlaw cosmologies.

2.7 Summary

Motivated by the importance of accurate modeling of the BAO feature in large scale structure for interpreting the results of future dark energy experiments, I have used N-body simulations to investigate the evolution of a BAO-like feature in a simpler, alternative setting, where it modulates an underlying powerlaw initial power spectrum in an $\Omega_m = 1$ universe. Specifically, the initial conditions have a correlation function defined by Eq. 3.22, with a Gaussian multiplicative bump centered at scale $r_{\rm bao}$ and the amplitude $A_{\rm bump}$ and width $\sigma_{\rm bao}$ chosen in approximate agreement with ΛCDM expecations. The corresponding initial power spectrum follows Eq. 2.10 to an excellent approximation. For given values of $A_{\rm bump}$, $\sigma_{\rm bao}$, and the powerlaw spectral index n, non-linear matter clustering statistics (including the correlation function and power spectrum) should depend only on the ratio $r_0/r_{\rm bao}$, where r_0 is the correlation length defined by $\xi(r_0) = 1$. I evolve the simulations to values of $r_0/r_{\rm bao}$ much higher than traditional ΛCDM models, with final outputs corresponding to $\sigma_8 = 4.0\,(n = -1.5)$, $6.0\,(n = -1)$, and $12.0\,(n = -0.5)$ if I define a physical scale by setting $r_{\rm bao} = 100h^{-1}$Mpc. The standard simulations have box side $L_{\rm box}/r_{\rm bao} = 20$ and 512^3 particles. I use the simulations to develop physical intuition for BAO evolution and to test analytic descriptions in a regime far from that where they have been tested previously. In this respect, the spirit of my exercise is similar to the "crazy" CDM investigation of Carlson et al. (2009) and Padmanabhan & White (2009).

Consistent with ΛCDM studies, I find that the strongest effect of non-linear evolution on the BAO feature in $\xi(r)$ is to flatten and broaden the bump, with $A_{\rm bump}$ decreasing and $\sigma_{\rm bao}$ increasing. To a good approximation, failing only at late times in the $n = -0.5$ model, the area of the Gaussian bump, proportional to $A_{\rm bump} \times \sigma_{\rm bao}$, remains constant, which suggests that pairs are "diffusing" out of the shell corresponding to the initial BAO feature (see the physical description of Eisenstein et al. (2007)). The evolution of the bump width is well described by a model in which the non-linear $\sigma_{\rm bao}$ is the quadrature sum of the initial width and a length proportional to $\Sigma_{\rm pair}$, the rms relative displacement (computed from linear theory) of pairs separated by $r = r_{\rm bao}$. The constant of proportionality varies with n, but the same constant that describes the standard $n = -1$ model also describes the faster evolution of an $n = -1$ model with a "skinny" initial bump, supporting the validity of the diffusion interpretation. I emphasize that it is $\Sigma_{\rm pair}$ rather than the rms absolute displacement Σ that is relevant to analytic descriptions of these models. The latter quantity has an infrared divergence for $n \leq -1$, but this divergence corresponds to bulk translations induced by very large scale modes, which cannot affect the BAO peak itself. I think that the appearance of Σ rather than $\Sigma_{\rm pair}$ in many analytic models of BAO evolution is at best an approximation restricted to CDM-like models with a turnover in $P(k)$; by coincidence, $\Sigma \approx \Sigma_{\rm pair}(r_{\rm bao})$ for ΛCDM.

The location of the BAO peak, defined by the scale $r_{\rm peak}$ of a Gaussian fit to the non-linear $\xi(r)$ divided by the linear theory powerlaw, stays constant within the statistical precision of the measurements for the $n = -0.5$ and $n = -1$ models, even when these are evolved to a highly non-linear stage where the bump amplitude has dropped by a factor of $\sim 4 - 10$ from its initial value. For $n = -1.5$, on the other hand, the peak location shifts to smaller r, an effect that is already noticeable at the first output ($r_0/r_{\rm bao} = 0.024$, equivalent to $\sigma_8 = 0.5$) and that grows to a 30% drop by $r_0/r_{\rm bao} = 0.386$ (equivalent to $\sigma_8 = 4.0$). The analytic models of Smith et al. (2008) and Crocce & Scoccimarro (2008) accurately predict that shifts should be much larger for $n = -1.5$ than for $n = -0.5$ and $n = -1$, and the Smith et al. (2008) model accurately describes the evolution of the peak location for $n = -1.5$. However, both models predict non-linear shifts in the $n = -0.5$ and $n = -1$ cases that are inconsistent with the simulation results at late times.

I carried out a number of additional numerical tests varying either numerical parameters or the physical model. The fiducial simulations have $L_{\rm box}/r_{\rm bao} = 20$ and an initial mean interparticle spacing smaller than $r_{\rm bao}$ by a factor of $r_{\rm bao}/n_p^{-1/3} = 25$. I found consistent results in simulations with $L_{\rm box}/r_{\rm bao} = 10$ and $r_{\rm bao}/n_p^{-1/3} = 50$, indicating that a box size ten times the BAO scale is acceptable. I found marginal discrepancies for 256^3 simulations with $r_{\rm bao}/n_p^{-1/3} = 12.5$. Success of the box size test and other internal consistency tests is achieved only because I include the integral constraint corrections described in Appendix B, which make a noticeable difference for $n = -1$ and an important difference for $n = -1.5$. In other tests, I show that BAO evolution is nearly identical in an $\Omega_m = 1$ model and a model with $\Omega_m = 0.3$, $\Omega_\Lambda = 0.7$ (and the same initial conditions) provided they are evaluated at the same value of $r_0/r_{\rm bao}$ (or, equivalently, the same value of the linear growth function).

For more thorough tests of analytic models, I turned to a Fourier space description using the non-linear matter power spectrum. A "phenomenological" model in which I combine numerical results for the non-linear power spectrum of a pure powerlaw model (Appendix A and references therein) with the gaussian fits to the evolution of the BAO bump in $\xi(r)$ gives a remarkably accurate description of the full non-linear outputs of the $n = -1$ and $n = -1.5$ models. This model assumes no shift of the $\xi(r)$ peak location for $n = -0.5$ and $n = -1$ and $r_{\rm peak}/r_{\rm bao} = 1 - 1.08(r_0/r_{\rm bao})^{1.5}$ for $n = -1.5$. The success of this model suggests that the BAO bump has little effect on the non-linear evolution of the underlying "smooth" power spectrum. At least for $r_0/r_{\rm bao} < 0.2$, I expect that this model is a *more* accurate description than the numerical $P(k)$ measurements themselves, since it draws on self-similar scaling results from pure powerlaw spectra that have wider dynamic range than my simulations.

I compared my simulation results to predictions of two *ab initio* analytic approaches, "standard" 1-loop perturbation theory (SPT; e.g. Vishniac (1983); Makino et al. (1992)) and the "simple renormalization group" (SimpleRG) scheme of McDonald (2007). SimpleRG provides a quite accurate description of the low-k evolution in all cases, including $n = -1.5$ where the peak location shifts significantly, and it produces good but not perfect agreement with the evolution of the $\xi(r)$ bump in configuration space. For SPT, I break up the terms into distinct "interactions" between the powerlaw and "wiggle" components of the linear power spectrum, both to obtain physical insight and in order to define a more accurate "SPT+" scheme that uses numerical results for pure powerlaw evolution and perturbation theory to describe the interaction terms that involve the "wiggle" spectrum. SPT alone gives a reasonable description of the early $P(k)$ outputs for $n = -1.5$, but on the whole SimpleRG is substantially more accurate and has a wider range of validity.

The high statistical precision achievable with future BAO surveys — with cosmic variance distance scale errors for $z > 1$ and redshift bins $\Delta z = 0.2$ (Seo & Eisenstein 2007) — puts stringent demands on theoretical models. Exploiting the power of these surveys will require large numerical simulations supplemented by the physical insight and modeling flexibility afforded by analytic methods. The simulation results presented here offer valuable "stress tests" of numerical and analytic approaches in regimes beyond those where they are usually applied, and they allow isolation of distinct physical effects. Two natural directions that I plan to explore in future work are the clustering of biased tracers — in particular the massive halos expected to host luminous galaxies — and the impact of redshift-space distortions on BAO measurement from galaxy clustering. I will also investigate the impact of the initial conditions algorithms, comparing the scheme advocated by Sirko (2005) for simulation ensembles to the traditional scheme of mean density boxes used here. The combination of future BAO surveys and improved theoretical models will lead, ultimately, to new insights on the energy and matter contents of the cosmos.

Chapter 3

REVISITING A NOVEL METHOD FOR RUNNING COSMOLOGICAL N-BODY SIMULATIONS

3.1 Introduction

Next generation astronomical surveys will demand increasingly precise predictions from theory in order to properly interpret observations and constrain the nature of dark energy. As emphasized by Annis et al. (2005), this will be a challenging task: inaccuracies in the predictions of halo abundance and halo bias, for example, can affect cosmological inferences (Wu et al. 2010), and measurements of the baryon acoustic oscillations (BAO) clustering feature will eventually reach the stage where theoretical estimates of the shift of this feature from non-linear dynamics become important (Seo et al. 2010). Although current state-of-the-art cosmological N-body simulations, given a specific set of cosmological parameters, are in many ways well-equipped to deliver highly precise predictions of the dark matter two-point correlation function and power spectrum for a relatively wide range of scales (Heitmann et al. 2010), the difficult-to-estimate covariances of these statistics are also crucial for placing constraints on cosmological parameters (Habib et al. 2007; Takahashi et al. 2009). To stay ahead of the observational demands, any methodological improvement to the current framework of setting up and running cosmological N-body simulations is therefore welcome, even if only relevant to certain applications and in certain regimes.

In this paper I explore the predictions of a novel method for running ensembles of simulations that, unlike the conventional method, is designed to maintain correspondence between simulated real-space clustering statistics (e.g. $\sigma_8, \xi(r)$) and the real-space properties of the assumed cosmological model. Originally proposed by Pen (1997) and implemented by Sirko (2005)[12], this method allows the DC mode of each simulation (in an ensemble of simulations) to vary according to the clustering power on the scale of the box in much the same way that the density within randomly placed boxes in the real universe will fluctuate around the mean density. Although it is now com-

---

[12] Once publicly available, the code can still be obtained through http://web.archive.org

mon practice, using the conventional method, to set the DC mode in each simulation to zero, in the early days of fully cosmological N-body simulations this was not always done (e.g. Frenk et al. 1988). This issue has also been discussed in the context of artificially changing the DC mode of an existing simulation as a way of scaling a simulation completed with a certain set of cosmological parameters to a slightly different model (Tormen & Bertschinger 1996; Cole 1997; Angulo & White 2010).

In the Sirko (2005) framework the initial power spectrum used with the Zeldovich (1970) (and by extension 2LPT, Bouchet et al. 1995; Scoccimarro 1998) approximation is convolved such that the matter correlation function matches exactly the linear theory correlation function for $r < L_{\rm box}/2$, while for $r > L_{\rm box}/2$ the correlation function is set to zero. With this in mind Sirko refers to this approach as "ξ-sampled" initial conditions (ICs), while the standard method is referred to as "P-sampled", since by using an unconvolved linear theory power spectrum with the Zeldovich approximation the initial conditions are instead matched to the fourier space clustering statistics. The ξ-sampled strategy, by matching the correlation function out to $r = L_{\rm box}/2$, should avoid biases on all real space statistics, since the rms overdensity in spheres, $\sigma(R)$, is simply related to the correlation function, and the halo mass function to good approximation is only a function of $\sigma(R)$. Without this convolution these real space statistics become biased (i.e. from $P(k) = 0$ for $k \lesssim 2\pi/L_{\rm box}$), as discussed by Pen (1997) and Bagla & Prasad (2006).

Although a number of groups have published results using the initial conditions code developed by Sirko, which was the among the first include the 2nd order Lagrangian corrections (Bouchet et al. 1995; Scoccimarro 1998) to the Zeldovich (1970) displacements, the code is very seldom used to generate ξ-sampled ICs. To my knowledge, only Reid et al. (2009) have utilized the code in this mode, citing the success of convergence tests in Reid (2008). In that study they create mock catalogues from a suite of 42 simulations with $L_{\rm box} = 558h^{-1}$ Mpc, and $N = 512^3$ for comparison with SDSS LRG data (Tegmark et al. 2006). They chose the ξ-sampled method for this task, citing the attractive feature of allowing the DC mode of the box to vary, thereby modeling the power spectrum covarariance of real surveys more realistically. Reid (2008) and Appendix A of Reid et al. (2009) present a wide variety of convergence tests that explore the effects of increasing the resolution with either fixed initial conditions (i.e. with a particular randomly sampled value for the DC mode) or for a set of a few initial conditions realizations. Though these tests met with much success, there may, nevertheless, be differences between *ensembles* of ξ-sampled and P-sampled simulations.

This study systematically explores the ensemble-averaged predictions using the two different methods. Where the results disagree it may be ambiguous which approach is more accurate, therefore I focus on pure powerlaw models which should evolve self-similarly. This allows powerful self-consistency checks of the simulation results, since each output should, in a statistical sense, resemble scaled versions of earlier and later outputs. These kinds of "self-similar" tests were decisive in confirming the accuracy of the first generation of fully cosmological N-body codes (Efstathiou et al. 1988). I also show a few tests where, instead of a pure powerlaw, I simulate initial conditions consistent with a configuration space powerlaw times a gaussian bump. Investigated in Chapter 2 in great depth as a simplified model of BAO, this test is self-similar in a different sense – namely that the evolution of the dark matter clustering should only depend on the ratio of the scale of non-linearity to the scale of the BAO.

I test these models extensively, focusing on pure powerlaw models with spectral slopes of $n = -1$, -1.5, and -2, and on the three models explored in Chapter 2 which resemble $n = -0.5$, -1, and -1.5 powerlaws in fourier space. I compare predictions from the two methods, showing results for the matter correlation function in § 3.3, the power spectrum in § 3.4, and statistics of the halo population in § 3.5. In § 3.7 I discuss my results and in § 3.8 I summarize my main conclusions.

3.2 Initial Conditions

3.2.1 Overview of the ξ-sampled Method

In the ξ-sampled method implemented by Sirko (2005), the (real space) matter correlation function for a given cosmological model is the fourier transform of the power spectrum

$$\xi(r) = \int \frac{d^3k}{(2\pi)^3} P(k)\, e^{i\vec{k}\cdot\vec{r}} = \int_0^\infty P(k)\, \frac{\sin kr}{kr}\, k^2\, dk. \tag{3.1}$$

To convolve $P(k)$ such that the simulated $\xi(r)$ is an exact match to Eq. 3.1 for $r < L_{\rm box}/2$, but is zero for larger separations, one simply fourier transforms $\xi(r)$ while cutting off the integral at $L_{\rm box}/2$ since $\xi(r) = 0$ for $r > L_{\rm box}/2$,

$$P_{\rm real}(k) = 4\pi \int_0^{L_{\rm box}/2} \xi(r)\, \frac{\sin kr}{kr}\, r^2\, dr. \tag{3.2}$$

I will refer to this result as $P_{\rm real}(k)$ to emphasize that this power spectrum is designed to maintain correspondence with the real space properties of the cosmological density field. Importantly, $P_{\rm real}(0)$ is non-zero even if $P(0) = 0$; this term sets the fluctuations in the DC mode. In Appendix A of Sirko (2005), using the subscript "uni" to denote variables in the model of interest and "box" to identify the parameters of the simulated volume, these fluctuations are mapped self-consistently onto fluctuations in cosmological parameters,

$$H_{0,\rm box} = H_{0,\rm uni}\frac{1}{1+\phi}, \tag{3.3}$$

$$\Omega_{m,\rm box} = \Omega_{m,\rm uni}(1+\phi)^2, \tag{3.4}$$

$$\Omega_{\Lambda,\rm box} = \Omega_{\Lambda,\rm uni}(1+\phi)^2, \tag{3.5}$$

$$\phi = \frac{5}{6}\frac{\Omega_m}{D(1)}\Delta_0, \tag{3.6}$$

where Δ_0 is a gaussian variable with mean zero and variance $P_{\rm real}(0)/L_{\rm box}^3$ and $D(1)$ is the value of the linear growth function at the present epoch. Note that Eq. 3.3 implies that in h^{-1} length units the box size of each simulation varies with the value of ϕ, whereas in standard length units (e.g. Mpc) the box size remains fixed. Similarly the box integrated mass, $M_{\rm box} = \rho_m L_{\rm box}^3$, varies from box-to-box in $h^{-1}M_\odot$ units, but is fixed in $M_\odot$ units.

Of crucial importance in deriving Eqs. 3.3-3.6 is the relationship between the scale factor of interest, $a_{\rm uni}$, and the corresponding scale factor in a particular realization, $a_{\rm box}$. In Sirko (2005) this relationship is set by an approximate formula which determines $a_{\rm box}$ as the epoch where the age of the universe in the box is the same as the age of the unperturbed universe during the epoch of interest,[13]

$$a_{\rm box} \approx a_{\rm uni}\left(1 - \frac{1}{3}\frac{D(a)}{D(1)}\Delta_0\right). \tag{3.7}$$

Sirko (2005) justified this formula by arguing that the ratio of the average density of the universe to the average density of a given box, $\bar{\rho}_{\rm uni}/\bar{\rho}_{\rm box} = a_{\rm box}^3/a_{\rm uni}^3$, is simply related to the overdensity of the box, which grows according to the linear theory growth function. Eq. 3.7 can also be obtained by Taylor expanding the perturbed $H(a_{\rm box})$ for small ϕ and equating the age of the universe in the box to the age of the universe at the epoch of interest.

3.2.2 Integration of Particle Trajectories

Having set up the initial conditions, determined the perturbed cosmological parameters of a given realization and computed the relevant scale factors, $a_{\rm box}$, for the epochs of interest, the initial conditions can be evolved using any cosmological N-body code. I use the publicly-available Gadget2 code with no modifications (Springel 2005). As a hybrid Tree-based code with PM grid for large scale forces, Gadget2 is a highly scalable N-body code which compares well to other codes used in the literature (e.g. Heitmann et al. 2010). Unless otherwise noted I show results from simulations with 256^3 particles and a 512^3 PM grid. Initial redshifts were set using $\Delta^2(k_{\rm Ny}) \lesssim 0.001$ as a rule of thumb (Lukić et al. 2007), and the force softening was set to 1/20th the initial mean interparticle spacing.

3.2.3 Statistics of the Cosmological Density Field

With ensembles of simulations in the conventional method, the measurements of dark matter clustering at a given output, $a_{\rm uni}$, can typically be combined, and the statistical precision improved, with a simple average. In ξ-sampled simulations this procedure involves the extra step of weighting the measurements in each realization by factors of $a_{\rm box}^3$. Measuring $\xi(r)$ (in any context) is equivalent to calculating Gabrielli et al. (2005)

$$\xi(r) = \frac{\Gamma(r)}{\bar{n}} - 1 \tag{3.8}$$

---

[13] Cole (1997) was the first to appreciate that $a_{\rm box} \neq a_{\rm uni}$ but instead proposed to set $a_{\rm box}$ by matching the amplitude of the linear growth function in the perturbed cosmology. I return to this issue in 3.7

where $\bar{n}$ is the average number density of particles in the volume and $\Gamma(r)$ is the number density of particles separated by length r. For an output from given realization using ξ-sampled ICs I am interested in $\xi_{\rm uni}(r) = \Gamma(r)/\bar{n}_{\rm uni} - 1$, and since $\bar{n}_{\rm uni} = \bar{n}_{\rm box}(a_{\rm box}/a_{\rm uni})^3$ this scaling is simply

$$\xi_{\rm uni}(r) = \left(\frac{a_{\rm uni}}{a_{\rm box}}\right)^3 \frac{\Gamma_{\rm box}(r)}{\bar{n}_{\rm box}} - 1 = \left(\frac{a_{\rm uni}}{a_{\rm box}}\right)^3 (\xi_{\rm box}(r) + 1) - 1 \qquad (3.9)$$

Note that in Eq. 3.9 I have omitted an extra factor of $-2(a_{\rm uni}/a_{\rm box})^3$ that appears in Sirko (2005). I am unable to reproduce the results in Sirko (2005) including this term, which could arise from using optimal estimators like Landy & Szalay (1993) or Davis & Peebles (1977). I use the "natural" estimator, $\xi(r) = \Sigma_i DD_i/RR_i - 1$, without any kind of cross correlation between data and random pairs. Sirko (2005) does not state which estimator is used.

The box-to-uni correction factor for the power spectrum is determined straightforwardly from the fourier transform of Eq. 3.9,

$$P_{\rm uni}(k) = \left(\frac{a_{\rm uni}}{a_{\rm box}}\right)^3 \langle \delta(\vec{k})\delta^*(\vec{k})\rangle \ . \qquad (3.10)$$

If computed using h Mpc^{-1} units in k-space, the measurement of the bracketed term in Eq. 3.10, and the book keeping required to count of the number of modes contributing to each k for error estimation can be a fairly complicated exercise since the size of the simulation box varies in h^{-1} length units. In practice, it is much simpler (bearing in mind that box size is fixed in Mpc units) to convert the particle positions to Mpc units before applying the standard methods of mapping the particles onto a gridded density field (Hockney & Eastwood 1981, I use CIC) and computing its fourier transform. Similarly, measuring the halo mass function is considerably simplified by converting the particle positions to Mpc units and the particle masses to $M_\odot$ units (from $h^{-1}M_\odot$ units) before using standard halo finding methods. I use the FOF halo finder (Einasto et al. 1984; Davis et al. 1985) with a linking length of 0.2 times the mean interparticle spacing.

3.2.4 The Integral Constraint on $\xi(r)$ in P-sampled Simulations

An important but sometimes neglected subtlety in measuring the correlation function in standard, P-sampled simulations is the artificial imposition of an integral constraint on the *measured* $\xi(r)$ on the scale of the simulation volume. This effect is entirely orthogonal to the question of which estimator (Davis & Peebles 1977; Landy & Szalay 1993, etc.) converges most rapidly to the true $\xi(r)$ in the presence of Poisson noise. The problem stems from using a finite volume with a fixed number density of particles $\bar{n}$ to estimate $\xi(r)$. Since, in a simulation box, the integral of $\Gamma(r)$ over the volume yields the number density of particles,

$$\int_{V_{\rm box}} r^2\Gamma(r)dr = \bar{n}, \qquad (3.11)$$

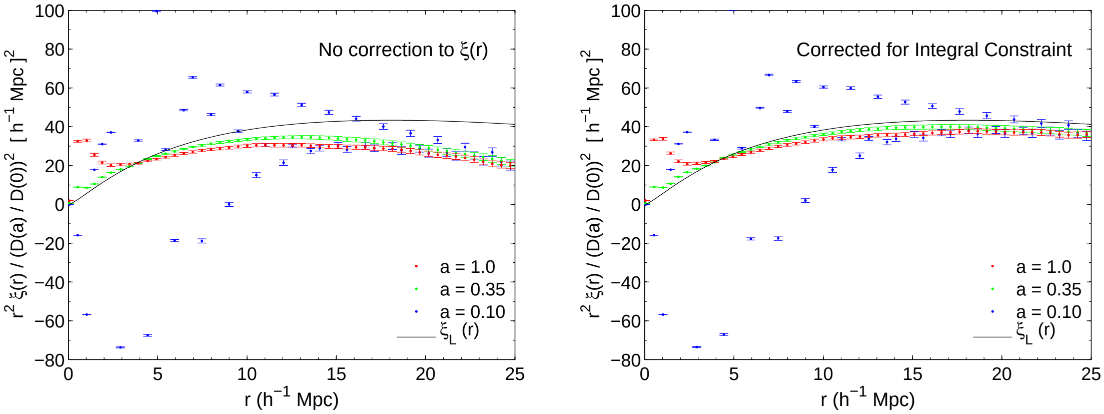

Figure 3.1: Matter correlation function results from a ΛCDM ensemble of simulations ($L_{\rm box} = 100h^{-1}$ Mpc, $N = 64^3$, 100 realizations) using standard (P-sampled) ICs. The left panel shows the $\xi(r)$ results from this simulation set without applying the integral constraint correction described in the text. The right panel shows the results from including the corrections in Eq. 3.13. Error bars show the error on the mean. Note that the earliest output ($a = 0.1$, shown in blue) is severely affected by transients from the initial conditions.

with $\xi(r)$ in its original form in Eq. 3.8, this implies

$$\int_{V_{\rm box}} r^2 \xi_{\rm meas}(r) dr = 0 \tag{3.12}$$

regardless of whether this is the case with the true $\xi(r)$. In finite volumes in the real universe $\bar{n}$ will vary from box-to-box and, importantly, the average of $\bar{n}^{-1}$ (which appears in Eq. 3.8) will deviate from the inverse of the true (i.e. asymptotically large volume) number density. In surveys a similar problem is encountered from uncertainties and biases in the average number density of objects – in both cases the problem lies with the $\bar{n}$ term in Eq. 3.8 rather than the $\Gamma(r)$ term.

For ΛCDM simulations using large boxes ($L_{\rm box} \gg 1$Gpc) the integral constraint is a minor issue, but for simulations with smaller boxes this is an important concern. Notably, Sirko (2005) presented simulations with $L_{\rm box} = 50 - 100h^{-1}$ Mpc without any kind of corrections for this effect. Consistent with the more sophisticated treatments of Bernardeau et al. (2002) and Landy & Szalay (1993), I argue in Appendix B that the correction should take the form

$$\xi(r) = \quad \xi_{\rm meas}(r) + \bar{\xi}_L(R_{\rm S}) \tag{3.13}$$

where $\xi_{\rm meas}(r)$ is as in Eq. 3.8 and $\bar{\xi}_L(R_{\rm S}) = 3/R_{\rm S}^3 \int_0^{R_{\rm S}} r^2 \xi_L(r) dr$ where $\xi_L(r)$ is the linear theory correlation function and $R_{\rm S} \approx L_{\rm box}/1.61$.

Fig. 3.1 shows the importance of this correction with a set of P-sampled results from ΛCDM simulations ($\Omega_m = 0.27, \Omega_\Lambda = 0.73, h = 0.71$, $\sigma_8 = 0.84$) that closely mimics the fiducial simulation

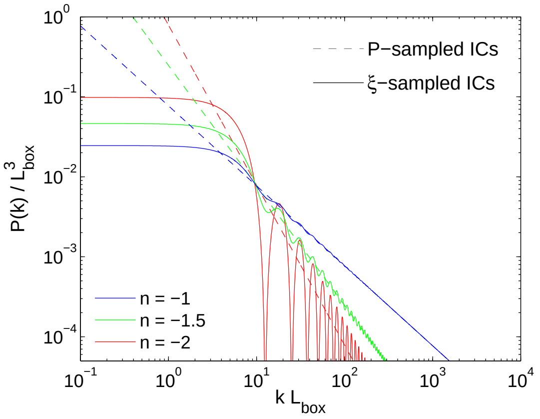

Figure 3.2: A comparison of P-sampled and ξ-sampled pure powerlaw models. ξ-sampled power spectra are computed from Eq. 3.2 and used to generate initial conditions for that method. $r_0/L_{\rm box} = 1/16$ is chosen to set the overall amplitude of each model.

set in Sirko (2005) ($N = 64^3$ particles, $L_{\rm box} = 100h^{-1}$ Mpc, 100 realizations with $z_i = 39$). Fig. 3.1 can be directly compared to Fig. 9 of Sirko (2005). Although the first output is severely affected by transients from the initial conditions I include it for comparison with Sirko (2005).

The integral-constraint correction increases the correlation function at 1/4th scale of the box scale by almost a factor of two, considerably improving the agreement with linear theory. Without including this correction it is tempting to conclude that the standard P-sampled method dramatically fails in modeling the correlation function unless box sizes much larger than the scales of interest are used. I apply this correction to all of the P-sampled results shown in this paper. ξ-sampled results do not require this correction, and Eq. 3.9 naturally takes this effect into account. In fact, the correction to $\xi(r)$ in Eq. 3.13 bears a close resemblance to the form of 3.9, as I will discuss in the next section using pure powerlaw initial conditions.

3.2.5 ξ-sampled ICs with Powerlaw Models

For powerlaw models, where $P(k) = Aa^2k^n$, the task of computing Eq. 3.2 is made substantially easier because an exact analytic solution for $\xi(r)$ is known in this case,

$$\xi(r) = \left(\frac{r_0}{r}\right)^{n+3}, \, A\,a^2 = \frac{2\pi^2\, r_0^{n+3}\,(2+n)}{\Gamma(3+n)\sin((2+n)\pi/2)}\ , \tag{3.14}$$

(Peebles 1980). Eq. 3.2 therefore becomes

$$P_{\rm real}(k) = 4\pi r_0^{n+3}\int_0^{L_{\rm box}/2} r^{-(n+1)}\,\frac{\sin kr}{kr}\,dr \tag{3.15}$$

and the DC power can be straightforwardly expressed as

$$P_{\rm real}(0) = 4\pi r_0^{n+3} \int_0^{L_{\rm box}/2} r^{-(n+1)}\, dr \tag{3.16}$$

$$= \frac{2^{n+2}\pi}{-n} \left(\frac{r_0}{L_{\rm box}}\right)^{n+3} L_{\rm box}^3. \tag{3.17}$$

Analytic and special-function solutions to Eq. 3.15 exist for certain powerlaws. In this study I am interested in $n = -1$, -1.5 and -2 which can be expressed by

$$P_{\rm real,n=-1}(k) = 4\pi r_0^2\, {\rm Si}({\rm kL_{box}}/2)\, {\rm k}^{-1}, \tag{3.18}$$

$$P_{\rm real,n=-1.5}(k) = 2^{5/2}\pi^{3/2} r_0^{3/2}\, {\rm S}(\sqrt{\rm kL_{box}}/\sqrt{\pi}){\rm k}^{-1.5}, \tag{3.19}$$

$$P_{\rm real,n=-2}(k) = 8\pi r_0\, \sin^2(kL_{\rm box}/4)\, k^{-2}, \tag{3.20}$$

where Si(x) is the sine integral and S(x) is a Fresnel integral. These formulae can be very useful for generating accurate initial conditions, especially for steep power spectra. I show these power spectra in Fig. 3.2, fixing $r_0/L_{\rm box} = 1/16$ to set the relative amplitudes. Notice that steeper powerlaws have larger DC power, easily seen on the plot as the asymptotic value of $P_{\rm real}(k)/L_{\rm box}^3$ for small k. Noticing that $P(k)$ does not go to zero at small k for the P-sampled powerlaws, one might be concerned that these models are unphysical. However, despite the high levels of large scale clustering power the rms overdensity in spheres and other statistics remain finite for $n > -3$.

3.2.6 Scale free?

Although pure powerlaw models are often referred to in the literature as "scale free," since $P(k) = Ak^n$ is featureless, the ξ-sampled initial power spectra shown in Fig. 3.2 clearly depend on the choice of $L_{\rm box}$. In practice, these oscillatory features die away in simulations and the effect of $L_{\rm box}$ is merely to change the variance of the DC mode (which is set by $P_{\rm real}(0)/L_{\rm box}^3$).

Since dark energy does introduce a new scale into the problem (e.g. the age of the universe when $\rho_m = \rho_\Lambda$), I consider only $\Omega_{m,\rm uni} = 1.0, \Omega_{\Lambda,\rm uni} = 0, \Omega_{k,\rm uni} = 0$ so as to keep the simulations as "scale free" as possible and allow the self-similar tests discussed in the next section. In the Zeldovich (1970) and adhesion (Gurbatov et al. 1989; Weinberg & Gunn 1990) approximations (as in linear theory), the effect of dark energy on structure formation is entirely captured by changing the linear theory growth function. Nusser & Colberg (1998) and Zheng et al. (2002) convincingly argue that this approximation is remarkably accurate even in the non-linear regime – the second order effect of dark energy is relatively small (see also Chapter 2). Therefore the results of my $\Omega_m = 1$ tests should still be quite relevant to studies that include a dark energy component.

As one final comment on the scale-free nature of my simulations, throughout I adopt, as a time variable,

$$\frac{a}{a_*} = \left(\frac{k_{\rm box}}{k_{\rm NL}}\right)^{(n+3)/2}, \tag{3.21}$$

where $k_{\rm box} = 2\pi/L_{\rm box}$ and $k_{\rm NL}$ is defined by the dimensionless linear theory power spectrum, $\Delta^2(k_{\rm NL}) \equiv 1$. This choice is simply related to the $\sigma_{\rm miss}$ formula of Smith et al. (2003), which quantifies the missing power on the scale of the box in P-sampled simulations. I adopt Eq. 3.21 for ease of comparison with Widrow et al. (2009) and because the $\sigma_{\rm miss}$ formula in Smith et al. (2003) would be inappropriately applied to ξ-sampled simulations, which have a turnoff in $P_L(k)$ near the box scale (Fig. 3.2).

3.3 $\xi(r)$ results

3.3.1 Powerlaw Models

Fig. 3.3 shows my primary results for the self-similar scaling of the matter correlation function. The x-axis is shown in r/r_0 units where $\xi_L(r_0) = 1$. Insofar as the dark matter clustering is negligibly affected by numerical limitations such as the finite scale of the box or the scale of the force softening, with this scaling the correlation function results from different outputs should all lie upon the same line. To the extent that this is achieved the correlation function can be said to evolve with self-similarity and it is clear from Fig. 3.3 that over a wide range of scales the results from these relatively modest, $N = 256^3$, simulations do fall upon the the same locus as expected. This locus is different for each powerlaw; for steeper power spectra (e.g. $n = -2$) power is transferred from large scales to small scales and the non-linear growth of $\xi(r)$ outpaces linear theory whereas for shallower power spectra (e.g. $n \gtrsim -1$) there is so much small scale power that the process of halo formation and collapse causes the non-linear growth to fall behind linear theory in a process sometimes called "pre-virialization" (Davis & Peebles 1977). In the language of the halo model (Cooray & Sheth 2002) this implies that the predicted linear theory clustering on small scales is so high that the amplitude of the 1-halo term is below the linear theory clustering amplitude on those scales. The $n = -1$ case falls between these two extremes and the amplitude of the correlation function is both above and below linear theory, depending on the regime. (For a bracketing case of an even shallower power spectrum see, e.g., the $n = -0.5$ results in Appendix A.)

In Fig. 3.3, the ξ-sampled and P-sampled methods generally agree on the shape of the self-similar solution. This is significant for the ξ-sampled results, on some level verifying the method. Alongside the measurements in each case the results from higher resolution simulations are shown. For $n = -1$ and $n = -2$ this comparison is made by numerically fourier transforming the non-linear power spectrum fitting functions published in Widrow et al. (2009); note in the $n = -1$ case I include subtle but important corrections to their fit at small $k/k_{\rm nl}$ as determined in Appendix A. For $n = -1.5$ I compare with $\xi(r)$ measurements from 10 P-sampled simulations with $N = 512^3$ (Appendix A). These high-resolution results are used more quantitatively in Fig. 3.4.

Important to point out in Fig. 3.3 is that the error on the mean $\xi(r)$ for the ξ-sampled method is much larger than the P-sampled simulations, despite running 2.5× as many ξ-sampled simulations in the $n = -1$ and $n = -2$ cases to improve the statistics, and 7.5× as many simulations in the

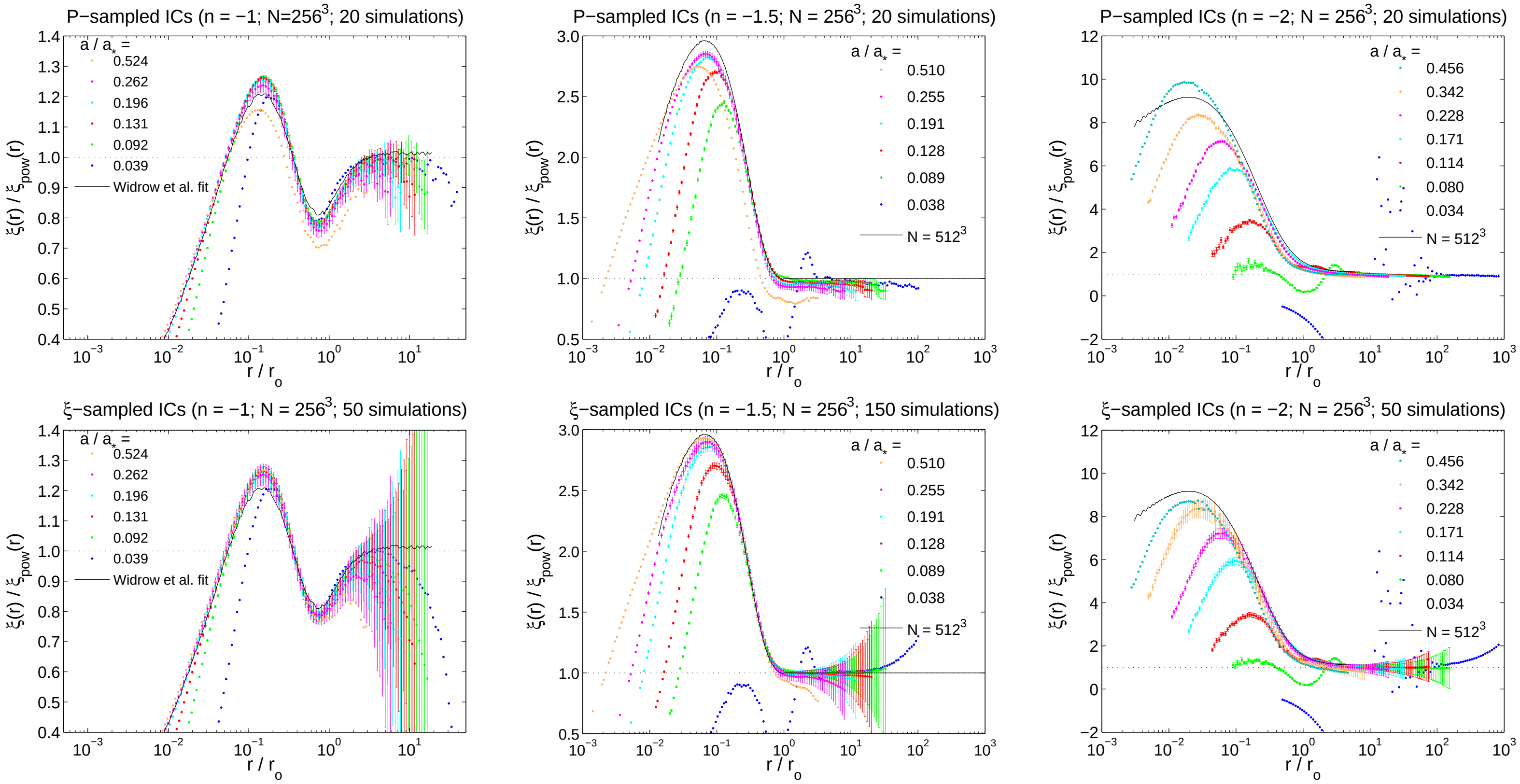

Figure 3.3: Measured matter autocorrelation functions from conventional P-sampled (upper panels) and ξ-sampled (lower panels) ensembles of simulations. The left-most panels show results from an initially $n = -1$ power spectrum, middle panels show results from $n = -1.5$, and the right hand panels show $n = -2$. In each plot the x-axis is scaled by the non-linear scale, r_0, where $\xi_L(r_0) \equiv 1$ so that, if evolving with the expected self-similar behavior, the outputs should lie upon the same locus of points. The y-axis is scaled by $\xi_L(r) = (r_0/r)^{n+3}$. Black lines show high resolution results from P-sampled simulations for comparison (see text). Error bars show measured error on the mean.

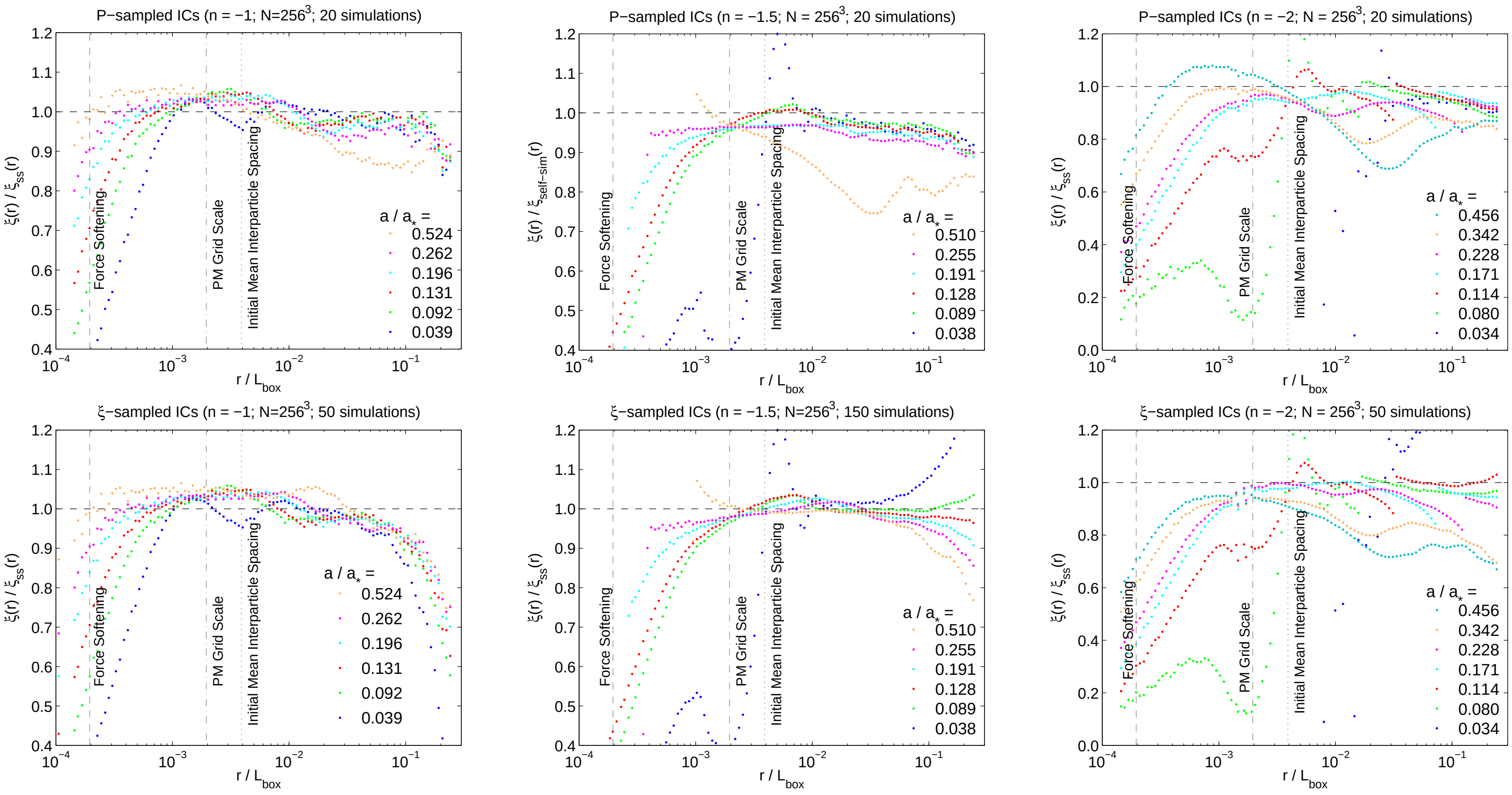

Figure 3.4: Measured correlation functions from simulations relative to high-resolution results for the self-similar scaling ($\xi_{ss}(r)$; black lines in Fig. 3.3). Points show the mean $\xi(r)$. Panels are organized as in Fig. 3.3 (top panels: P-sampled results, bottom panels: ξ-sampled results, $n = -1, -1.5$ and -2 from left to right). Vertical lines show relevant *numerical* scales: the initial mean interparticle spacing (dotted black), the Particle-Mesh Grid (dot-dashed black), and the force softening (dashed black).

$n = -1.5$ case to further ensure that the mean of the distribution of DC modes in the simulation set was very close to zero. For the ξ-sampled $n = -1$ case there are not enough realizations (50) to ensure that the mean of the distribution of DC modes agree with zero at the necessary level of accuracy (a criterion which will be discussed in § 3.6), and as a result, although difficult to see from the large error bars on the mean, there are strong deviations between the measurements of the mean $\xi(r)$ and the self-similar fit at large r for each output. The effect is more clearly illustrated in Fig. 3.4, which shows the agreement between the $\xi(r)$ measurements from my simulation set and the high-resolution self-similar solutions more quantitatively. Near $r/L_{\rm box} \sim 10^{-1}$ and independent of output, the ξ-sampled $n = -1$ results systematically fall well below the self-similar solution.

With this well-understood caveat, the agreement with the high-resolution self-similar results is fairly good and excluding the final outputs in each case my simulation set tends to match the self-similar evolution to better than about 5% in most outputs and on most scales. The last output is excluded from this conclusion since the linear theory clustering level is so high that one expects departures from the true non-linear clustering from the suppression of power on the scale of the box. Also, the correction for the integral constraint, which assumes a *linear theory* correlation function in $\bar{\xi}(R_{\rm box})$, likely becomes inaccurate in this regime as well.

On scales much smaller than the box size, Fig. 3.4 shows that as structure evolves in the simulations the self-similar behavior extends below the scale of the initial mean inter-particle spacing, in some cases approaching the force softening. Since at best the initial conditions of the simulations only match the self-similar correlation function down to the initial mean interparticle spacing this result is non-trivial and difficult to anticipate from first principles. Little et al. (1991), using $n = -1$ simulations, show that Fourier modes in the non-linear regime are largely determined by the collapse of large-scale modes rather than by evolution of power initially on those scales. However, Joyce et al. (2009) and collaborators have argued that the common practice of setting the force softening significantly smaller than the initial mean interparticle spacing introduces errors which arise from the possibility that with this choice the equations of motion for the particles are no longer true to the Vlasov-Poisson fluid equations. My results argue against this, although my ~5% correspondence with the self-similar correlation function from high resolution simulations may still be within the anticipated errors on $P(k)$ discussed in Joyce et al. (2009). At any rate I point out that powerlaw models may be a valuable tool for checking the accuracy of simulations in this regime, as previously argued by Efstathiou et al. (1988). For example, self-similar scaling could be used to determine when force softening becomes too aggressive – a matter of considerable import for studies of halo substructure or larger-box cosmological simulations with a wide dynamic range. The small scale results in Fig. 3.4 imply that the force softening used here (1/20th of the initial mean interparticle spacing) does substantially and accurately extend the dynamic range of my simulations. Importantly, this appears to be true for different powerlaws; it does not significantly depend on whether power is being rapidly "transferred" to smaller scales as for $n = -1.5$ and $n = -2$ or whether the non-linear growth proceeds less quickly than the linear theory prediction on small scales (i.e. $r < r_0$), as for $n = -1$.

3.3.2 Powerlaw Times a Bump Results

As discussed in Chapter 2, a real-space powerlaw times a bump can be used as a self-similar numerical test in addition to providing insight into the non-linear physics of the evolution of the BAO feature. In this case,

$$\xi_{\rm IC}(r) = \left(\frac{r_0}{r}\right)^{n+3} (1 + A_{\rm bump}\, e^{-(r-r_{\rm bao})^2/2\sigma_{\rm bao}^2}), \tag{3.22}$$

and for resemblance to the ΛCDM correlation function I chose $A_{\rm bump} = 2.75$, $\sigma_{\rm bao}/r_{\rm bao} = 0.075$, and powerlaws of $n = -0.5$, -1, and -1.5. Unlike ΛCDM, this setup can be evolved much further than $\sigma_8 \sim 1$ to investigate the non-linear physics of the problem. I compare results in Fig. 3.5 from ξ-sampled ensembles of simulations with $N = 256^3$, $r_{\rm bao}/L_{\rm box} = 1/20$ to gaussian fits to the results of the P-sampled, $N = 512^3$, $r_{\rm bao}/L_{\rm bao} = 1/20$ sets of simulations in Chapter 2. At least qualitatively the two simulation sets agree well. The slight small-scale discrepancy with the gaussian fit in the last output shown for the $n = -1$ case is a problem with the fit itself, as apparent in the P-sampled $n = -1$ results shown in Fig 2.3 while the discrepancies with the fit on scales larger than the bump stem from the mean of the fifty, randomly-sampled DC modes being slightly above zero, much like the pure powerlaw case for $n = -1$, a problem easily fixed by running more realizations. The slight mismatch in the amplitude of the bump in the $n = -1.5$ case is mirrored in the P-sampled, $N = 256^3$, $r_{\rm bao}/L_{\rm box} = 1/20$ results in Fig. 2.8, and the discrepancy, at large $r/r_{\rm bao}$, for the $n = -0.5$ case is in a regime where the amplitude of the correlation function is very weak and difficult to measure. Overall, the evolution of the bump is remarkably similar to previous results and, importantly, the non-linear shift of the bump in the $n = -1.5$ case and lack of a shift in the $n = -0.5$ and -1 cases agree with P-sampled simulations. Insofar as these two methods are equally valid approaches to setting up and running cosmological N-body simulations, this conclusion should be reassuring to the wider effort to characterize the non-linear shift of the BAO peak using standard, P-sampled simulations.

As with the powerlaw results in the previous section, despite running a few times more simulations than the P-sampled ensembles, the measured error on the mean $\xi(r)$ is still quite large. (In Chapter 2, I typically ran only seven realizations in each case.) This seems to be the case for a variety of powerlaws and in simulations with and without a bump. A close inspection of the original $\xi(r)$ results in Sirko (2005) likewise show in ΛCDM simulations that the error on the mean $\xi(r)$ is significantly larger in ξ-sampled simulations. Sirko (2005) does not not comment on this interesting result. I return to this issue in §.

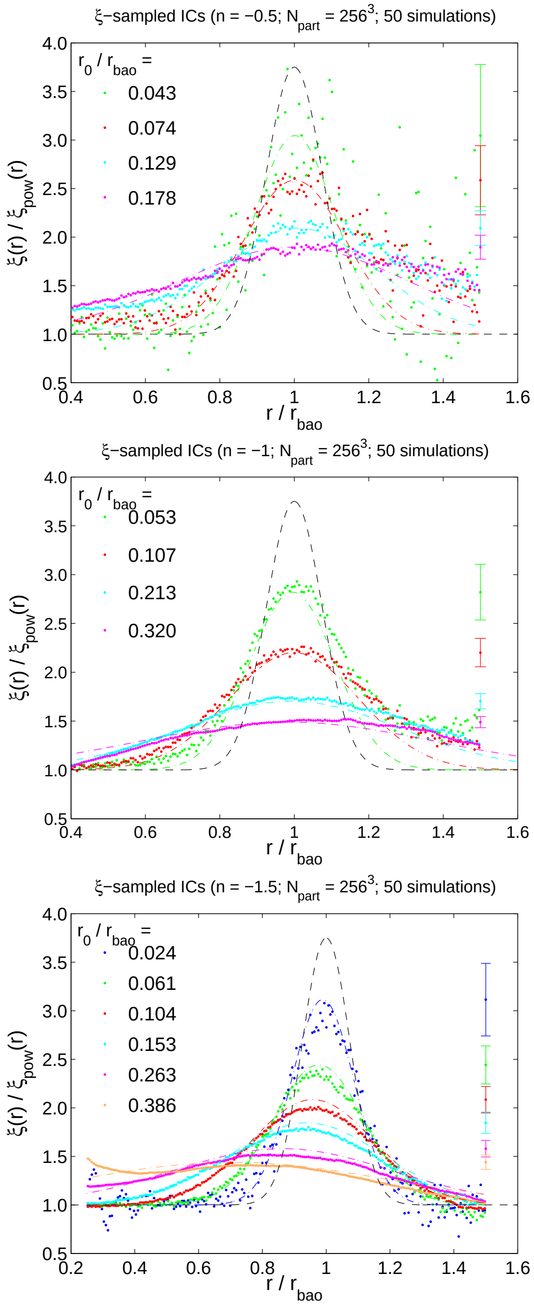

Figure 3.5: Correlation function results from ensembles of 50 ξ-sampled simulations using initial conditions consistent with a powerlaw times a gaussian bump as a simplified model of baryon acoustic oscillations. Dot-dashed lines show gaussian fits to the high-resolution simulations presented in Fig. 2.3. Typical errors on the mean are shown offset to the right.

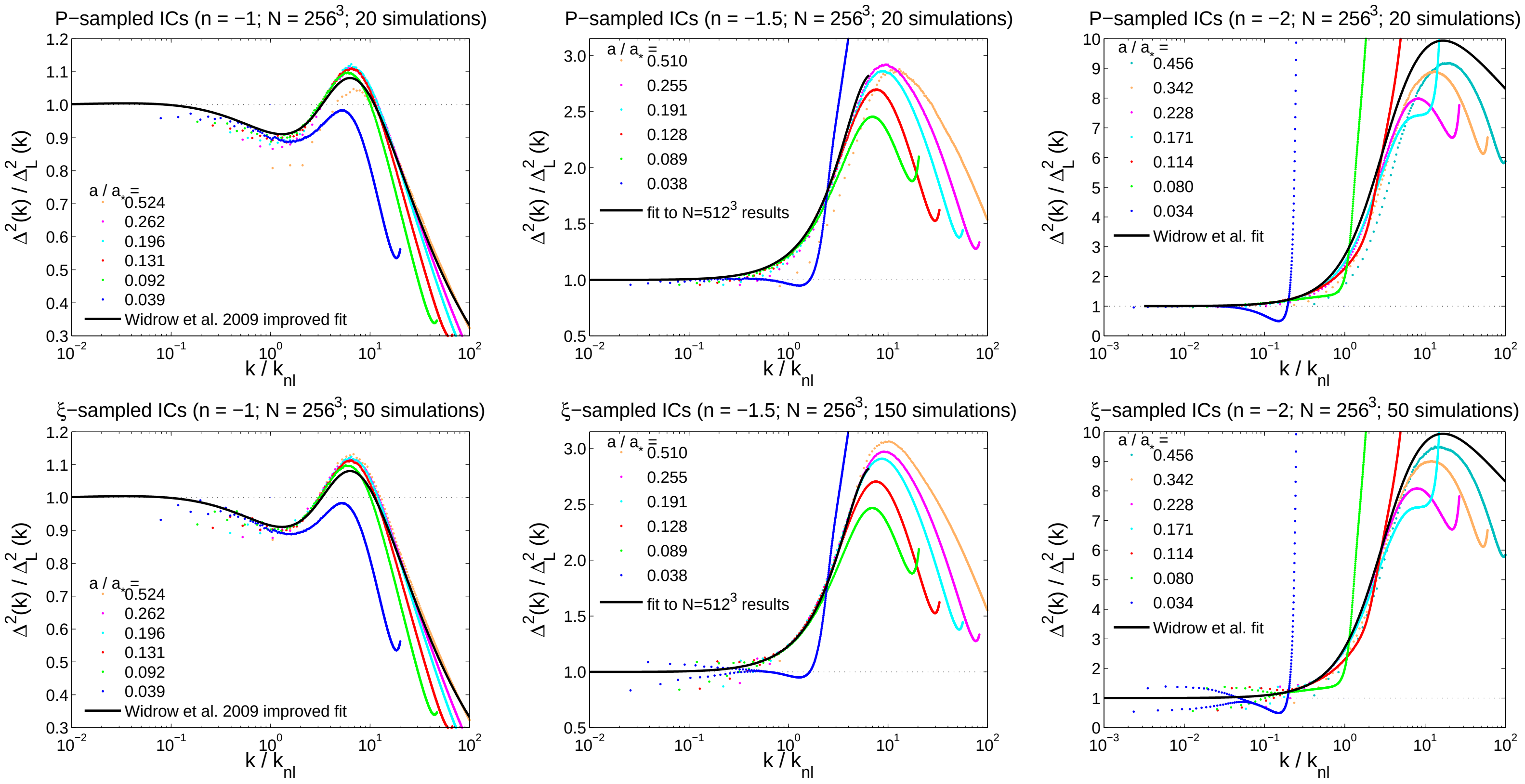

Figure 3.6: Comparison of non-linear power spectrum results from ξ-sampled (top panels) and P-sampled (lower panels) ensembles of simulations for initially $n = -1$ (left), $n = -1.5$ (middle) and $n = -2$ (right) powerlaws. The x-axis is scaled by the non-linear wavenumber $k_{\rm nl}$, defined by $\Delta^2(k_{\rm nl}) \equiv 1$. Solid black lines show results from high-resolution simulations (see text).

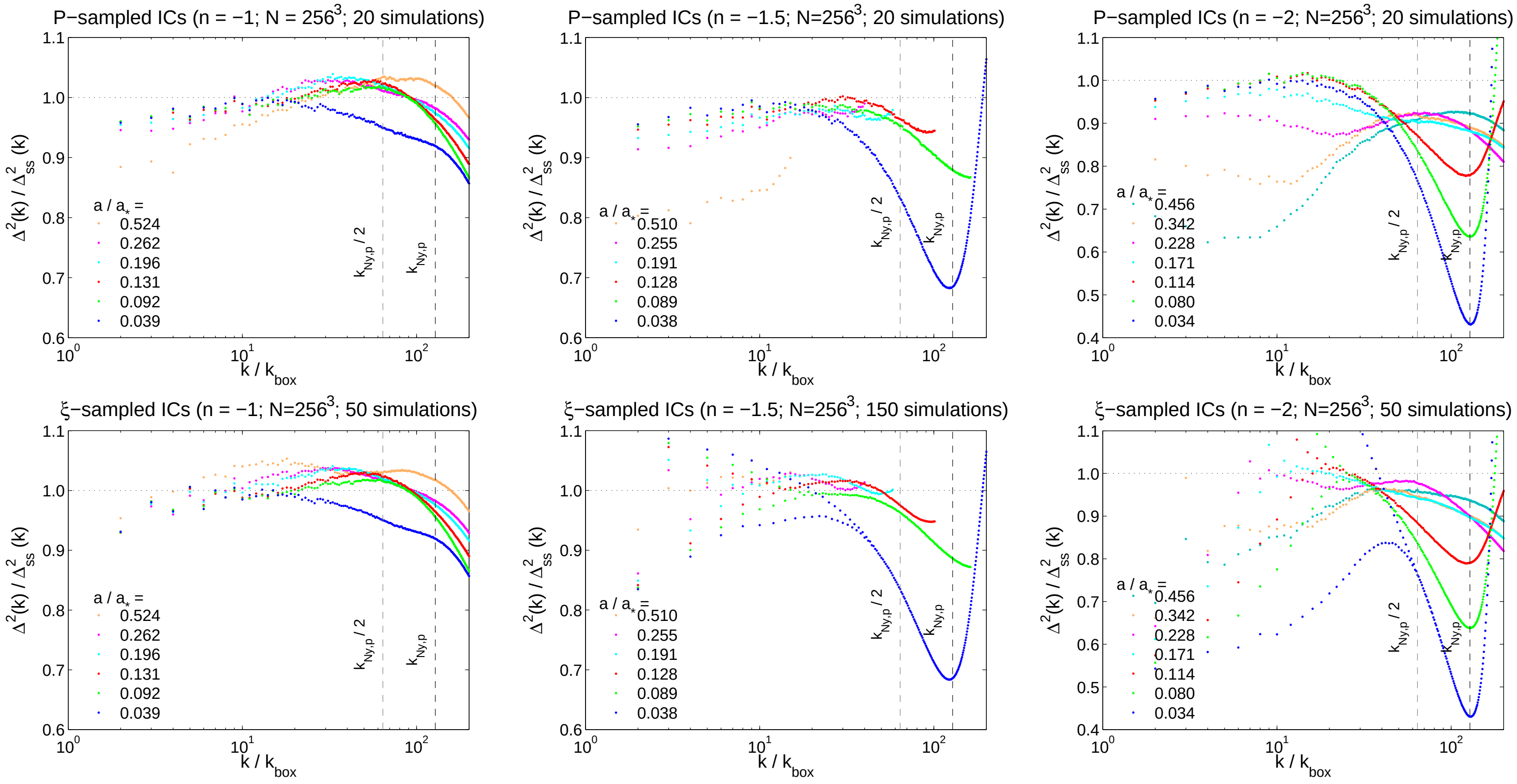

Figure 3.7: Non-linear power spectrum results relative to fitting functions to results from high-resolution simulations ($\Delta^2_{ss}(k)$; black lines in Fig. 3.6). Panels are organized as in Fig. 3.6. The x-axis is shown relative to $k_{\rm box} = 2\pi/L_{\rm box}$ and dashed vertical lines show the particle nyquist wavenumber and half the particle nyquist wavenumber. The $n = -1.5$ results extend to smaller k because non-linear fitting functions from very high-resolution ($N \gg 512^3$) simulations are unavailable in this case.

3.4 P(k) results

Although ξ-sampled simulations are designed to match the real-space properties of the cosmological density field, it is nevertheless interesting to measure the power spectra in these simulations as another self-similar numerical test. These results are presented in Fig. 3.6. As seen in the ΛCDM simulations in Sirko (2005), the oscillations in the initial ξ-sampled power spectrum largely die away. These features are essentially absent in the $n = -1$ case while in the $n = -1.5$ and $n = -2$ cases the oscillations about linear theory for $k/k_{\rm NL} \ll 1$ seem to persist for longer. This is likely explained by the fact that there are more factors of expansion between the epoch of the initial conditions and an output at a given a/a_* in the $n = -1$ case than the $n = -1.5$ or $n = -2$ cases. (As a result, the $n = -1$ case requires much longer execution times to reach $a/a_* \sim 0.5$ than $n = -1.5$ or $n = -2$.)

I compare the power spectrum results in Fig. 3.6 to fitting functions from higher resolution simulations. For $n = -1$ I compare with an improved version (Appendix A) of the fitting function from the high-resolution simulations by Widrow et al. (2009). The $n = -2$ fitting function comes directly from Widrow et al. (2009) and the $n = -1.5$ fitting function (which was not investigated in Widrow et al. 2009) comes from 10 P-sampled, $N = 512^3$ simulations presented in Appendix A. Generally, the agreement with the higher resolution non-linear fits is quite good and, intriguingly, the final outputs of the ξ-sampled results in each case seem to agree more closely with the non-linear fitting function than the P-sampled case. One might expect the ξ-sampled simulations to more accurately handle situations with large amounts of clustering power on the scale of the box, since the fluctuating DC mode is more true to the large scale clustering in the real universe. With the correlation function, it is difficult to see which scheme performs better in this regime, since a discrepancy between the P-sampled correlation function results from different outputs – a violation of self-similarity – or with some higher-resolution result can potentially be explained as a failure of the integral constraint correction, which assumes a linear theory model for $\xi(r)$ in $\bar{\xi}(R_{\rm box})$.

The self-similarity of the power spectrum exhibited in ξ-sampled simulations when the clustering levels become very high on the scale of the box appears to be one of the principal improvements offered by this approach in the tests shown here. Ironically, a method designed to match the real-space properties of the density field appears to more accurately render the fourier-space statistics in this regime. It is tempting to speculate that the difficulties, historically, with realizing self-similar evolution in $n = -2$ simulations with small numbers of particles could have been alleviated by this method (Efstathiou et al. 1988; Bertschinger & Gelb 1991). However, note that the errors on the mean in Fig. 3.6 are considerably larger in ξ-sampled simulations with even 2.5× the number of realizations than in P-sampled simulations. This penalty is severe – at least doubling the computational expense to obtain the same errors on the mean power spectrum and correlation function. I return to this issue in § 3.6, discussing whether "paying" this penalty is more advantageous than increasing the numbers of particles in the box in simulating the non-linear evolution of very steep

($n \lesssim -2$) power spectra as would be relevant to studying the evolution of the very large k power spectrum in ΛCDM (Elahi et al. 2009).

As a more quantitative comparison in Fig. 3.7 I show the ratios of the non-linear power spectrum results to the high-resolution self-similar fits. Bearing in mind, again, that the initial power spectrum has oscillatory features from the cutoff in Eq. 3.2, the ξ-sampled simulations typically match the self-similar solution on scales close to the box better than the P-sampled simulations. Conclusions regarding the self-similar scaling beyond the scale of the initial mean interparticle spacing are hindered by the aliasing of the 1024^3 grid used to measure the power spectrum. Since the scale of the resolution elements of this grid is only a factor of four smaller than the scale of the initial mean interparticle spacing (indicated as $k_{Ny,p}$ with a dot-dashed vertical line) it is unclear whether the power spectrum results corroborate the results in Fig. 3.4, namely, that the self-similar behavior extends below the initial mean interparticle spacing. Increasing the grid size significantly beyond 1024^3 proved to be technically challenging.

3.5 Halo Mass Function and Halo Bias

As aspects of structure formation with their own set of numerical challenges (Lukić et al. 2007; Tinker et al. 2010), I also investigate the halo abundance and clustering bias in my simulation ensembles. I principally compare my results to Bagla et al. (2009) who measured the $f(\nu)$ mass function in a variety of different powerlaw models using higher resolution simulations than employed here but with far fewer realizations. Using halo abundances, Bagla et al. (2009) reports their best fit parameters for each powerlaw to the Sheth & Tormen (1999) form of $f(\nu)$, a result which can be used to predict both the halo abundance and the halo clustering using the Sheth-Tormen framework. Other models for $f(\nu)$ exist in the literature as calibrated fits to ΛCDM simulations. I principally compare to Bagla et al. (2009), who focused on pure powerlaw models.

3.5.1 Halo Mass Function

Fig. 3.8 shows my primary results for the halo mass function. To highlight the self-similar evolution in the upper panel of each sub-figure I multiply the halo mass function by a factor of $(4\pi/3)R_*^3 = M_*/\rho_m$ where $\sigma(M_*) = \delta_c$. This choice is motivated as follows: the halo mass function can be characterized solely as a function of σ,

$$\frac{dn}{d\log M} = \frac{\rho_m}{M}\frac{d\log\sigma^{-1}}{d\log M}\nu f(\nu) \tag{3.23}$$

where $\nu = \delta_c/\sigma(M)$ and $f(\nu)$ is calibrated to simulations or estimated analytically. For powerlaw models $\nu = (M/M_*)^{(n+3)/6}$ and Eq. 3.23 becomes

$$\frac{dn}{d\log M} = \frac{\rho_m}{M}\left(\frac{n+3}{6}\right)\left(\frac{M}{M_*}\right)^{(n+3)/6} f\left(\left(\frac{M}{M_*}\right)^{(n+3)/6}\right) , \tag{3.24}$$

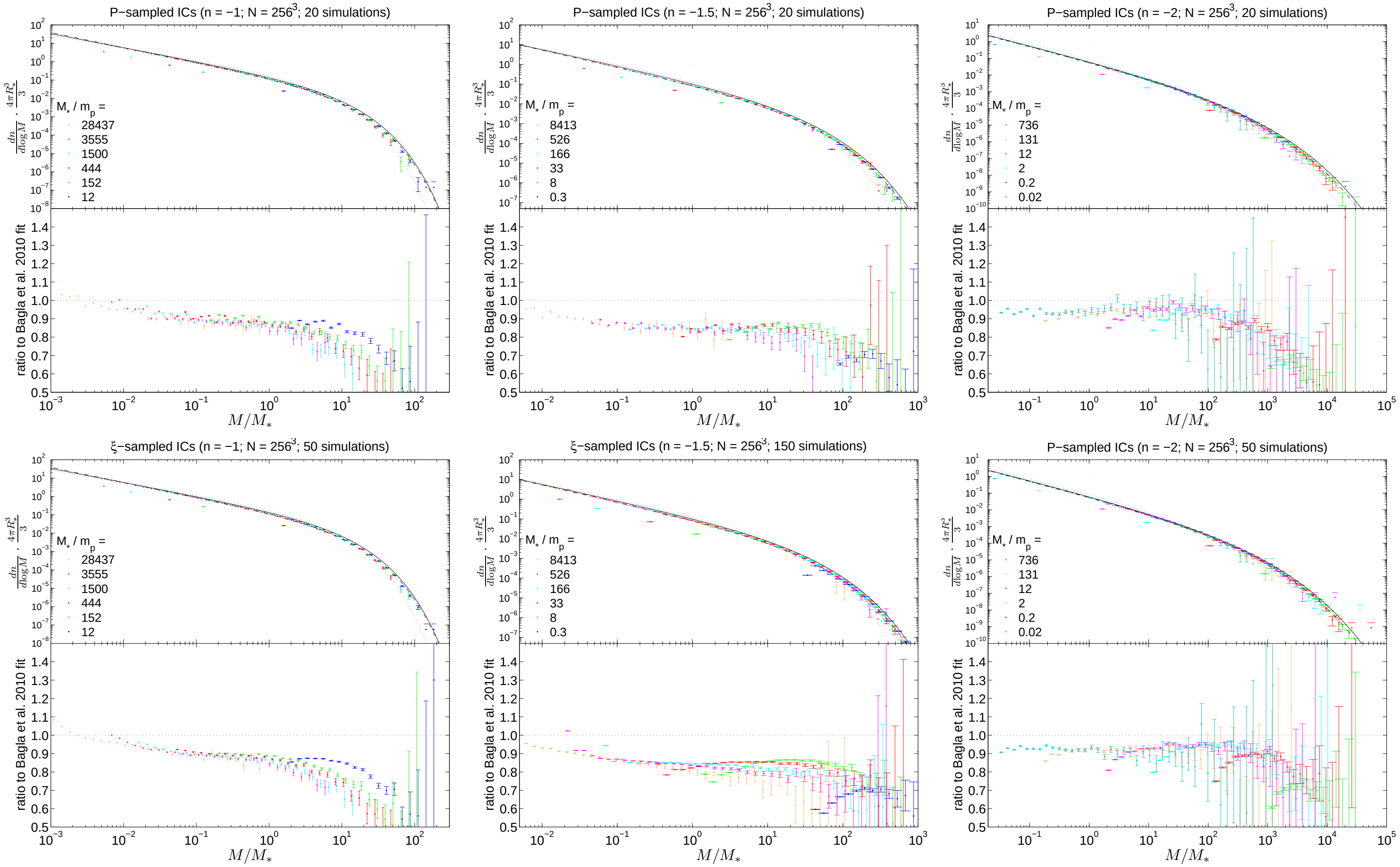

Figure 3.8: Halo mass function results for my fiducial simulation set. Results are shown either scaled by $(4\pi/3)R_*^3 = M_*/\rho_m$ (upper panels in each case) or relative to the fitting function of Bagla et al. (2009) (lower panels in each case). For each output the characteristic non-linear mass ($\sigma(M_*) \equiv \delta_c$) is shown in the legend; each output is colored consistently with other plots. Error bars show the error on the mean.

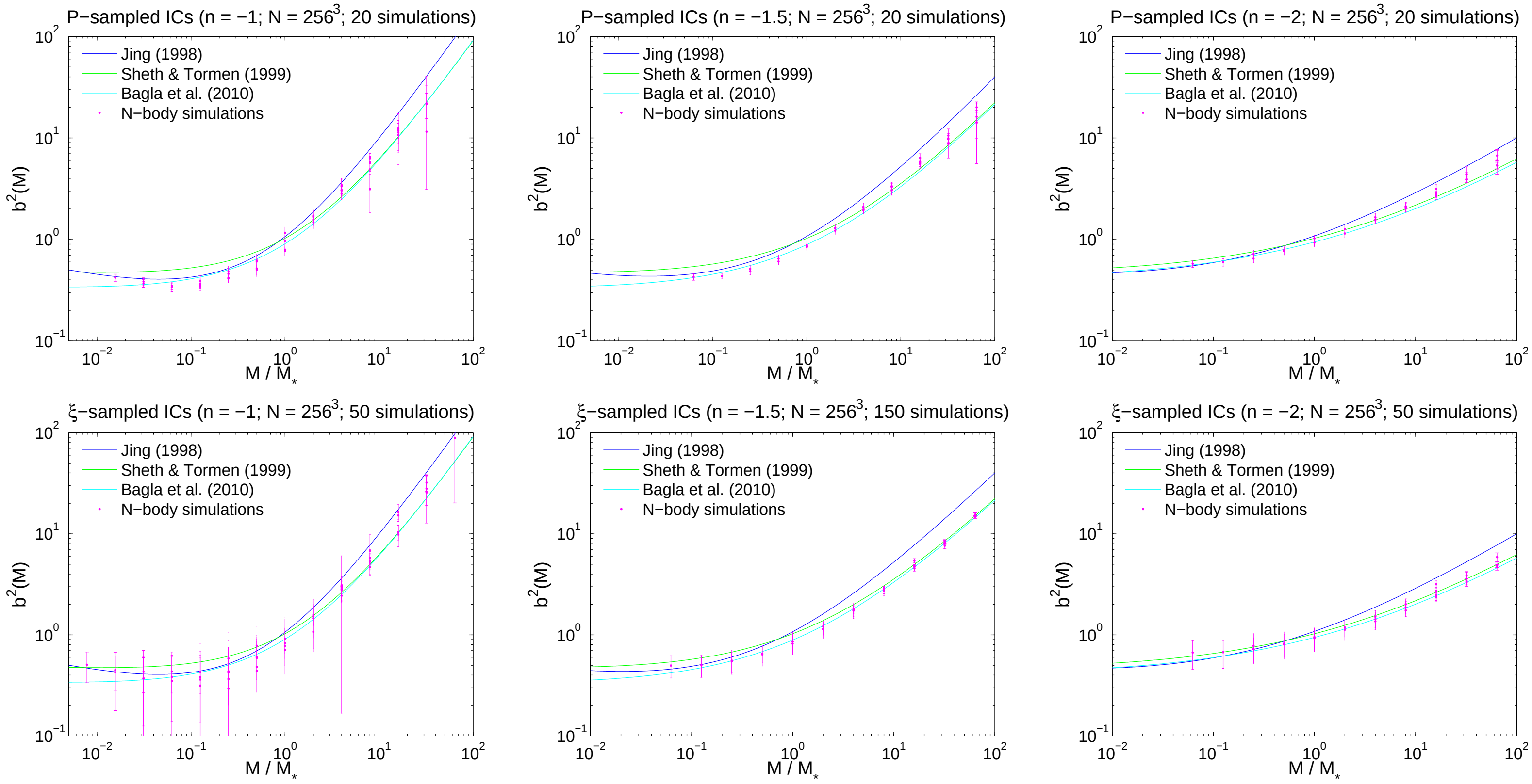

Figure 3.9: Halo clustering bias measured with $b^2(M) = \xi_{hh}(r)/\xi_{mm}(r)$. Results from my simulations are shown by magenta points; error bars show the measured error on the mean. In each panel the bias functions of Jing (1998) (blue), Sheth & Tormen (1999) (green) and Bagla et al. (2009)(cyan) are shown for comparison. Since the Sheth & Tormen (1999) bias has been calibrated to ΛCDM simulations (rather than scale-free models) this prediction is shown only for reference to the familiar ΛCDM case.

so that multiplying by $M_*/\rho_m = (4\pi/3)R_*^3$ this expression becomes a unique function of M/M_*. Alternatively, this $(4\pi/3)R_*^3$ factor can be thought of as a characteristic non-linear volume, the abundance of halos at a particular M/M_* halo mass being set by the ratio of the fixed volume to the characteristic non-linear volume. For this reason the earliest simulation outputs probe the large M/M_* regime because the fixed volume of the simulation is so much larger than $(4\pi/3)R_*^3$ that these rare objects can be more easily found than at later outputs when the non-linear volume is significantly larger.

In Fig. 3.8 both ξ-sampled and P-sampled simulation sets give remarkably similar results in each case. Dividing by the prediction from Bagla et al. (2009) as in the bottom panels in each sub-figure does not break self-similarity, and the overlap of the mass functions from each output is still a test of self-similar evolution that my simulation results typically achieve, although, interestingly, the self-similar solution deviates significantly from the Bagla et al. (2009) fit. This can be explained by noticing in the plots shown in Bagla et al. (2009) that the measurements of $f(\nu)$ from their simulations can fall below the best fit $f(\nu)$ by up to 50%. Had they used more than two free parameters in their fit to $f(\nu)$ (as they did in adopting the Sheth-Tormen framework), it seems likely that my results would agree more closely with theirs.

3.5.2 Halo Bias

In the Sheth & Tormen (1999) framework the halo bias is given by

$$b(M) = 1 + \frac{a\nu - 1}{\delta_c} + \frac{2p/\delta_c}{1 + (a\nu)^p} \tag{3.25}$$

where a and p are free parameters. Using the best fit values for a and p quoted in Bagla et al. (2009) for each powerlaw, in Fig. 3.9 I compare their results to the measured halo bias in my simulations. Although the halo bias can be equally well measured in fourier space (Jing 1999; Tinker et al. 2010) as in real space, to avoid the oscillatory features in $P(k)$ I measure the bias with $b^2(M) = \xi_{hh}(r)/\xi_{mm}(r)$ in both P-sampled and ξ-sampled simulation results, where $\xi_{hh}(r)$ is the halo-halo correlation function and $\xi_{mm}(r)$ is the matter-matter correlation function (elsewhere referred to as $\xi(r)$). One subtlety with this measurement deserves mention: in P-sampled simulations the $\xi_{hh}(r)$ measurements, like the $\xi_{mm}(r)$ measurements, suffer from the artificial imposition of the integral constraint on the scale of the box. In Appendix C, drawing upon the procedure for correcting $\xi_{mm}(r)$ described in Appendix B, I demonstrate that this correction cancels (at least to first order) in the measurement of the clustering bias. ξ-sampled simulations naturally circumvent this issue, and no integral-constraint corrections are needed to the measured $\xi_{hh}(r)$ and $\xi_{mm}(r)$.

Generally, in Fig. 3.9, the bias measurements from the two methods agree within errors and the results typically stay closer to the Bagla et al. (2009) predictions rather than the formula from Jing (1998). (The Sheth & Tormen (1999) bias, calibrated to ΛCDM simulations, is overplotted for comparison.) At large M/M_* in particular the measurements typically fall below the fitting function of Jing (1998), as previously observed for $n = -1$ in Zheng et al. (2002), who point out that the fit deviates slightly from the original simulations in Jing (1998). My results (and indirectly the $f(\nu)$ results of Bagla et al. 2009) corroborate this conclusion.

Of particular note, in Fig. 3.9, the ξ-sampled bias for $n = -1$ shows substantially larger error bars at low M/M_* than the P-sampled case. This discrepancy stems from the large variance of $\xi_{mm}(r)$ and deviation from the self-similar fit, as seen in Figs. 3.3 & 3.4, rather than the $\xi_{hh}(r)$ measurement.

Taken together the results in this section assert that the process of halo formation is consistent between the two methods, at least for the measurements I show here (see also Reid 2008).

3.6 Box-to-Box Variance

Having explored the ensemble-averaged predictions for the mean $\xi(r)$, $P(k)$, and halo mass function, in this section I turn to comparing the box-to-box variance of these quantities with expectations from theory. As emphasized by Habib et al. (2007), it is important to be able to model both the mean dark matter and/or halo statistics and the covariances of these quantities to infer the appropriate cosmological constraints from a set of large-scale structure data. In this vein, there are a number of groups that have taken up this concern for ΛCDM (Meiksin & White 1999; Scoccimarro et al. 1999; Cohn 2006; Hamilton et al. 2006; Takahashi et al. 2009). By comparing gaussian and other expectations for the box-to-box variance of these statistics, I aim to compare these predictions to a more diverse range of cosmological models with the added simplicity and clarity of powerlaw setups.

3.6.1 Var ξ results

Fig. 3.10 shows my main results for the box-to-box variance of the correlation function, in each case multiplying by a well-motivated power of $(L_{\rm box}/r_0)$ to normalize the y-axis. In each plot I compare with the expected Gaussian variance (see below) for a volume $V = L_{\rm box}^3$ as well as an estimate of what I refer to as a "floor" to the variance from non-linear effects (i.e. higher-order statistics) provided by Hyper Extended Perturbation Theory (HEPT; Scoccimarro & Frieman 1999). This term produces a fractional error proportional to the volume averaged correlation function,

$$\frac{\sigma_{\xi,\rm hept}}{\xi_{\rm pow}(r)} = \sqrt{4(1 - 2Q_3 + Q_4)\bar{\xi}(R_S)} \tag{3.26}$$

where Q_3 and Q_4 come from HEPT[14]. Note that the scalings in Fig. 3.10 are designed to cancel with the $\sqrt{\bar{\xi}(R_s)} \sim (r_0/L_{\rm box})^{(n+3)/2}$ dependence of this term so that the "HEPT floor" is a horizontal line in each plot. Although not expected to be an extremely good match to simulations, I include it in Fig. 3.10 for qualitative comparison to my results.

---

[14] The Journal version of this paper contains a typographical error in the equation for Q_4. The arXiv version is correct or, c.f., Bernardeau et al. (2002).

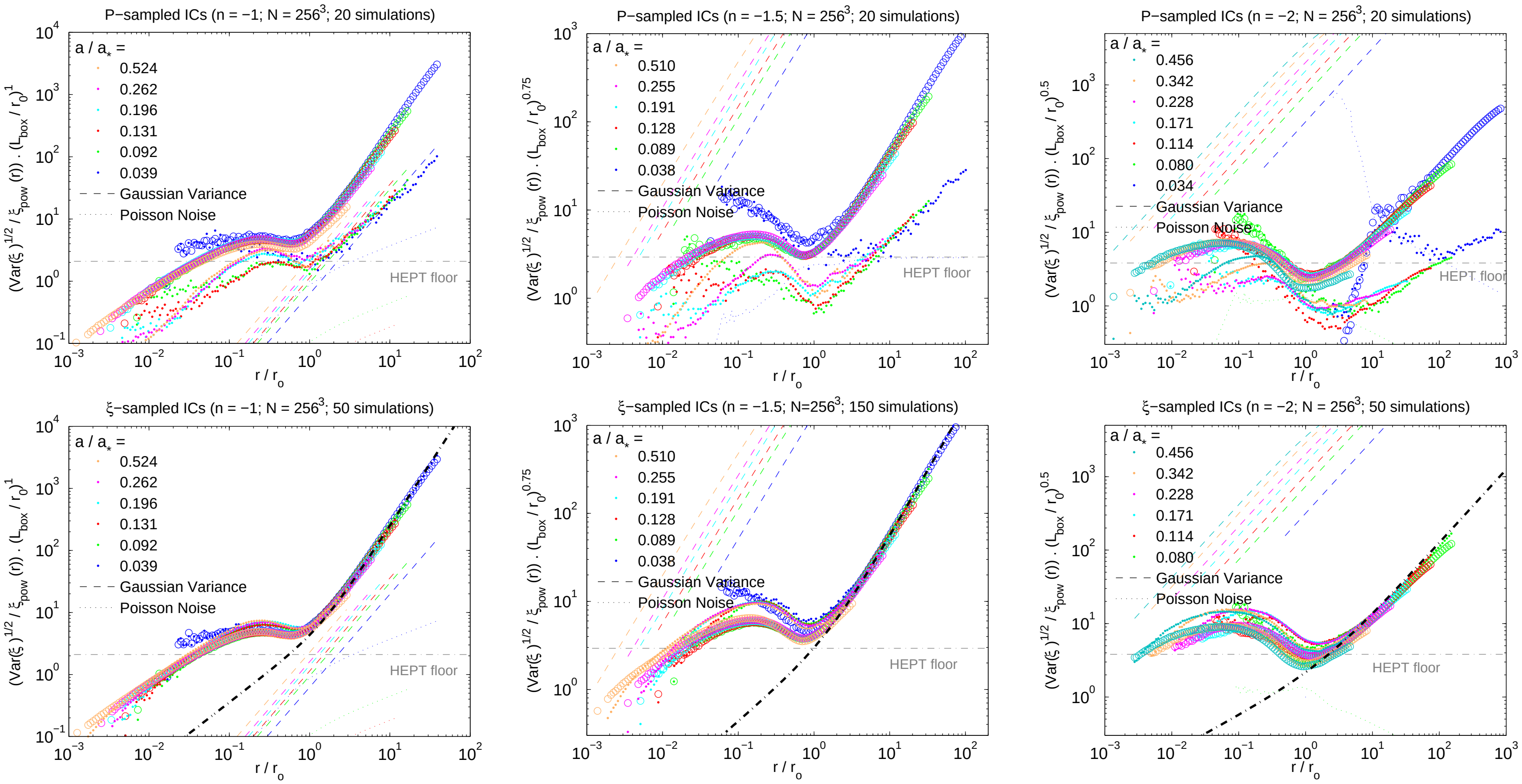

Figure 3.10: Measurements of the box-to-box variance of $\xi(r)$ (colored points) compared to expectations from Gaussian statistics (dashed colored lines). Open circles show a jackknife estimate of the variance from breaking up each simulation box into octants and measuring the correlation function in each sub-volume. The anticipated contribution to the variance from higher-order correlations (as predicted by "Hyper-Extended"PT Scoccimarro & Frieman (1999)) is shown with gray dot-dashed lines. The y-axis in each plot is scaled by $(L_{\rm box}/r_0)^{(n+3)/2}$ so that this expected "floor" to the box-to-box variance is a fixed horizontal line. Also shown is the Poisson noise level (colored dotted lines) and, for the ξ-sampled results in the lower three panels, a black dot-dashed line shows the result of Eq. 3.33.

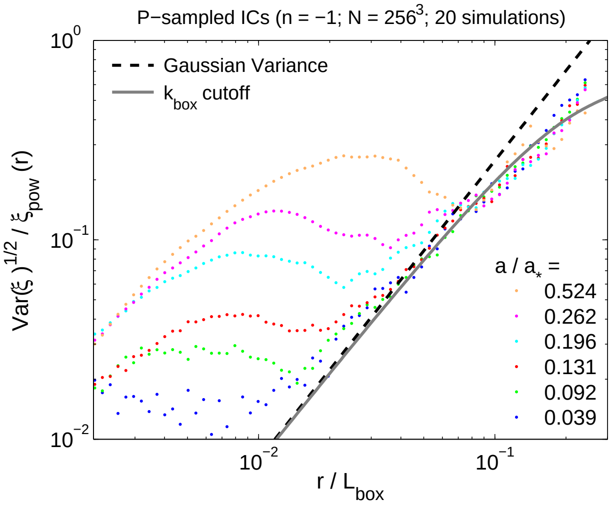

Figure 3.11: Focusing on the box-to-box variance of $\xi(r)$ for the P-sampled, $n = -1$ simulation ensemble (top left plot in Fig. 3.10). The y-axis is shown without the $(L_{\rm box}/r_0)^{(n+3)/2}$ scaling used in Fig. 3.10 and the x-axis shows the scale, r, of the correlation function measurement relative to the box scale so that the expected Gaussian variance (dashed black lines; Eq. 3.28) appears as a fixed line. Results from including a low k cutoff at $k = 2\pi/L_{\rm box}$ in the expected Gaussian variance are shown for comparison as a solid gray line.

The Gaussian variance is given by

$$\sigma_\xi^2 = \frac{1}{V\pi^2}\int_0^\infty dk k^2 \left(\frac{\sin kr}{kr}\right)^2 P(k)^2. \tag{3.27}$$

(Cohn 2006), which, for powerlaw, $P(k) = Ak^n$, models can be shown to be equivalent to

$$\frac{\sigma_\xi}{\xi_{\rm pow}(r)} = \frac{A_n}{\pi}\frac{\sqrt{\Gamma(1+2n)\sin n\pi}}{4^{(n+1)/2}}\left(\frac{r}{L_{\rm box}}\right)^{3/2} \tag{3.28}$$

where $A \equiv A_n r_0^{n+3}$, and $\Gamma(1+2n)$ is the usual gamma function. Notice that all of the r_0 dependence has canceled out with the division by $\xi_{\rm pow}(r) = (r_0/r)^{n+3}$. Unfortunately, Eq. 3.28 is only convergent for the limited range of $-1.5 < n < -0.5$. Therefore, the Gaussian variance predictions for the $n = -1.5$ and $n = -2$ results in Fig. 3.10 include cutoffs in $P(k)$ at $k = k_{\rm box}$. As a correction to a divergent result, the poor comparison of the expected Gaussian variance for these two cases is unsurprising.

In Fig. 3.10, the ξ-sampled results clearly exhibit much larger box-to-box variance than the P-sampled simulations. The ξ-sampled $n = -1$ results are perhaps most instructive since the Gaussian variance is accurate in this case – the measured variance is clearly much higher than this expectation. Though initially quite puzzling, the box-to-box variance of $\xi(r)$ turns out to be almost entirely dominated by the variance of the DC mode, so much so that it is as if the $(a_{\rm uni}/a_{\rm box})^3$

factor in Eq. 3.9 is the direct cause of the large variance over a wide regime without any interference from the variance of the $\Gamma(r)$ term. More explicitly, since $a_{\rm box,i}/a_{\rm uni} = 1 - \Delta_i/3$,

$$\left(\frac{a_{\rm uni}}{a_{\rm box,i}}\right)^3 \approx 1 + \Delta_i + \frac{2}{3}\Delta_i^2 \tag{3.29}$$

and referring to $\xi_{\rm uni,i}(r)$ as the result of scaling $\xi_{\rm box,i}(r)$ with the appropriate weighting,

$$\begin{aligned}\xi_{\rm uni,i}(r) &\approx (1 + \Delta_i + \frac{2}{3}\Delta_i^2)\frac{\Gamma(r)}{\bar{n}} - 1 \\ &= \frac{\Gamma(r)}{\bar{n}} - 1 + \frac{\Gamma(r)}{\bar{n}}\Delta_i + \frac{2}{3}\Delta_i^2\frac{\Gamma(r)}{\bar{n}} \\ &= \xi_{\rm box,i}(r) + (1 + \xi_{\rm box,i}(r))\Delta_i + (1 + \xi_{\rm box,i}(r))\frac{2}{3}\Delta_i^2\ .\end{aligned} \tag{3.30}$$

Ignoring, for the moment, the Δ_i^2 term, this is simply

$$\xi_{\rm uni,i}(r) \approx \xi_{\rm box,i}(r) + (1 + \xi_{\rm box,i}(r))\Delta_i \tag{3.31}$$

and computing the variance while assuming that $\langle\Delta_i\rangle = 0$, i.e. that the mean of the DC mode is equal to zero, it can be shown

$$\langle\xi_{\rm uni,i}^2\rangle - \langle\xi_{\rm uni,i}(r)\rangle^2 \approx (1 + 2\langle\xi_{\rm box,i}(r)\rangle)\langle\Delta_i^2\rangle \tag{3.32}$$

$$= (1 + 2\langle\xi_{\rm box,i}(r)\rangle)\frac{2^{n+2}\pi}{-n}\left(\frac{r_0}{L_{\rm box}}\right)^{n+3} \tag{3.33}$$

where in the last step I used the fact that the variance of the DC mode, $\langle\Delta_i\rangle$, is equal to $P_{\rm real}(0)/L_{\rm box}^3$. Using black dot-dashed lines, I compare this formula, with much agreement, to the ξ-sampled results in Fig. 3.10. An important detail in this derivation, which was lost in dropping the Δ_i^2 term in Eq. 3.31, is that the *mean* correlation function (i.e. $\langle\xi_{\rm uni,i}(r)\rangle$) will still retain a $(2/3)\langle\Delta_i^2\rangle$ term. This term is schematically very similar to the integral constraint correction described in Appendix B. The difference is that in ξ-sampled simulations this correction is, in a sense, applied individually to each simulation with a large scatter, rather than statistically as a correction to the ensemble-averaged correlation function. The $n = -1$ case, where the expected variance of $\xi(r)$ from Gaussian statistics is still well defined, is decisive for assessing which approach, if either, is more accurate. With this in mind, the lower left panel of Fig. 3.10 shows that the variance from the ξ-sampled method substantially exceeds the Gaussian expectations and the upper left panel of Fig. 3.10 argues that the results from the P-sampled method fall significantly below this expectation. This latter conclusion is more clearly shown in Fig. 3.11 which shows the P-sampled variance results for $n = -1$ relative to the scale of the box. As in Eq. 3.28 the Gaussian variance in Fig. 3.11 is independent of r_0. On the largest scales, the measurements from simulations systematically fall below the Gaussian expectations while on smaller scales non-linear (i.e. higher order) contributions to the variance dominate and the comparison to pure-Gaussian statistics is no longer appropriate. The suppression of the variance of $\xi(r)$ on large scales closely resembles the prediction from Eq. 3.27 using a lower limit of $k = 2\pi/L_{\rm box}$ (solid gray line).

Note that Sánchez et al. (2008) found good agreement comparing Eq. 3.28 to the covariance of the halo-halo correlation function. I point out that their comparison was made for $r/L_{\rm box} \lesssim 0.1$, where my results match the gaussian expectations without a low k cutoff.[15]

3.6.2 Var P(k) results

As discussed in the previous section the ξ-sampled method features large box-to-box variance in the correlation function. Fig. 3.12 shows the box-to-box variance of the power spectrum results in my simulation set. Unsurprisingly, the variance of the ξ-sampled results is much greater than the variance of the P-sampled results, which lie closer to the black-dashed line indicating the gaussian uncertainty from the number of modes at each k, i.e., $\mathrm{Var}^{1/2}(P(k))/P(k) = 2{N_k}^{-1/2}$. Overlayed for the P-sampled simulations in dot-dashed lines is the expected variance from non-linear effects related to the amplitude of the trispectrum (Scoccimarro et al. 1999), the fourier-space analogy of the "HEPT floor" in Fig. 3.10. This term depends on perturbation theory results which are not expected to be extremely accurate in practice. Nevertheless the $n = -1$ results agree reasonably well, while the $n = -1.5$ and $n = -2$ cases are much less convincing.

Though this source of variance should still be a contribution to the variance in ξ-sampled simulations, it is nevertheless small and I omit this term in Fig. 3.12, showing instead an estimate of the "beat coupling" expectation from Hamilton et al. (2006). I apply this term in much the same way as Reid et al. (2009), directly using the variance of the DC modes in the simulations rather than $P_L(2k_{\rm box})$ to estimate this effect which is only relevant to simulations being used to produce mock catalogues. Reid et al. (2009) find that the measured amplitude of the beat coupling term is $\sim 15\%$ below the expectation from HEPT. Compared with my results, the simulation measurements are closer to $\sim 50\%$ lower variance than this expectation. To make the most accurate mock catalogues possible, with accurate covariances, this effect should be studied more carefully. I will return to this issue in future work.

3.6.3 Var hmf results

For predicting the abundance of galaxy clusters or for more general use, high precision predictions of the halo mass function are becoming increasingly important for inferring the original, linear density field (containing the cosmological information) from observations of halo number counts. Here again, there exists an expectation of the variance from a sample volume which can be compared to the simulation results. Derived originally by Hu & Kravtsov (2003), the variance in the halo

---

[15] n.b. Sánchez et al. (2008), focusing on halo statistics, required careful bin-averaging of the $\sin kr/kr$ terms in Eq. 3.28 to achieve this agreement. In my matter correlation function results the bin widths are sufficiently small that this effect is negligible.

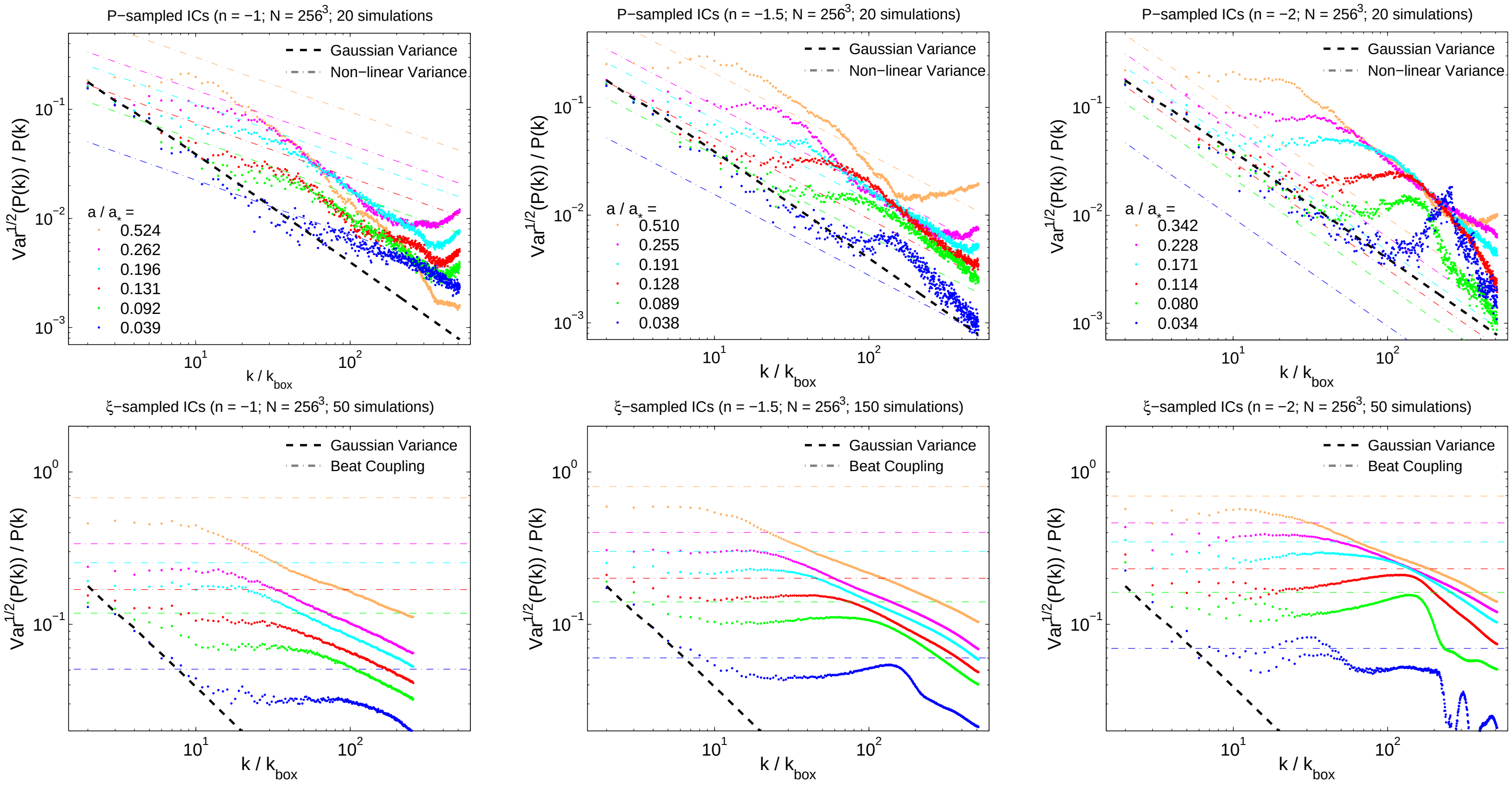

Figure 3.12: Results for the box-to-box variance of $P(k)$ in my fiducial simulation ensembles. In each plot I show in black dashed lines the expected variance from mode counting ($= 2N_k^{-1/2}$). For the P-sampled simulations I additionally show with colored dot-dashed lines the expected contribution to the variance from higher-order correlations Scoccimarro et al. (1999), while for ξ-sampled simulations (which, with fluctuating DC modes, are more analogous to surveys), I show expectations from the "beat coupling" result of Hamilton et al. (2006) and neglect to show the expected variance from non-linear effects merely for clarity.

mass function should be simply related to the Poisson noise and a sample variance term,

$$\sigma_h^2 = \frac{\langle n^2 \rangle - \bar{n}_h^2}{\bar{n}_h^2} = \frac{1}{\bar{n}_h V} + b^2 \sigma^2 (R_{\rm box}) \tag{3.34}$$

where $\sigma(R_{\rm box})$ is the rms variance in the matter overdensity in the sample volume. The first term in Eq. 3.34 is the Poisson error from number counts. Separating these two sources of error in Fig. 3.13 I plot separately the Poisson noise with dotted lines and the sample variance with a black dot-dashed line. The y-axis is normalized by $\sigma(R_{\rm box})$ so that the sample variance term is fixed in this plot (and equal to the value of $b(M/M_*)$). I assume the Bagla et al. (2009) model for the bias as in § 3.5.1.

The measured variance in P-sampled simulations seems to fall well below the sample variance estimate; the Poisson errors dominate in all regimes. This has been noticed before in a few ΛCDM studies (Crocce et al. 2010; Bhattacharya et al. 2010) The measured variance in the ξ-sampled simulations do seem to give different predictions for the variance, although, confusingly, they do drop significantly below the expectated sample variance for low M/M_*. It is not entirely clear why this is and I defer the topic to future work.

3.7 Discussion

In a suite of tests I demonstrate the accuracy of the ξ-sampled method for the ensemble-averaged statistics of $\xi(r)$, $P(k)$ and the halo mass function, finding good agreement with the expected self-similar scaling of these statistics and agreement with results P-sampled ensembles. For its capacity to predict the mean $P(k)$ and $\xi(r)$ for steep (e.g. $n = -2$) power spectra I anticipate that the ξ-sampled approach may be better suited than P-sampled simulations to model the non-linear evolution of extremely red spectra ($n \lesssim -2$). Widrow et al. (2009) demonstrate self-similarity in $n = -2.25$ simulations for the first time with impressively large, $N = 1583^3$, simulations. Recapping their argument for the numerical requirements for modeling redder spectra, one can estimate the necessary number of particles required to reach $k/k_{\rm NL} \sim 20$ (approximately the large $k/k_{\rm NL}$ limit of their $n = -2.25$ simulations). If I consider that I can measure power spectra reliably up to one half the *particle* nyquist wavenumber,

$$k_{\rm max} = \frac{k_{\rm Ny,p}}{2} = \frac{\pi N^{1/3}}{2L_{\rm box}} = \frac{N^{1/3}}{4} k_{\rm box} \tag{3.35}$$

then noting that $k_{\rm NL}/k_{\rm box} = (a/a_*)^{-2/(n+3)}$ (Widrow et al. 2009), and assuming we are interested in scales up to $k_{\rm max}/k_{\rm NL} = 20$ this implies

$$N^{1/3} = 4 \left(\frac{k_{\rm max}}{k_{\rm NL}} \right) \left(\frac{k_{\rm NL}}{k_{\rm box}} \right) = 80 \left(\frac{a}{a_*} \right)^{-2/(n+3)} \quad . \tag{3.36}$$

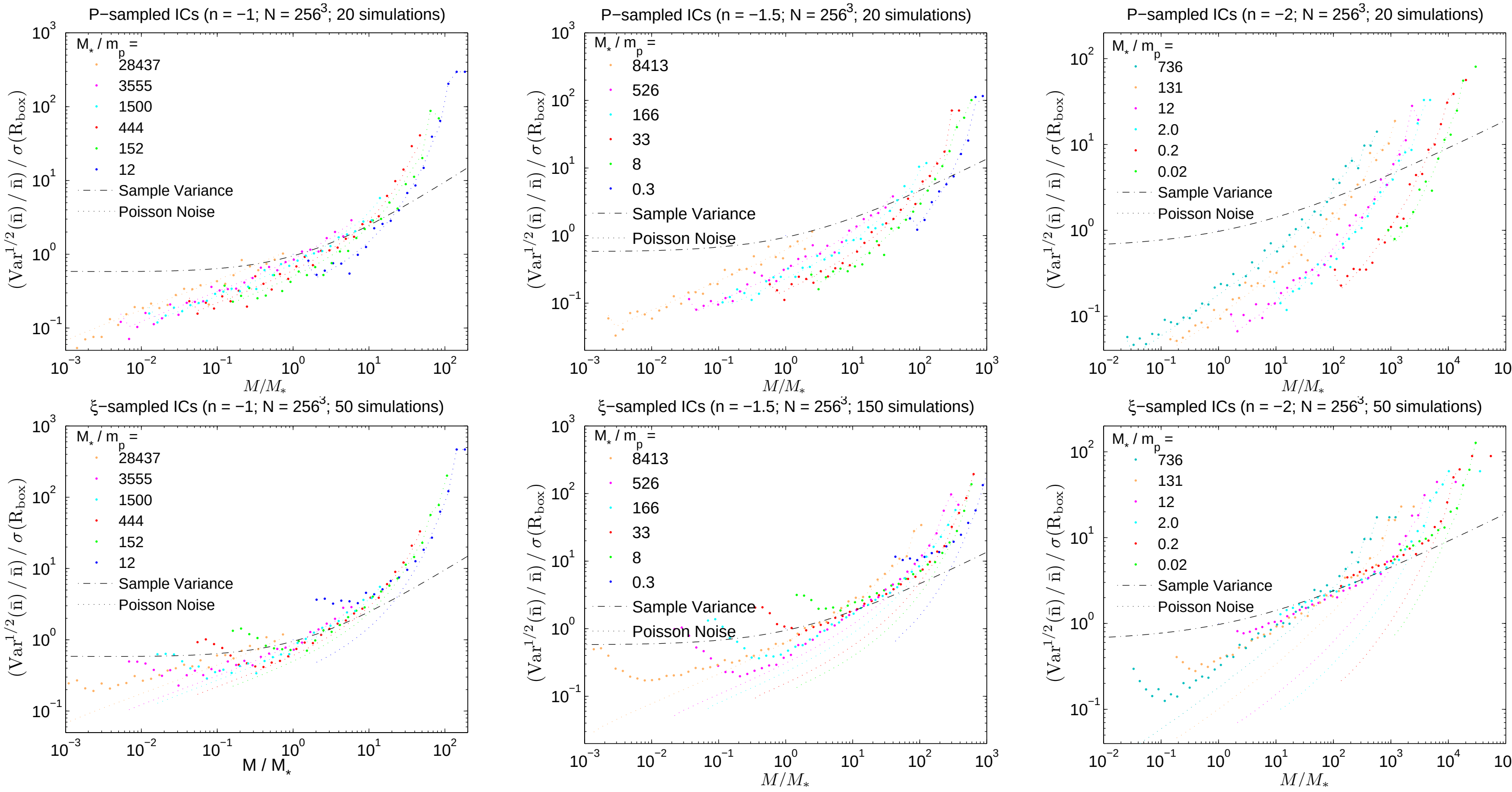

Figure 3.13: Measurements of the box-to-box variance of the halo mass function in our fiducial simulation set. As in Fig. 3.8, the legend shows outputs in terms of the characteristic non-linear mass, M_*, and the color scheme of the outputs is consistent with other figures. The y-axis is scaled by $\sigma(R_{\rm box}) = \delta_c(R_{\rm box}/R_*)^{-(n+3)/2}$ so that the sample variance expectation (in Eq. 3.34) is a fixed line in each plot. Colored dotted lines show the expected variance from Poisson noise (i.e. uncertainties from counting the number of clusters).

Widrow et al. (2009) conclude that the $n = -2.5$ case is impossible to accurately simulate with current machines. If the rules of thumb regarding the maximum a/a_* apply to $n = -2.5$, namely that the P-sampled method can be used up to $(a/a_*)_{\max} = 0.25$ and that the ξ-sampled method can be used up to $(a/a_*)_{\max} = 0.5$, then this would imply that ξ-sampled simulations substantially lower the particle requirements from $N = 80^3\,(0.25)^{-6/(n+3)} = 20480^3$ with the P-sampled method, ridiculously beyond the range of current simulations, while for ξ-sampled simulations this requirement relaxes to $N = 80^3(0.5)^{-6/(n+3)} = 1280^3$, which is well within the capabilities of current state-of-the-art supercomputers.

If, in fact, these projections hold true, then self-similar tests with the $n = -2.25$ and -2.5 cases would prove that ξ-sampled simulations are accurate in this regime and the ξ-sampled method would become a valuable tool for modeling the very small-scale dark matter clustering – on scales approaching the so-called end of the CDM hierarchy (Elahi et al. 2009; Reed et al. 2009). I am currently investigating the predictions of the ξ-sampled model for the $n = -2.25$ case as a proof-of-principle for these arguments and as a stepping stone to $n = -2.5$ simulations with the ξ-sampled method.

In regards to the excessively large box-to-box variance in the correlation function in ξ-sampled simulations, although the scatter in the DC mode correctly and naturally matches linear theory – avoiding the integral constraint problem – this feature comes at the cost of running many more simulations to reach the same precision on the mean $\xi(r)$. I experimented with different choices for $a_{\text{box}}/a_{\text{uni}}$, in an attempt to address this issue. In particular, one can instead choose to set a_{box} so that instead of ensuring that the age of the universe in each box is approximately the same, as for the choice $a_{\text{box}}/a_{\text{uni}} = 1 - \Delta/3$, one can match the amplitude of the linear theory growth function in each box. For an $\Omega_m = 1$ cosmology with no dark energy (as in the simulations presented throughout this paper) it can be shown that the choice $a_{\text{box}}/a_{\text{uni}} = 1 - (4/7)\Delta_i$ meets this requirement to first order. Tests using this 4/7 factor, rather than the original 1/3, further increased the variance in $\xi(r)$ (with the the box size fixed). Since 4/7 is larger than 1/3, a re-derivation of the result of Eq. 3.33 only increases the variance $\xi(r)$ about the mean, thus working in the opposite direction to the desired effect.

From the point of view of creating mock catalogues using the ξ-sampled approach, as in Reid et al. (2009), the varying DC mode is, in fact, an attractive feature that closely mimics the expectations for fluctuations about the mean number density in an ensemble of survey volumes. However, the gross disagreement with the Gaussian variance estimate in the ξ-sampled $n = -1$ variance measurements in Fig. 3.10 may suggest that the DC mode was allowed to fluctuate too wildly (even in the $n = -1$ case in which those fluctuations are smallest). I hope to return to this topic in future work, comparing P-sampled and ξ-sampled mock catalogues and considering which method (or some hybrid of the two) most optimally mimics surveys conducted in the real universe and in what regimes.

3.8 Summary

I conducted extensive tests demonstrating the accuracy of both conventional, P-sampled ensembles of simulations as well the so-called ξ-sampled method originally inspired by Pen (1997) and developed by Sirko (2005). Notably I point out that the $\xi(r)$ results shown in Sirko (2005) suffer from a measurement bias – an integral constraint on the scale of the box. This substantially improves the agreement with the P-sampled $\xi(r)$ results and the linear theory model in the fiducial simulations in that study.

The ξ-sampled code is very infrequently used in the literature and I show tests using pure powerlaw simulations to establish the veracity of its predictions for the mean $\xi(r)$, $P(k)$ and halo mass function results. The "scale-free" nature of these simulations give rise to the expected self-similar behavior, with the possible exception of the $n = -1$ spectral slope, which deviates from linear theory on scales approaching the box. Despite running 50 simulations, the measured mean value of the randomly sampled DC modes in these boxes was not sufficiently close to zero to correct for a correlation function as *weak* as the $n = -1$ correlation function on large scales. Comparing the correlation function results from my simulation set to high resolution results for the self-similar evolution of the correlation function revealed that my simulations do exhibit self-similar behavior on scales below the initial mean interparticle spacing – convincing evidence that cosmological N-body simulations do accurately render large scale structure in this regime and possibly refuting arguments in Joyce et al. (2009) that this is not the case.

I further explore the predictions of the code for the non-linear power spectra, finding remarkably good adherence to self-similar evolution in ξ-sampled simulations. I regard this as evidence that the ξ-sampled method is without bias when predicting mean quantities. The method also seems to maintain self-similar evolution longer for the $n = -1.5$ and $n = -2$ cases, which leads me to speculate that the ξ-sampled approach may excel at simulating extremely red ($n \lesssim -2$) power spectra, possibly becoming useful for exceedingly small box simulations which seek to model the "end" of the CDM hierarchy (Elahi et al. 2009; Reed et al. 2009).

I also set up and ran the ξ-sampled code to evolve initial conditions consistent with a powerlaw correlation function times a bump as a simplified model of BAO. At fixed $r_0/r_{\rm bao}$, these models should give unique results independent of the box size or other numerical details. I find that the ξ-sampled code performs well in these self-similar tests, matching the results of Fig. 2.3 with reasonable accuracy.

Previously, the ξ-sampled approach has been used to generate mock catalogues (Reid et al. 2009). I also measure the halo clustering in my simulations and halo mass functions, finding some discrepancies with the halo abundance measurements in Bagla et al. (2009) but generally matching the bias results that are consistent with their findings. Mindful of the code's potential use for generating mock catalogues, I then investigate the box-to-box variance in $\xi(r)$, $P(k)$ and the halo mass function. I found that in the $n = -1$ case, in which the Gaussian expectation for the variance of $\xi(r)$ is well-defined, my ξ-sampled simulations still dramatically overpredict the variance in $\xi(r)$. A more detailed study, comparing more definitively the P-sampled and ξ-sampled approaches to creating mock catalogues, will investigate these another issues in further detail, building off of the framework developed here and potentially optimizing the ξ-sampled approach for certain problems.

With the growing need for accurate predictions from simulations to interpret observations and constrain cosmological parameters, I foresee that a plurality of methods may be useful. In some cases – for example, measurements of the mean $\xi(r)$ or $P(k)$ from a finite set of simulations – the conventional P-sampled method will be optimal while for others, e.g., mock catalogues, the ξ-sampled approach or some variant may prove to be most accurate. Or, conceivably, the computationally-lean method of Angulo & White (2010) may be adequate for the task. In any case, an active consideration of simulation methods should prove to be most useful in the wider quest to characterize dark energy and other parameters of interest.

BIBLIOGRAPHY

Angulo, R. E., & White, S. D. M. 2010, MNRAS, 405, 143

Annis, J. et al. 2005, arXiv:astro-ph/0510194

Bagla, J. S., Khandai, N., & Kulkarni, G. 2009, ArXiv e-prints

Bagla, J. S., & Prasad, J. 2006, MNRAS, 370, 993

Barnes, J., & Hut, P. 1986, Nature, 324, 446

Bernardeau, F., Colombi, S., Gaztañaga, E., & Scoccimarro, R. 2002, Phys. Rep. , 367, 1

Bertschinger, E., & Gelb, J. M. 1991, Computers in Physics, 5, 164

Bhattacharya, S., Heitmann, K., White, M., Lukić, Z., Wagner, C., & Habib, S. 2010, ArXiv e-prints

Blake, C., & Glazebrook, K. 2003, ApJ, 594, 665

Blanford, R. D., the Committee for a Decadal Survey of Astronomy, & Astrophysics. 2010, *New Worlds, New Horizons in Astronomy and Astrophysics* (Washington, D.C: The National Academies Press)

Bouchet, F. R., Colombi, S., Hivon, E., & Juszkiewicz, R. 1995, A&A, 296, 575

Carlson, J., White, M., & Padmanabhan, N. 2009, PRD, 80, 043531

Cohn, J. D. 2006, Nature, 11, 226

Cole, S. 1997, MNRAS, 286, 38

Cole, S. et al. 2005, MNRAS, 362, 505

Colombi, S., Bouchet, F. R., & Hernquist, L. 1996, ApJ, 465, 14

Colombi, S., Jaffe, A., Novikov, D., & Pichon, C. 2009, MNRAS, 393, 511

Cooray, A., & Sheth, R. 2002, Phys. Rep. , 372, 1

Crocce, M., Cabre, A., & Gaztañaga, E. 2010, arXiv:1004.4640

Crocce, M., Pueblas, S., & Scoccimarro, R. 2006, MNRAS, 373, 369

Crocce, M., & Scoccimarro, R. 2006, PRD, 73, 063519

——. 2008, PRD, 77, 023533

Davis, M., Efstathiou, G., Frenk, C. S., & White, S. D. M. 1985, ApJ, 292, 371

Davis, M., & Peebles, P. J. E. 1977, ApJS, 34, 425

Drinkwater, M. J. et al. 2010, MNRAS, 401, 1429

Efstathiou, G., Frenk, C. S., White, S. D. M., & Davis, M. 1988, MNRAS, 235, 715

Einasto, J., Klypin, A. A., Saar, E., & Shandarin, S. F. 1984, MNRAS, 206, 529

Eisenstein, D., & White, M. 2004, PRD, 70, 103523

Eisenstein, D. J., & Hu, W. 1998, ApJ, 496, 605

Eisenstein, D. J., Hu, W., & Tegmark, M. 1998, ApJL, 504, L57+

Eisenstein, D. J., Seo, H., & White, M. 2007, ApJ, 664, 660

Eisenstein, D. J. et al. 2005, ApJ, 633, 560

Elahi, P. J., Thacker, R. J., Widrow, L. M., & Scannapieco, E. 2009, MNRAS, 395, 1950

Frenk, C. S., White, S. D. M., Davis, M., & Efstathiou, G. 1988, ApJ, 327, 507

Gabrielli, M., Sylos Labini, F., Joyce, M., & Pietronero, L. 2005, *Statistical Physics for Cosmic Structures* (Berlin: Springer Press)

Gurbatov, S. N., Saichev, A. I., & Shandarin, S. F. 1989, MNRAS, 236, 385

Habib, S., Heitmann, K., Higdon, D., Nakhleh, C., & Williams, B. 2007, PRD, 76, 083503

Hamilton, A. J. S., Rimes, C. D., & Scoccimarro, R. 2006, MNRAS, 371, 1188

Heitmann, K., White, M., Wagner, C., Habib, S., & Higdon, D. 2010, ApJ, 715, 104

Hill, G. J. et al. 2008, in Astronomical Society of the Pacific Conference Series, ed. T. Kodama, T. Yamada, & K. Aoki, Vol. 399, 115

Hockney, R. W., & Eastwood, J. W. 1981, Computer Simulation Using Particles (New York: McGraw-Hill)

Hu, W., & Kravtsov, A. V. 2003, ApJ, 584, 702

Jain, B., Mo, H. J., & White, S. D. M. 1995, MNRAS, 276, L25

Jing, Y. P. 1998, ApJL, 503, L9+

——. 1999, ApJL, 515, L45

——. 2005, ApJ, 620, 559

Joyce, M., Marcos, B., & Baertschiger, T. 2009, MNRAS, 394, 751

Kaiser, N. et al. 2002, in Society of Photo-Optical Instrumentation Engineers (SPIE) Conference Series, ed. J. A. Tyson & S. Wolff, Vol. 4836, 154–164

Kazin, E. A. et al. 2010, ApJ, 710, 1444

Komatsu, E. et al. 2010, arXiv:1001.4538

Lacey, C., & Cole, S. 1994, MNRAS, 271, 676

Landy, S. D., & Szalay, A. S. 1993, ApJ, 412, 64

Laureijs, R., et al. 2009, arXiv:0912.0914

Lewis, A., Challinor, A., & Lasenby, A. 2000, ApJ, 538, 473

Little, B., Weinberg, D. H., & Park, C. 1991, MNRAS, 253, 295

LSST Science Collaboration. 2009, arXiv:0912.0201

Lukić, Z., Heitmann, K., Habib, S., Bashinsky, S., & Ricker, P. M. 2007, ApJ, 671, 1160

Makino, N., Sasaki, M., & Suto, Y. 1992, PRD, 46, 585

Matsubara, T. 2008, PRD, 77, 063530

McDonald, P. 2007, PRD, 75, 043514

Meiksin, A., & White, M. 1999, MNRAS, 308, 1179

Montesano, F., Sánchez, A. G., & Phleps, S. 2010, MNRAS, 1223

Nusser, A., & Colberg, J. M. 1998, MNRAS, 294, 457

Padmanabhan, N., & White, M. 2009, PRD, 80, 063508

Peacock, J. A., & Dodds, S. J. 1996, MNRAS, 280, L19

Peebles, P. J. E. 1980, *The Large-Scale Structure of the Universe* (Princeton: Princeton University Press)

Peebles, P. J. E., & Yu, J. T. 1970, ApJ, 162, 815

Pen, U. 1997, ApJL, 490, L127+

Percival, W. J. et al. 2010, MNRAS, 401, 2148

Reed, D. S., Bower, R., Frenk, C. S., Jenkins, A., & Theuns, T. 2009, MNRAS, 394, 624

Reid, B. A. 2008, PhD thesis, Princeton University

Reid, B. A., Spergel, D. N., & Bode, P. 2009, ApJ, 702, 249

Sánchez, A. G., Baugh, C. M., & Angulo, R. 2008, MNRAS, 390, 1470

Schlegel, D., White, M., & Eisenstein, D. 2009a, arXiv:0902.4680

Schlegel, D. J. et al. 2009b, arXiv:0904.0468

Scoccimarro, R. 1997, ApJ, 487, 1

——. 1998, MNRAS, 299, 1097

Scoccimarro, R., & Frieman, J. A. 1996, ApJ, 473, 620

——. 1999, ApJ, 520, 35

Scoccimarro, R., Zaldarriaga, M., & Hui, L. 1999, ApJ, 527, 1

Seo, H. et al. 2010, ApJ, 720, 1650

Seo, H., & Eisenstein, D. J. 2003, ApJ, 598, 720

——. 2007, ApJ, 665, 14

Seo, H., Siegel, E. R., Eisenstein, D. J., & White, M. 2008, ApJ, 686, 13

Sheth, R. K., & Tormen, G. 1999, MNRAS, 308, 119

Sirko, E. 2005, ApJ, 634, 728

Smith, R. E. et al. 2003, MNRAS, 341, 1311

Smith, R. E., Scoccimarro, R., & Sheth, R. K. 2008, PRD, 77, 043525

Springel, V. 2005, MNRAS, 364, 1105

Takahashi, R. et al. 2009, ApJ, 700, 479

Tegmark, M. et al. 2006, PRD, 74, 123507

The Dark Energy Survey Collaboration. 2005, arXiv:astro-ph/0510346

Tinker, J. L., Robertson, B. E., Kravtsov, A. V., Klypin, A., Warren, M. S., Yepes, G., & Gottlöber, S. 2010, ApJ, 724, 878

Tormen, G., & Bertschinger, E. 1996, ApJ, 472, 14

Vishniac, E. T. 1983, MNRAS, 203, 345

Weinberg, D. H., & Gunn, J. E. 1990, MNRAS, 247, 260

Widrow, L. M., Elahi, P. J., Thacker, R. J., Richardson, M., & Scannapieco, E. 2009, MNRAS, 397, 1275

Wu, H., Zentner, A. R., & Wechsler, R. H. 2010, ApJ, 713, 856

Zeldovich, Y. B. 1970, A&A, 5, 84

Zheng, Z., Tinker, J. L., Weinberg, D. H., & Berlind, A. A. 2002, ApJ, 575, 617

Appendix A
PURE POWERLAW SIMULATIONS

Having performed pure powerlaw simulations for the sake of better understanding the non-linear power spectra of the fiducial simulations, I give fitting functions for the $n = -0.5, -1$ and -1.5 powerlaws using 512^3-particle Gadget2 simulations, which were set up similarly to the fiducial simulations as outlined in § 2.2. The interested reader can consult the excellent paper by Widrow et al. (2009) to find fitting functions for other powerlaws.

Fig. A.1 shows the primary powerlaw results compared against other fitting functions in the literature, either specific to each powerlaw or universal fitting functions designed to match a variety of powerlaws and cosmologies. These simulations do not extend to impressively large values of $k/k_{\rm NL}$ compared to Widrow et al. (2009), in part because of how long I chose to evolve the simulations and in part because I chose, conservatively, to only show k-values up to *one fourth* the particle nyquist wavenumber, i.e., half the rule of thumb recommended by Heitmann et al. (2010). However, I run a number of realizations of each powerlaw (six realizations for $n = -0.5$, four for $n = -1$, and ten for $n = -1.5$), which is a few to many more than in previous studies. As a result the error bars in Fig. A.1, which show the measured errors on the mean from all realizations in each case, can be quite constraining.

Since there is always a concern that the numerical results will be invalidated when the clustering power on the scale of the box becomes large, following the convention of Widrow et al. (2009) I show the value of $a/a_* = (k_{\rm B}/k_{\rm NL})^{(n+3)/2}$ for each output in all three panels as an indicator for how close the non-linear scale has come to the scale of the box. As stated previously, even the simulations with the most large scale clustering ($n = -1.5$) fall comfortably below the threshold where the loss of clustering power from beyond the box scale might be a concern. More quantitatively, in Fig. A.1, a/a_* is typically $\ll 1$, and in the $n = -1.5$ case the last output only reaches $a/a_* = 0.18$. Importantly, the later outputs seem to show the self-similar scaling required by the scale-free nature of the initial conditions, the results falling along the same curve when plotted against $k/k_{\rm NL}$ and divided by $\Delta^2_L(k)$. For the earlier outputs this scaling seems not to have set in yet in some cases, a fact revealed by the self-similar test. Therefore I define the non-linear fitting functions as much as possible to the later outputs which are least affected by the clustering signature of the initial grid.

I present non-linear fitting functions as a generalization of the functional form in Widrow et al. (2009):

$$\Delta^2_{\rm NL}(k) = \Delta^2_{\rm L}(k) f_n(k/k_{\rm NL}), \tag{A.1}$$

$$f_n(x) = \left(\frac{1 + Ax + Bx^\alpha + Ex^\epsilon}{1 + Cx^\gamma + Dx^\delta}\right)^\beta. \tag{A.2}$$

Table A.1: Best-fit Parameters for the Non-linear Fitting Function

n	A	B	C	D	E	α	β	γ	δ	ϵ
-0.5	-0.1309	0.1131	0.1296	-0.02472	0.0	8.599	2.066	8.714	0.4565	0.0
-1	-0.4722	0.3542	0.04449	-0.2020	-0.08956	1.358	1.447	1.911	0.3963	0.2564
-1.5	-0.0792	0.1704	0.008748	0.0	0.0	1.225	2.672	2.1306	0.0	0.0

The $n = -1$ results primarily drive the necessity of making this generalization. The $n = -1.5$ results seem reasonably well represented with the Widrow formula, so I set $E = D = \epsilon = \delta = 0$ in that case, while in the $n = -0.5$ case I set $E = \epsilon = 0$, which still allows sufficient degrees of freedom to adequately describe the simulation results. The fitting formula above should be accurate to $k/k_{\rm NL} \sim 5$ for $n = -0.5$, $k/k_{\rm NL} \sim 100$ for $n = -1$ (larger because the fit was forced to closely match the results of Widrow et al. (2009) at high k), and $k/k_{\rm NL} \sim 6.5$ for $n = -1.5$.

A.0.1 Specific Comments on n = -0.5, -1, & -1.5

To my knowledge the most recent work to explicitly show the non-linear evolution of a pure $n = -0.5$ spectrum from simulations is Jain et al. (1995), whose universal fitting function I plot alongside my results in Fig. A.1. The universal fitting functions of Peacock & Dodds (1996) and Smith et al. (2003) are capable of making predictions for $n = -0.5$, but their fitting functions were trained only on $n = 0$ and $n = -1$ simulations to set the scaling in this regime. With this caveat the remarkable agreement of the prediction of Peacock & Dodds (1996) and my $n = -0.5$ results seems somewhat fortuitous and the disagreement with the Smith et al. (2003) prediction seems not so surprising.

The discrepancy between my $n = -1$ simulation results and the Widrow fitting function is entirely explainable by the sparseness of their measurements in the quasi-linear regime and is not indicative of any kind of problem with either their or our simulations. At larger $k/k_{\rm NL}$ both results overlap nicely, and I define a fitting function to closely match theirs for $k/k_{\rm NL} \gtrsim 3$. Also plotted alongside the $n = -1$ simulation results is a fitting function specific to $n = -1$ from Appendix B of Smith et al. (2003). There is a typo in their fitting formula (their Eq. B1), which should read

$$f_{EdS}(y) = y \left[\frac{1 + y/a + (y/b)^2 + (y/c)^{\alpha-1}}{(1 + (y/d)^{(\alpha-\beta)\gamma})^{1/\gamma}} \right] \tag{A.3}$$

(R. Smith private communication). The corrected formula for $n = -1$ is shown in the middle panel of Fig. A.1, and although at $k \sim k_{\mathrm{NL}}$ it deviates strongly from either fitting function, at lower k it matches my results reasonably well.

Appendix B of Smith et al. (2003) also includes a set of constants tuned specifically for their $n = -1.5$ results, but there is a typo in their table in the reported value of α. From quantitative comparison to their Fig. 11 (especially at large k/k_{NL}), the correct value seems to be $\alpha \approx 7$, rather than $\alpha = 0.707$ as reported. I show this result alongside my other results for $n = -1.5$ in the right panel of Fig. A.1. Since both Peacock & Dodds (1996) and Jain et al. (1995) include $n = -1.5$ simulations in their universal fits, I also show the predictions of their fitting functions. Finally, I plot the expectations from SPT for $n = -1.5$ in the limit that the UV cutoff goes to infinity, as in Appendix B of Scoccimarro & Frieman (1996). In my fiducial simulations this is the formula used to predict the evolution of the powerlaw in the SPT model shown in Fig. 2.11. The SPT+ models in Fig. 2.11 instead use the non-linear fitting functions just described to model the evolution of the $n = -0.5$ and $n = -1$ powerlaws.

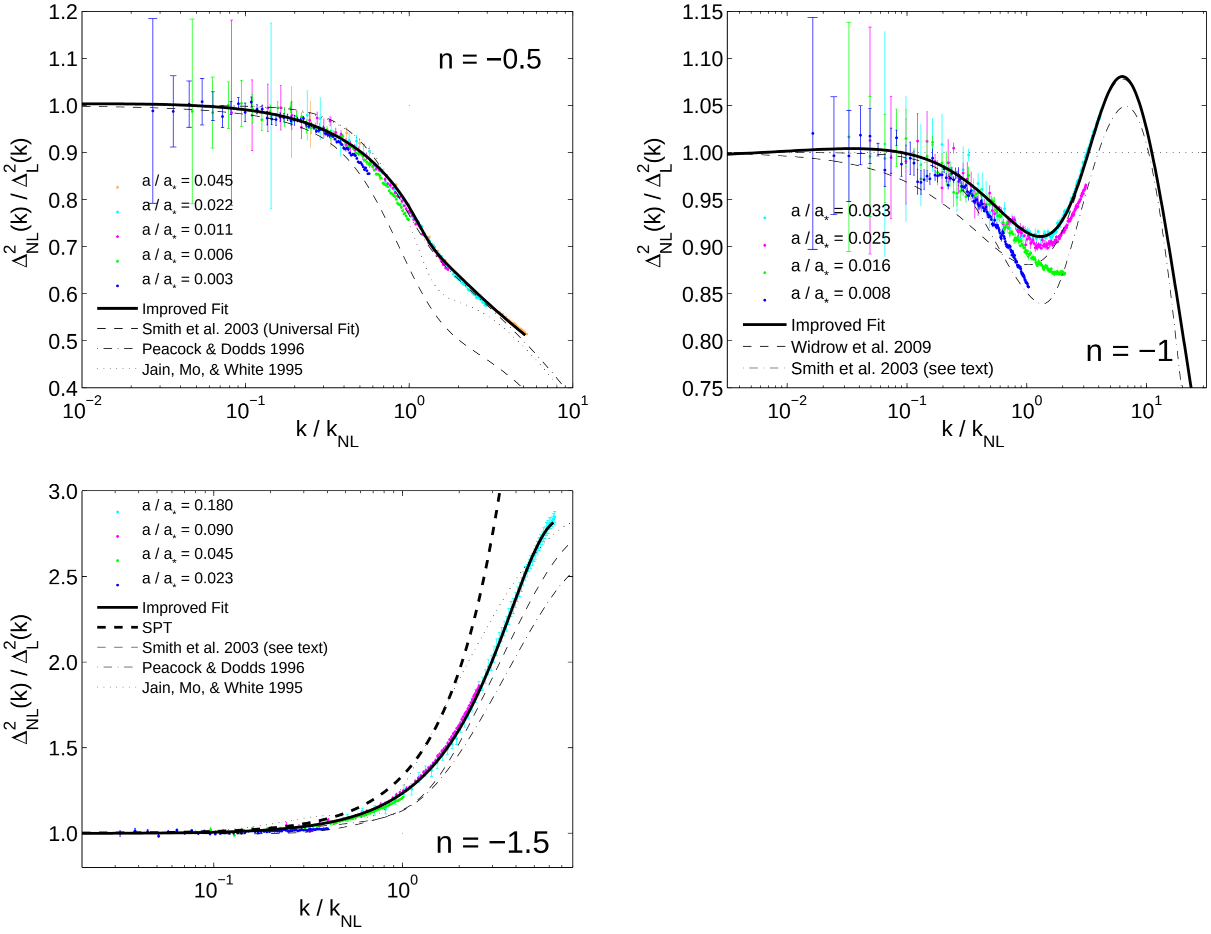

Figure A.1: Results from pure powerlaw simulations (colored points with error bars) compared to various fitting functions in the literature (black dotted, dash-dotted or dashed lines). Also shown is my improved fit in thick black lines (Eqs. A.1 & A.2) and, for $n = -1.5$, the analytically derived SPT prediction from Appendix B of Scoccimarro & Frieman (1996) is shown with a thick black dashed line.

Appendix B

INTEGRAL CONSTRAINT CORRECTIONS TO THE MATTER AUTOCORRELATION FUNCTION

When estimating the correlation function in simulations, I divide the average number of neighbors found around paticles in the separation range $r \rightarrow r+dr$ by the number expected for an unclustered distribution of number density N/V:

$$\hat{\xi}(r) = \frac{\langle N_{\rm nbr}(r \rightarrow r + dr)\rangle}{4\pi r^2\,dr \times N/V} - 1 \ , \tag{B.1}$$

where N is the simulation box volume, N is the total number of particles and I use $\hat{\xi}(r)$ to distinguish this estimated correlation function from the true correlation function $\xi_{\rm true}(r)$ of the underlying cosmological model. This procedure is subject to a well known "integral constraint" bias (described by, e.g., (Peebles 1980, §47)), which arises because the simulation volume itself is forced to have the cosmological mean density. The fact that the total number of particle pairs in the box is $N(N-1)/2 \approx (1/2)N^2$ imposes the requirement

$$\int_{V_{\rm box}} d^3r\,\hat{\xi}(r) \approx \int_0^{R_S = L_{\rm box}/1.61} 4\pi r^2\,dr\,\hat{\xi}(r) = 0 \ , \tag{B.2}$$

where I have approximated the integral over the box volume as the integral over a sphere of volume $(4\pi/3)R_S^3 = V = L_{\rm box}^3$. For large volume ΛCDM simulations, the bias in $\hat{\xi}(r)$ is usually a small effect because the true correlation function goes rapidly to zero, then becomes negative at large r, making equation (B.2) easy to satisfy. However, for powerlaw models with negative n, the slow decay of the correlation function makes the integral constraint bias more important.

I account for the integral constraint by assuming that it produces a scale-independent additive bias, so that the mean value of $\hat{\xi}(r)$ averaged over an ensemble of simulations would be

$$\hat{\xi}(r) = \xi_{\rm true}(r) + \xi_{\rm bias} \ . \tag{B.3}$$

For powerlaw models, Eq. (B.2) then implies

$$\int_0^{R_S} 4\pi r^2\, dr\ [\xi_{\rm true}(r) + \xi_{\rm bias}] = 0 \tag{B.4}$$

and thus

$$\xi_{\rm bias} = -\frac{3}{4\pi R_S^3}\int_0^{R_S} 4\pi r^2\, dr\, \xi_{\rm true}(r) = \frac{3}{n}\left(\frac{r_0}{R_S}\right)^{n+3}\ , \tag{B.5}$$

where I have used the linear theory $\xi_L(r) = (r/r_0)^{-(n+3)}$ for $\xi_{\rm true}(r)$. More elegantly, this bias is simply the volume-averaged correlation function, $\xi_{\rm bias} = -\bar{\xi}_L(R_s)$, which agrees with the conclusions of (Bernardeau et al. 2002, §6.4.2), who derived this term using the sophisticated error analysis in Landy & Szalay (1993).

In all figures I plot the corrected correlation function

$$\xi(r) = \hat{\xi}(r) + \bar{\xi}_L(R_S)\ . \tag{B.6}$$

At large r, the *fractional* correction is

$$\frac{\xi(r) - \hat{\xi}(r)}{\xi_L(r)} = \frac{3}{-n}\left(\frac{1.61r}{L_{\rm box}}\right)^{n+3}\ . \tag{B.7}$$

Since r is always less than $L_{\rm box}/1.61$, this correction is fractionally larger for more negative n and, at fixed n, the effect is most important for r approaching the box scale as previously mentioned. In practice, I find that the integral constraint makes little quantitative difference to the appearance of, e.g., Figs. 2.3 & 2.8 for $n = -0.5$, a noticeable difference for $n = -1$, and an important difference for $n = -1.5$. In particular, the box size convergence tests in Figure 2.8 succeed for $n = -1.5$ only because I include the integral constraint correction.

Appendix C

THE INTEGRAL CONSTRAINT IN HALO BIAS MEASUREMENTS

As discussed in Appendix B, correlation function measurements in P-sampled simulations suffer from an integral constraint imposed on the scale of the box. These conclusions extend to clustering measurements for any distribution of points in a finite volume (e.g. dark matter, halos, quasars), and, as a remedy consistent with the conclusions of Bernardeau et al. (2002) & Landy & Szalay (1993), I proposed the correction:

$$\xi(r) = \hat{\xi}(r) + \bar{\xi}(R_S) \tag{C.1}$$

where $\bar{\xi}(r)$ is the measured correlation function, $\xi(r)$ is the "true" corrected correlation function and $\bar{\xi}(R_S)$ is given by

$$\bar{\xi}(R_S) = \frac{3}{4\pi R_S^3} \int_0^{R_S} 4\pi r^2 dr \xi_L(r) \tag{C.2}$$

assuming a linear theory model for $\xi(r)$ in the integral. R_S is set by $R_S = (4\pi/3)^{-1/3} L_{\rm box} \approx L_{\rm box}/1.61$. This correction is used in the P-sampled results in Figs. 3.3 & 3.4. Importantly, without this correction, the $\xi(r)$ results would not match linear theory, as expected, in the large r/r_0 regime.

For bias measurements I am interested in the quantity,

$$b^2 = \frac{\xi_{hh}(r)}{\xi_{mm}(r)} \ , \tag{C.3}$$

where $\xi_{hh}(r)$ is the halo-halo correlation function and $\xi_{mm}(r)$ is the matter-matter correlation function, elsewhere referred to in this paper as $\xi(r)$. Using the corrected values of $\xi_{hh}(r)$ and $\xi_{mm}(r)$ yields,

$$b^2 = \frac{\hat{\xi}_{hh}(r) + b^2\bar{\xi}(R_S)}{\hat{\xi}_{mm}(r) + \bar{\xi}(R_S)} \tag{C.4}$$

where $\hat{\xi}_{hh}(r)$ are $\hat{\xi}_{mm}(r)$ are uncorrected correlation function measurements. Moving the denominator of Eq. C.4 to the left hand side,

$$b^2(\hat{\xi}_{mm}(r) + \bar{\xi}(R_S)) = \hat{\xi}_{hh}(r) + b^2\bar{\xi}(R_S) \tag{C.5}$$

the $\bar{\xi}(R_S)$ terms cancel, leaving just

$$b^2 = \frac{\hat{\xi}_{hh}(r)}{\hat{\xi}_{mm}(r)}\ . \tag{C.6}$$

It is unclear whether this subtlety was noticed in previous studies where bias measurements from pure powerlaw simulations using real-space statistics have been made Jing (1998); Zheng et al. (2002). In any case, this appendix argues that the correction cancels, at least to first order. More sophisticated models for correcting for the integral constraint (e.g. Bagla & Prasad (2006)) may require more lengthy derivations to obtain unbiased estimators of the halo clustering bias.